Study on Energetics and Particle Acceleration in Superbubbles and Development of X-ray CCD Cameras onboard the *Suzaku* Satellite

Hiroshi Nakajima
Department of Physics, Faculty of Science
Graduate School of Kyoto University

January 5, 2007

Abstract

This thesis has two distinct components. One concerns the ground- and in-orbit calibration of the X-ray Imaging Spectrometer (XIS), the Charge Coupled Device (CCD) onboard the *Suzaku* X-ray astronomical satellite. The other involves the X-ray observations and analyses of the superbubbles (SBs), which have been considered to be formed by the composite contributions from the strong stellar winds from massive stars in the shell and successive supernova (SN) explosions, utilizing *Suzaku* and other satellites.

Successive SN explosions in SBs may re-heat the cavity and its wall leaving sometimes stellar remnants such as neutron stars and black holes inside. Both of the remnants may emit either diffuse or point like X-rays. Young massive stars in an OB association are also known to be moderately bright X-ray sources. Therefore, X-ray observations can reveal valuable information on the overall structure and evolution of SBs. The SBs would also be the key cites of particle acceleration. However, no observational evidence for particle acceleration and/or limited information of high temperature plasma from SBs have only been obtained. We found strong non-thermal X-ray emission from 30 Dor C, an SB in the Large Magellanic Cloud (LMC). Assuming that this emission is due to the synchrotron X-rays and that the thermal pressure inside the SB is equal to that of the magnetic field, we showed that the electrons are accelerated up to $\sim$90 TeV in the shell of 30 Dor C. This is the first clear evidence of the long-term particle acceleration inside an SB. On the other hand, N44, another SB in the LMC does not show non-thermal X-ray emission. If we sum up the thermal energies of hot gases including the breakout regions around the main shell of N44 and kinetic energy, it reaches up to the expected injected energy by the stellar winds and SNe. The lack of the non-thermal X-ray emission is seen in other galactic SB candidates Sgr C and CTB 37A, which makes 30 Dor C the conspicuous object.

The instrumental portion of this thesis especially concerns the verification and performance investigation of the Charge Injection (CI) capability of the XIS. The existing X-ray CCDs working in orbit suffer from the radiation damage due to the charged particles and subsequent degradation of the charge transfer inefficiency (CTI). Then we have tried to run the CI for the first time among the X-ray CCDs in orbit. In principle, charge packets are artificially injected into each transfer channel and are subsequently read after the transfer in the same manner as X-ray events. This method allows us to measure and/or mitigate the amount of charge loss on a column-to-column basis, which in turn, can potentially be a powerful tool for the calibration of the CTI. The column-to-column CTI correction for the calibration source spectra significantly reduces the line widths compared to those with a column-averaged CTI correction (from 193 eV to 173 eV in FWHM on an average). In addition, this method significantly reduces the low energy tail in the line profile of the calibration source spectrum.

Contents

List of Figures

List of Tables

Chapter 1

Introduction

Since the daybreak of the astronomy, its progress has been facilitated by observations with novel instruments at each time. Especially with respect to the observations of the photons from celestial objects, many astronomers have taken their efforts to obtain the precise and accurate values of the wavelength (*i.e.* energy), flux intensity, direction, and polarity with wide range. The sophisticated spectra, light curves, and images enable one to reveal the consciousness and/or the emission mechanisms of the objects.

Extending the effective energy range to the X-ray band, we have been able to see and investigate energetic phenomena hidden behind dense absorption columns such as shocked thermal plasma in supernova remnants (SNRs), accretion disks around black holes, hot intracluster gases in clusters of galaxies, and so on. In fact, in the case of the Galactic Center (GC), the absorption column density is 6×10^{22} cm^{-2}, which is consistent with the suggested distance of 8.0 kpc to the GC (McNamara et al. 2000) and the average number density of the hydrogen atoms along the galactic plane of 1 cm^{-3}.

The first imaging in the hard X-ray band (2 - 10 keV) was performed by *ASCA* satellite. Since then, Charge Coupled Device (CCD) has been the primary instrument because of its high spatial resolution, moderate energy resolution and temporal resolution. Through the successful operations and results by the *Chandra*/ACIS and *XMM-Newton*/EPIC, the X-ray CCD has also been the most reliable and stable detector in the X-ray astronomy.

At the time of writing this thesis, the X-ray Imaging Spectrometer (XIS) onboard *Suzaku*, the fifth Japanese X-ray astronomical satellite, is the brand-new, superior X-ray CCDs in orbit. Its low and stable particle background and good energy resolution are the complementary characteristics against those of the other X-ray CCDs in orbit: high spatial resolution of the *Chandra*/ACIS, large effective area of the *XMM-Newton*/EPIC.

We, the XIS team, have made experiments to improve the above performance and make correct energy redistribution function, which defines a mapping from the source photon energy to the detected pulse height amplitude (PHA).

Another advantage of the XIS is that it equips a register for the injection of artificial charge packets. Injection and subsequent readout of the charge packets

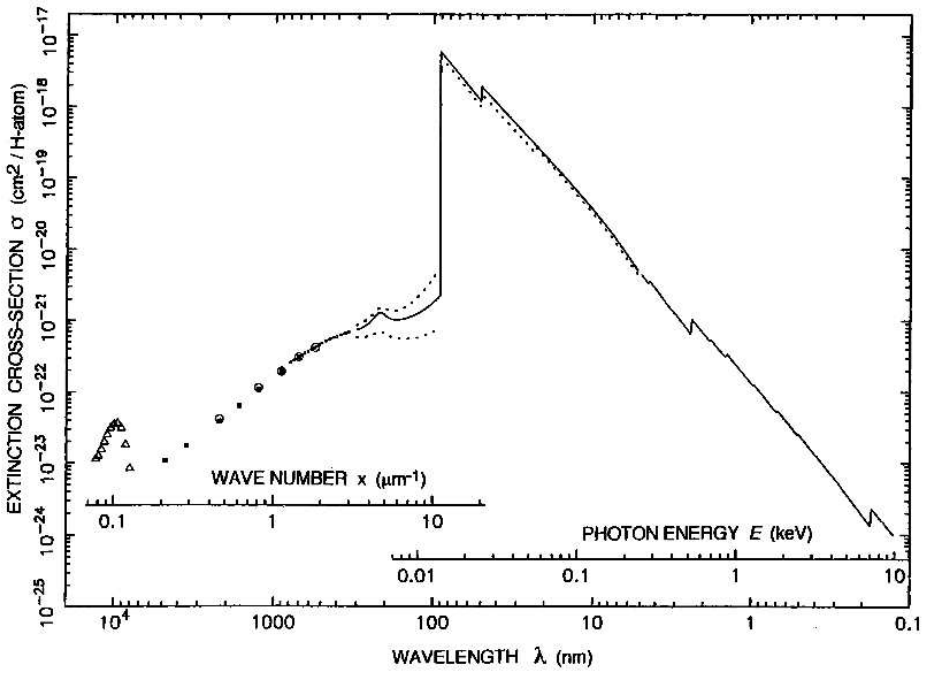

Figure 1.1: The extinction cross section by interstellar medium from far-infrared to the X-rays. Both of the absorption and scattering are included. This figure is adopted from Ryter (1996).

enable us to measure charge losses and/or mitigate charge traps in a transfer channel. Then, compensating the lost charges for each event leads to the precise estimation of the PHA, that is, the better gain and energy resolution. Because the degradation of the gain and energy resolution of X-ray CCDs in orbit is inevitable due to the radiation damage by charged particle, the charge injection (CI) capability can be the most powerful tool to have the advantage of other satellites.

Hot ionized gas is an essential component of the interstellar medium (ISM) and supernovae (SNe) and their remnants as well as the stellar winds from massive stars are the main site for the formation of the hot gas with a temperature from several 10^6 K to over 10^7 K. They interact with ISM through ionizing, accelerating, and heating up. The heavy elements are spread out by the SN explosions into the interstellar space, thus the X-ray spectra of young SNRs strongly reflect the abundance of ejected matter. As the SNRs get older, the amount of the ambient matter gathered up by their shock fronts. Hence the middle-aged SNRs show the X-ray spectra which characterize the abundance of the ambient ISM. More older SNRs are then considered to gradually lose their identities by merging into the ambient ISM. Thus, the ISM can be considered as the wreck of SNRs.

However, in most cases, SNRs occur spatially and temporally concentrated and near the massive stars. The enormous mechanical energy released by these stars through stellar winds and SNe creates a large pressure in the surrounding medium. The dense neutral ISM is displaced by low-density coronal gas, producing a super-

bubble (SB) surrounded by a dense ringlike supershell. Through the SB evolution, the front shocks of each SNR and strong stellar winds interact with each other producing the turbulence of plasma with a hundred to thousand parsec scale. The association of massive stars and successive SNRs potentially distribute around the galactic center, spiral arms, and other dense molecular clouds. Although detailed calculations of the evolution of SBs may differ depending on various assumptions about energy deposition and the interstellar environment, this qualitative picture generally holds. Because of its enormous energy and mass, SBs contribute large part of the energy input and chemical evolution of a galaxy. Therefore, we can trace the course of the formation of hot ISM in the galaxy by systematically investigating SBs and the site of SB formation as well as the hot ISM. Furthermore, the multiple front shocks in the hot and tenuous gas and their interaction inside SB lead the acceleration of cosmic rays (CR). Compared with the isolated SNRs, the duration of the acceleration is long and the particle injection rate to the acceleration site is more efficient, the SBs are one of the most possible candidates of the most powerful acceleration site of Galactic CRs.

Scope of this thesis is:

1. Bring out the superior performances of the XIS through ground and in-orbit calibrations.

2. Improve the in-orbit performance, especially the gain and energy resolution with the execution of the CI capability for the first time among the X-ray CCDs used for satellite.

3. Study the energetics and particle acceleration in the SBs by investigating some samples of SBs and multiple SNRs sites.

We will introduce the observatories which are used in this thesis including *Suzaku* in chapter 2 at first. The hardware portion of this thesis consists of chapter 3 which describes the detailed specification of XIS. The following chapter 4 and 5 are dedicated to explain the results of the ground- and in-orbit calibrations, respectively. The other part concerning SB consists of the review of SNR and SB formation and their evolution in chapter 6, our observation results in chapter 7, and the discussion in chapter 8. Finally the conclusion is shown in chapter 9.

Chapter 2

Observatories

2.1 *Suzaku*

Suzaku, the fifth Japanese X-ray astronomical satellite, was put into orbit on 10^{th} July, 2005 as the recovery mission of *Astro-E*, the launch of which was unsuccessful in 2000. It was developed at the Institute of Space and Astronautical Science of Japan Aerospace Exploration Agency (ISAS/JAXA) in collaboration with NASA Goddard Space Flight Center (GSFC), Massachusetts Institute of Technology (MIT), and other Japanese institutions. The spacecraft is in a near-circular orbit with an apogee of 568 km, inclination angle of 31.9°, and the orbital period of approximately 96 minutes. Its mass and length are about 1300 kg and 6.5 m along the telescope axis after the deployment of the extensible optical bench (EOB). Schematic views are shown in figure 2.1.

Suzaku is equipped with three scientific instruments: the Hard X-ray detector (HXD), the X-ray Imaging spectrometer (XIS), and the X-ray spectrometer (XRS). Although the basic specifications of these instruments are the same as those of *Astro-E*, some improvements have been performed. In spite of the loss of the XRS, the main instrument of *Suzaku*, just before its first light, *Suzaku* still has the wide-energy range of 0.2 - 600 keV, high energy resolution at low energy band, and an extremely low background level compared with other major X-ray satellites.

2.1.1 X-ray Telescope

Suzaku has five light-weight thin-foil X-Ray Telescopes (XRTs). One of them is dedicated for the XRS and is called XRT-S, although it is no more functional. The others are equipped for the XIS and are called XRT-I. They have been developed jointly by NASA/GSFC, Nagoya University, Tokyo Metropolitan University, and ISAS/JAXA. These are Walter type I grazing-incidence reflective optics consisting of compactly nested, thin conical elements as shown in figure 2.3. Because of the reflectors' small thickness, they permit high density nesting and thus provide large collecting efficiency with a moderate imaging capability in the energy range of 0.2 - 12 keV, all accomplished in telescope units under 20 kg each.

The XRTs are arranged on the EOB on the spacecraft in the manner shown in

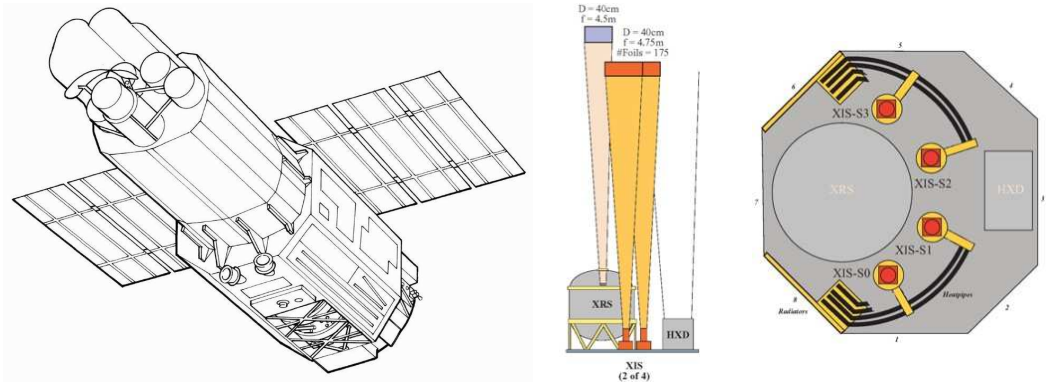

Figure 2.1: (Left panel:) Schematic picture of the bottom of the *Suzaku* satellite. (Middle panel:) Side view of the instruments and telescopes on *Suzaku*. (Right panel:) Top view of the instruments on *Suzaku*.

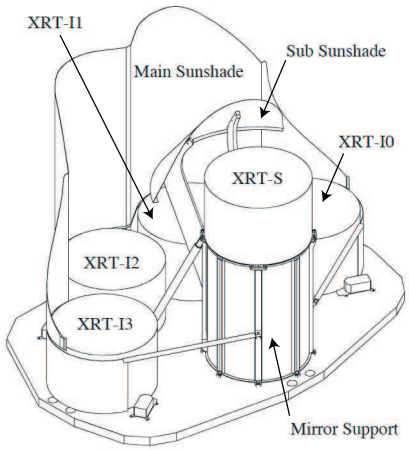

Figure 2.2: Schematic view of the XRTs mounted on the top plate of the EOB. The courtesy of K. Abe, NIPPI corporation.

figure 2.2. The external dimensions of the 4 XRT-Is, however, are the same. The angular resolutions of the XRTs range from 1.8′ to 2.3′, expressed in terms of half-power diameter, which is the diameter within which half of the focused X-ray is enclosed. The angular resolution does not significantly depend on the energy of the incident X-ray in the energy range of Suzaku, 0.2 - 12 keV. The effective areas are typically 440 cm^2 at 1.5 keV and 250 cm^2 at 8 keV. The focal lengths are 4.75 m for the XRT-I. Individual XRT quadrants have their component focal lengths deviated from the design values by a few cm. The optical axes of the quadrants of each XRT are aligned within 2′ from the mechanical axis. The field of view (FOV) for XRT-Is is about 17′ at 1.5 keV and 13′ at 8 keV.

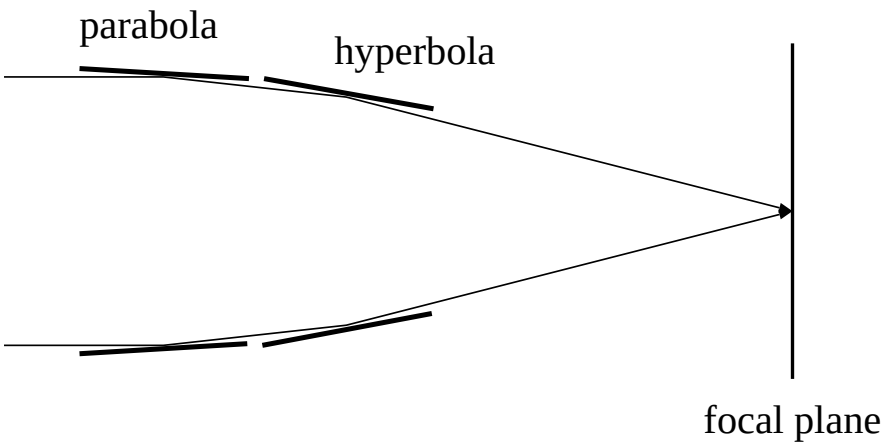

Figure 2.3: Walter type I optics. This is accomplished by two successive grazing-incidence reflections on a parabolic and a hyperbolic shaped metal surface.

2.1.2 X-ray Imaging Spectrometer

The XIS consists of the sensor, analog electronics (AE), and digital electronics (DE). The picture of the sensor is shown in figure 2.4. The readout analog signals from the sensor are transferred to the AE and converted into the digital signals. The digitized pixel data are transferred into the DE and then each X-ray event is extracted. The X-ray event information is formatted into telemeter data and transferred to the data processor.

All sensors of XIS were developed through the collaboration of the Center for Space Research (CSR) at MIT, ISAS/JAXA, Osaka Univ., Kyoto Univ., Rikkyo Univ., Kogakuin Univ., and Ehime Univ. The AE and CCD chips were developed at CSR and the Lincoln Laboratory at MIT, respectively. The upper part of the sensors (hereafter referred to as bonnet) and DE were developed by ISAS/JAXA, Osaka Univ., and Kyoto Univ.. The CCD calibrations have been done by MIT, Osaka Univ. and Kyoto Univ. Gain, energy resolution, and quantum efficiency (QE) have been investigated. After simple calibrations at MIT, the Osaka Univ. group has investigated the low energy ($\leq$Si K-edge $\simeq$ 1.8 keV) X-ray response of the sensors. At Kyoto Univ., the high energy ($\geq$Al Kα line $\simeq$ 1.5 keV) response has been intensively investigated.

Each sensor consists of an X-ray CCD camera combined with the single XRT. Three sets of XIS utilize front-illuminated (FI) chips, while the other is equipped with a back-illuminated (BI) chip (MIT Lincoln Laboratory model CCID41). All sensors including spare sensors utilize the three phase CCD, and the FI CCDs have basically the same chip structure as the ACIS-I chips onboard *Chandra* (CCID17; Bautz et al. 1996). Table 2.1 summarizes the specification of the XIS CCD chip.

There are several improvements against the XIS onboard *Astro-E* (Tsuru et al. 2000). First, the BI chip is used. The BI chip has the same basic specifications as the FI chips, except that it has a larger QE in the soft energy band as shown in figure

Figure 2.4: An outside view of the XIS sensor component.

Table 2.1: The performance description of XIS front-illuminated CCD chips.

Pixel Size	24μm×24μm
Pixel Number	1024×1024
Chip Size	25mm×25mm
Time Resolution	8 msec (Timing Mode), 8 sec (Normal Mode)

2.6. Furthermore, the BI CCD for XIS is treated with the chemisorption process developed by Lesser et al. (1998). Coating the thin ($\sim$ 1 nm) silver on the backside surface in a fabrication process, the silver catalyzes dissociation of the molecular oxygens leaving fixed, negatively charged oxygen atoms on the surface as shown in figure 2.5. Because of the potential due to these oxygen ions, the photoelectrons created around the backside edge of the depletion layer can be successfully drifted to the front surface. Hence, the BI CCD of XIS has almost the same energy resolution as FI CCDs in the soft energy band, while other BI CCDs such as ACIS-S onboard *Chandra* and pn-CCD onboard *XMM-Newton* have energy resolution worse than FI devices roughly by a factor of two.

Second, a charge injection (CI) capability is added (Prigozhin et al. 2004; Bautz et al. 2004; LaMarr et al. 2004). Injection of charge packets (CPs) into a transfer channel of the CCD and a subsequent readout process allow the charge transfer inefficiency (CTI) in each transfer channel to be measured. I will describe the performance of the CI capability in chapter 5 in detail. Here I describe the basic specification of the CI capability.

In order to maintain the performance of CCDs in orbit, the CTI must be frequently measured and corrected. Furthermore, the *ASCA*/SIS raised an important issue: The CTI varies significantly from column to column. Therefore some capability is needed such that the CTI can be measured for each column. Then, the CI structure was introduced to the *Astro-E*2/XIS (figure 2.7). The structure of CI

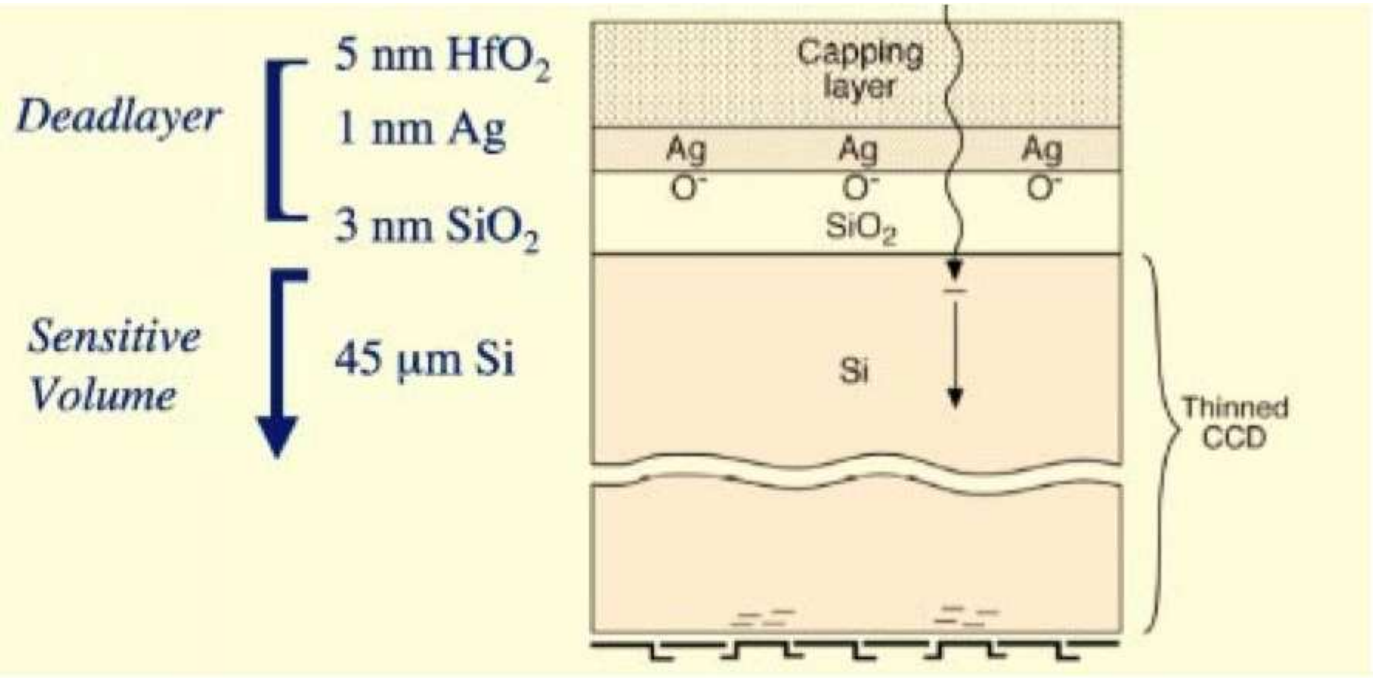

Figure 2.5: Schematic view of the back surface of the BI CCD chip treated with chemisorption process. This figure is adopted from Burke et al. (2004).

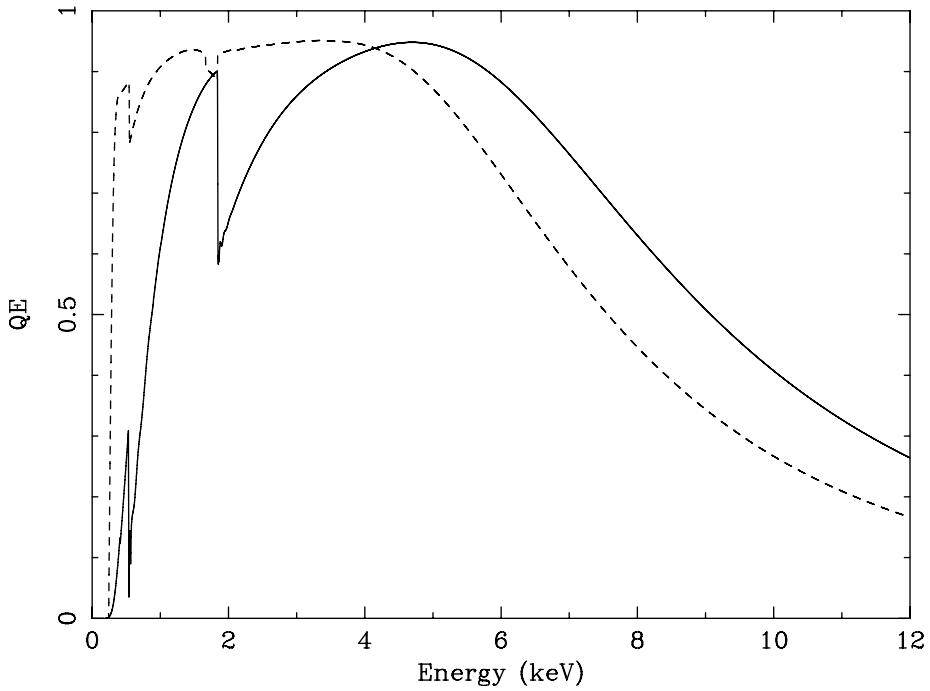

Figure 2.6: Quantum efficiency of the FI and BI CCD calculated from a CCD model with designed thickness of the electrode layer, insulation layer, and depletion layer.

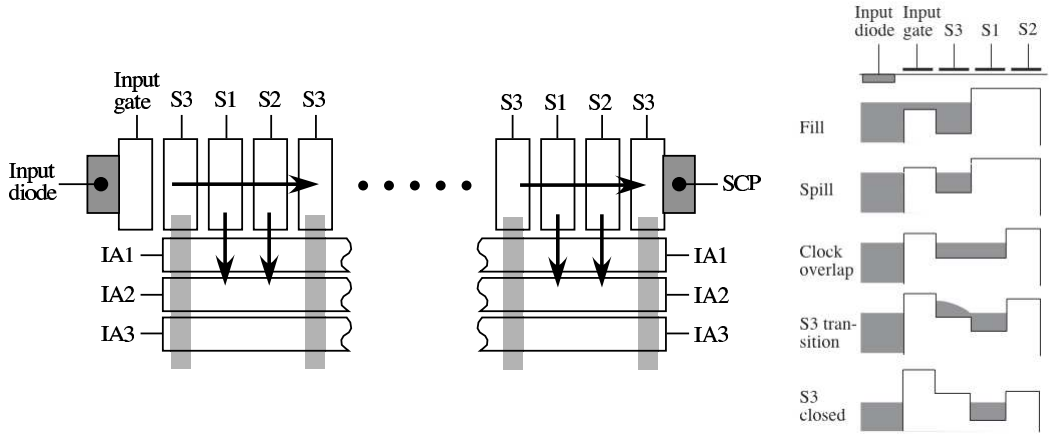

Figure 2.7: (Left panel:) Schematic view of the CI structure. The artificial charges are injected to the serial register from the input gate located at the edge of the register. After positioning the charges over the register, they are injected to the imaging area simultaneously by the vertical clock. (Right panel:) Schematic view of how to inject charges at the input gate. The amount of injected charges can be controlled by adjusting the offset voltage between the input gate and the S3 electrode.

register and how to inject charges are shown in figure 2.7. A serial register (hereafter CI register) equipped at the edge of the imaging area (IA) and an artificial charge packet can be injected from the input gate equipped at the edge of the CI register. Pulling down the potential for electrons at the input gate and the next electrode (S3 in figure 2.7), "fill" the bucket formed at the electrode. The amount of the injected charges can be controlled by the offset voltage between the input gate and the S3 electrode. Then "spill" the charges pulling up the potential. We repeat this "fill and spill" cycle with 1/40960 sec $\simeq$ 24 μsec in the normal manner. After positioning the packets in the register with a desired pattern, they are simultaneously transferred into the IA by vertical clock.

Another characteristics of XIS is the low background level. While *Chandra* and *XMM-Newton* suffer from the charged particle background, primarily low energy protons ($\sim$ 10 - 100 keV) in the van Allen belts (Plucinsky et al. 2000; Read & Ponman 2003), that of *Suzaku* is low and stable compared to other satellites due to the low earth orbit. Figure 2.8 shows the comparison of the non X-ray background between other satellites (*ASCA*, *Chandra*, and *XMM-Newton*).

2.1.3 Hard X-ray Detector

One of the main advantage of *Suzaku* is a spectroscopy in the wide energy band of 0.2 - 600 keV. The HXD takes charge of high energy band of 12 - 600 keV. The HXD consists of two detectors: 2 mm thick silicon PIN diodes sensitive over 10 - 70 keV, and GSO crystal scintillators placed behind the PIN diodes covering 40 - 600 keV. Figure 2.9 shows a schematic view of the HXD sensor. The HXD is composed of 16

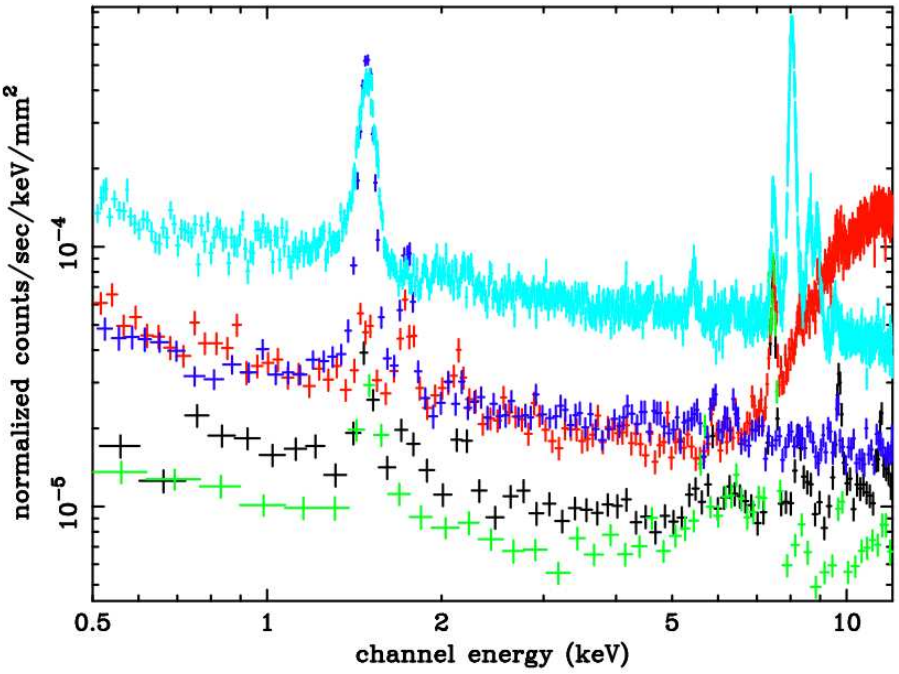

Figure 2.8: Internal background spectra of *ASCA*/SIS, *Suzaku*/XIS-FI, *Suzaku*/XIS-BI, *XMM-Newton*/MOS, *XMM-Newton*/pn. Each spectrum is normalized by the CCD area.

(4×4) identical detector units. The four sides of the detector units are surrounded by 20 thick anti-counters made of BGO scintillators for background shield. The anti-counters are also expected to detect transient high energy phenomena such as the gamma-ray bursts.

Inside of each well, passive fine collimators made of phosphor bronze sheet are placed to limit the FOV for soft X-rays (< 100 keV), so that the FOV becomes comparable to those of the XRS and XIS. The fine collimators are also expected to reduce the cosmic diffuse X-ray background, which otherwise might be a significant background source for the PIN diodes. With this collimator, the HXD achieves the lowest background level in this energy band ever as shown in figure 2.10. The detailed description of the detector and the results of the flight calibration of the HXD can be seen in Takahashi et al. (2006) and Kokubun et al. (2006).

2.2 *XMM-Newton*

The European Space Agency's $X-rayMultiMirrorMission-Newton(XMM-Newton)$ was launched by Ariane 504 on December 10, 1999. *XMM-Newton* carries three XRT with the largest effective area of a focusing telescope ever: The total mirror geometric effective area at 1.5 keV energy is 1550 cm^2 for each telescope, i.e., 4650 cm^2 in total (Jansen et al. 2001 for details). The main instrument, European Photon Imaging Camera (EPIC), is the CCD cameras, which have moderate spectral

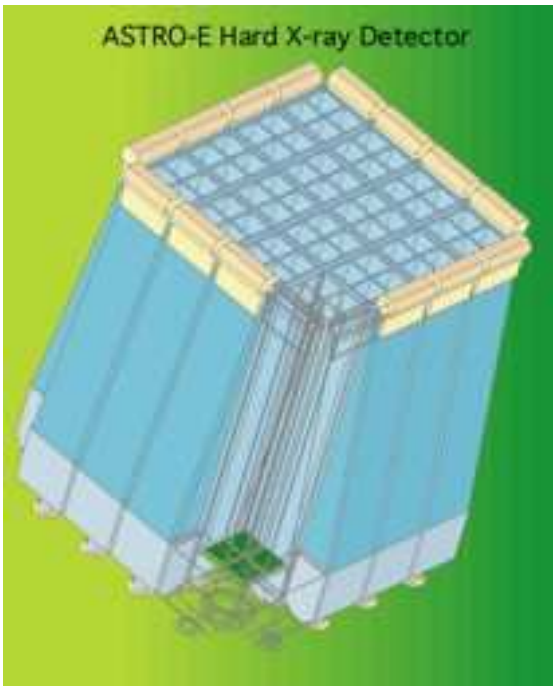

Figure 2.9: Schematic view of the HXD sensor component. The green and blue part is the PIN diodes and BGO crystal, respectively.

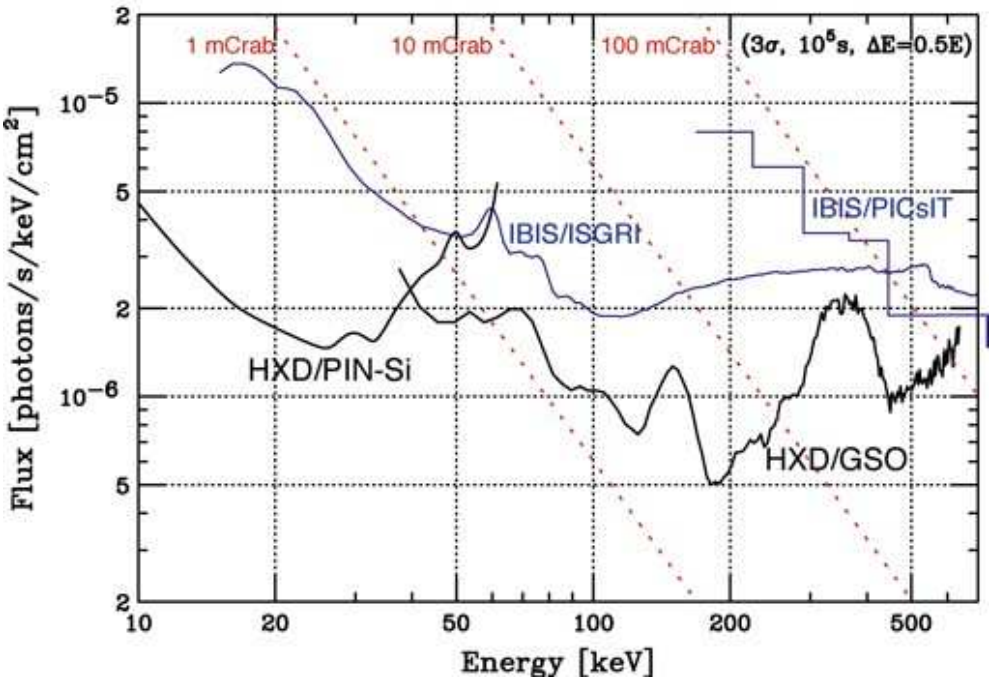

Figure 2.10: Predicted sensitivity of *Suzaku*/HXD vs. IBIS/ISGLI and IBIS/PlCsIT onboard *INTEGRAL* calculated on ground. 100 ks observation and the energy resolution of $\Delta E = 0.5E$ are assumed.

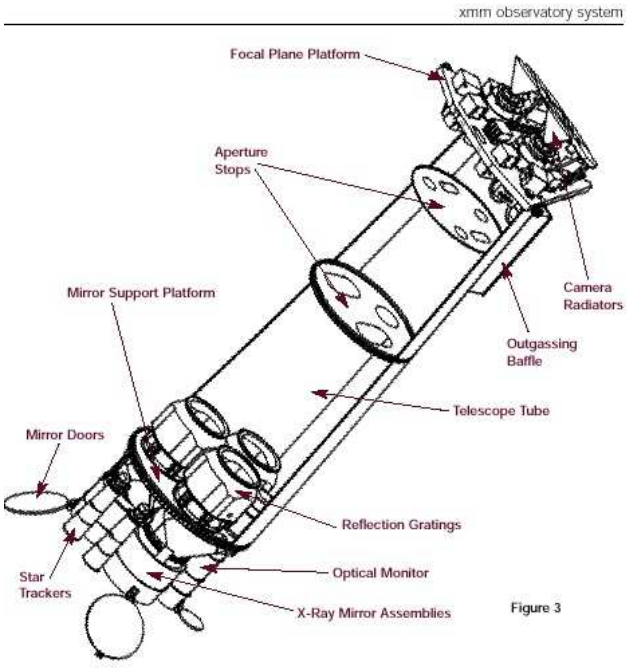

Figure 2.11: Schematic view of the *XMM-Newton* telescope. X-rays irradiate from the bottom-left XRT to the upper-right instruments.

resolution (with a resolving power, E/ΔE, of ∼ 20 - 50). The Reflection Grating Spectrometers offer much higher spectral resolution, with a resolving power in the range of 200 - 800. A highly elliptical orbit offers continuous target visibility of up to about 40 hours, with a minimum height for science observations of 46,000 km. This is very favourable for studies of source variability and also in order to achieve a high overall observatory efficiency.

2.2.1 X-ray Telescope

XMM-Newton's high sensitivity is achieved by using 58 thin nested mirror shells in each XRT. The XRT onboard *XMM-Newton* consists of three Wolter-I type X-ray telescopes that are co-aligned with a relative astrometry between the three EPIC cameras with the focal length of 7.5 m. They are calibrated to better than 1 - 2″ across the full FOV. The system is illustrated in figure 2.11. Two of them have grating assemblies in their light paths, diffracting a part of the incoming radiation onto their secondary focus. Values for the full width at half maximum (FWHM) and half energy width (HEW) of the PSFs and effective area of each XRT are listed in table 2.2.

Table 2.2: The on-axis performance description of XRT onboard *XMM-Newton* at 1.5keV.

Instr. chain	pn	MOS-1+RGS-1	MOS-2+RGS-2
FWHM (″)	<12.5	4.3	4.4
HEW (″)	15.2	13.8	13.0
Eff. Area (cm^2)	1380	520	520

2.2.2 European Photon Imaging Camera

Two of the *XMM-Newton* XRT are equipped with EPIC MOS (Metal Oxide Semiconductor) CCD arrays, the third carries a different CCD camera called EPIC pn. The EPIC cameras offer the possibility to perform sensitive imaging observations over an FOV of 30′ and an energy range from 0.15 to 15 keV, with moderate spectral resolution ($E/\Delta E \sim 20 - 50$).

Each of the MOS CCD arrays consists of seven FI CCDs. Each chip is a three phase frame transfer device and has an imaging area of 600 pixels × 600 pixels with the pixel size of 40 μm square, so that the FOV of a mosaic of seven chips is 28′.4. The mean depletion of the MOS CCDs is between 35 and 40 μm. Each camera is equipped with the calibration source of ^{55}Fe with Al-targets for the calibration of the absolute gain and it provides the Al Kα, Mn Kα, and Mn Kβ line. Holland et al. (1996) and Sembay et al. (2004) describe the specification and in-orbit performance of the MOS detectors in detail.

The heart of the EPIC pn camera is an array of 12 monolithically integrated pn-CCDs. The pixel size is 150 μm square, arranged in 200 rows by 64 channels forming a sensitive area of 6 cm × 6 cm. A 300 μm silicon wafer is fully depleted with a reverse biased pn-diode and reverse biased strip diodes at the opposite wafer surface. The large area diode acts as a homogeneous radiation entrance window. The pn-strip diodes (shift registers) are used for electron storage and transfer to the anode, similar to the MOS gates of the other CCDs. The detector is kept at a temperature of –90 °C.

The in-orbit FWHM of EPIC cameras of the Al Kα and Mn Kα on-board calibration lines is plotted in figure 2.12. The CTI correction is already applied. This shows a degradation of approximately 13% in the energy resolution of the MOS since the launch. In this point the EPIC MOS is a formidable competitor for the XIS.

2.3 *Chandra*

The *Chandra* X-ray Observatory was deployed by the Space Shuttle Columbia on the 23 of July 1999. The *Chandra* spacecraft carries a high resolution mirror, two imaging detectors, and two sets of transmission gratings. Important *Chandra* features are spatial resolution of $< 1''$ and good sensitivity from 0.1 to 10 keV for point

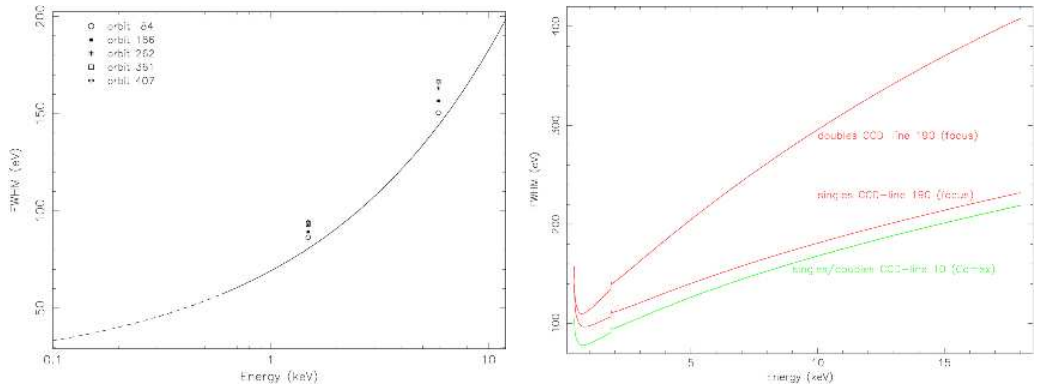

Figure 2.12: (Left panel:) EPIC MOS FWHM as a function of energy. The solid curve is a best-fit $E^{0.5}$ function to ground calibration data between 0.1 - 12.0 keV. (Right panel:) EPIC pn FWHM as a function of energy as present in the response matrices. Curves are given for single- and double-pixel events at the focus position as well as at a position 10 pixels away from the readout node.

sources. *Chandra* is in an elliptical high-earth orbit allowing observing intervals of more than 48 hours in length. The details for the satellite and instruments are described by Weisskopf et al. (2002).

2.3.1 X-ray Telescope

The mirror consists of four pairs of nested reflecting surfaces, arranged in the usual Wolter-I type geometry. The high energy response is achieved by use of relatively small reflection angles and by coating the mirrors with iridium. Improvements in mirror technology since *Einstein* include advances in grinding, polishing, alignment, and testing. Mirrors with resolution of 0.5″ have been achieved.

2.3.2 Advanced CCD Imaging Spectrometer

The Advanced CCD Imaging Spectrometer (ACIS) offers the capability to simultaneously acquire high-resolution images and moderate resolution spectra. The instrument also is used in conjunction with the High Energy Transmission Grating (HETG) or Low Energy Transmission Grating (LETG) to obtain higher resolution spectra. ACIS contains 10 planar, 1024 pixels × 1024 pixels CCDs; four arranged in a 2×2 array (ACIS-I) used for imaging, and six arranged in a 1×6 array (ACIS-S) used either for imaging or as a grating readout. Any combination of up to 6 CCDs may be operated simultaneously. Two CCDs are BI chips and eight are FI chips. The response of the BI devices extends to energies below that accessible to the FI chips. The chip-averaged energy resolution of the BI devices is better than that of the FI devices in a high energy band.

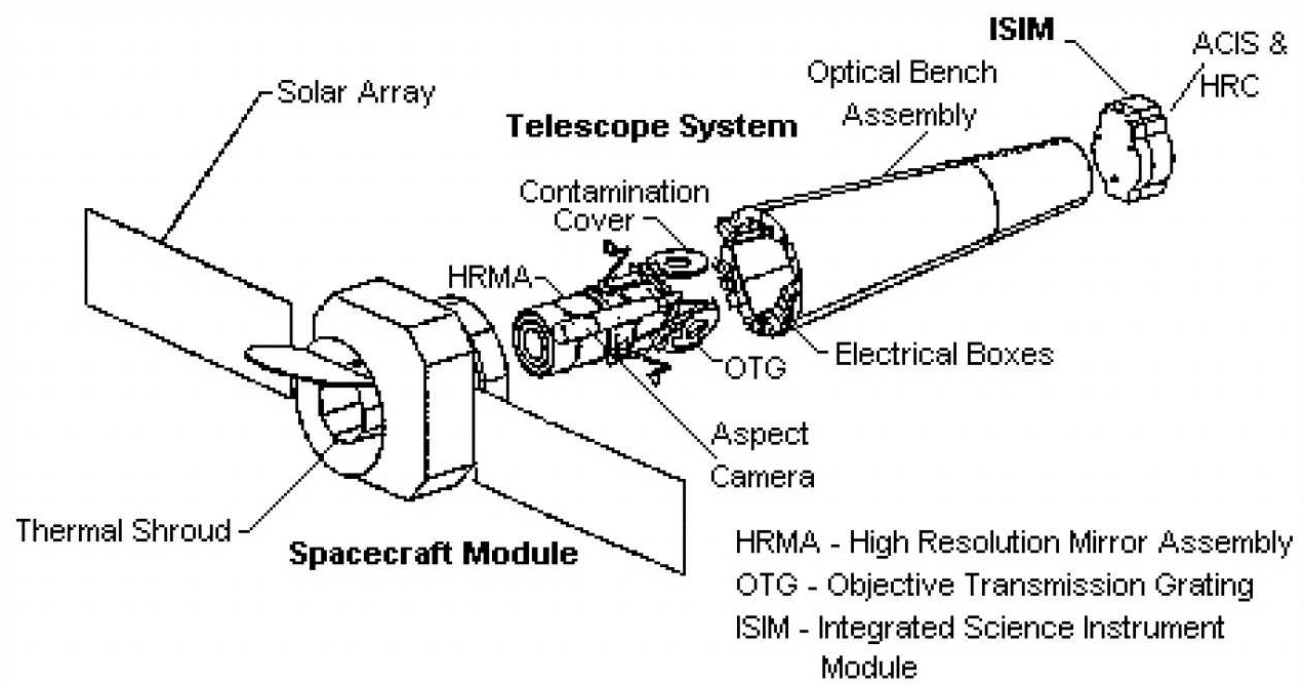

Figure 2.13: Schematic view of the *Chandra* spacecraft with an exploded view of the science instruments.

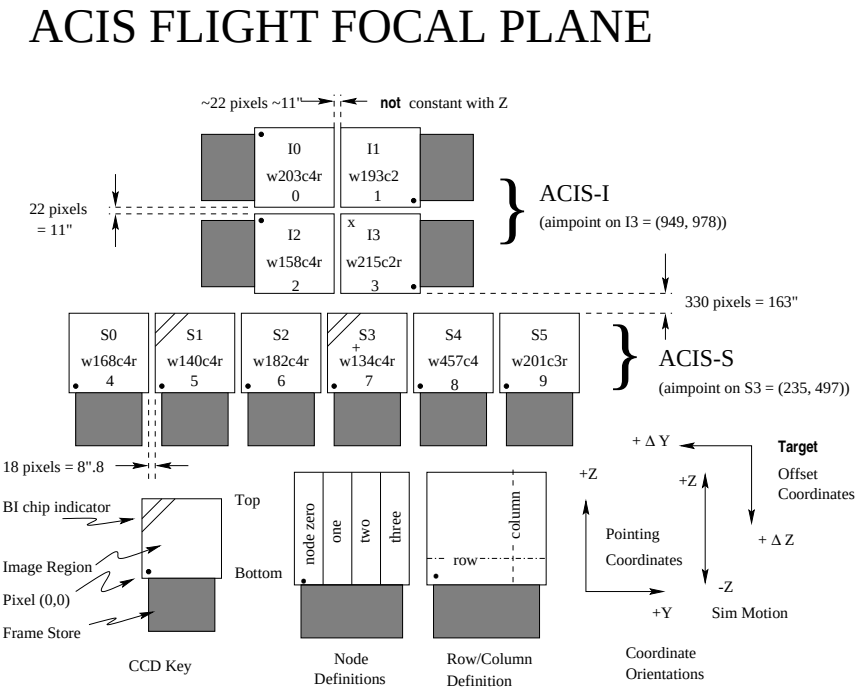

Figure 2.14: Schematic view of the ACIS focal plane. The nominal aimpoints for "imaging" and "grating" mode are marked with cross on S3 and I3 chip, respectively.

Chapter 3

XIS

Here I describe the detail of the XIS and its components.

3.1 Basic Structure of the XIS

XIS camera body consists of a hood, bonnet, and base as shown in figure 3.1. The hood has five baffles to block stray light. The bonnet includes a vacuum valve, an optical blocking filter (OBF), calibration sources, a pressure sensor, a paraffin actuator, and a door. The base contains an X-ray CCD mounted on an alumina (Al_2O_3) substrate and is attached to a heat sink assembly made of copper (Cu). Over the frame-store region (FS) of the CCD, an aluminum (Al) shield with a gold (Au)-plated nickel (Ni) surface treatment is placed to block X-ray irradiation. The surfaces of the substrate, the heat sink assembly, and the shield are also plated with Au. The bonnet and the hood are made of Al with black surface finish. The inside of the base is Ni-plated, except for the feed-through plate which is Au electro-plated. The XIS sensor is covered by multi-layer insulators to reduce heat-flow from the satellite body.

The XIS CCD are sensitive to optical and ultraviolet light as well as X-rays, and hence have an OBF 20 mm above the IA. The OBF is made of a polyimide ($C_{22}H_{10}N_2O_4$) film with vapor-deposited Al on both sides, in order to avoid light leakage from pinholes. The thicknesses of the Al on the two sides of the filter are different from each other. This reduces the light transmission by the interference effect (Born & Wolf 1999). The thickness of the polyimide film and Al layers are $\sim 1400\mathring{A}$ and $\sim 800\mathring{A} + 400\mathring{A}$, respectively. This realizes a low transmission coefficient for optical light ($\leq 5 \times 10^{-5}$), but is transparent to X-rays ($\geq 80\%$ above 0.7 keV). The measured transmissions for optical light and soft X-rays are reported in Kitamoto et al. (2004). Since the OBF is very fragile and vibrations during launch may destroy it; at the time of the launch, the vicinity of the chip and the OBF was kept in an air-tight vacuum by closing a door equipped with the bonnet. The door was opened by the paraffin actuator after 18 days from the launch.

The X-ray CCDs generally suffer from dark current due to the thermal excitation of electrons and the small energy band gap of Si semiconductor crystals (1.12 eV). Then, a three-stage thermo-electric cooler (TEC; Peltier sensor) is used to cool the

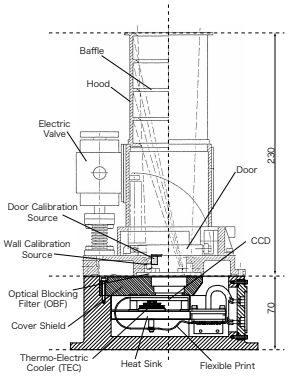

Figure 3.1: Schematic view of the XIS sensor component. The single-hatched and cross-hatched regions are bonnet and base, respectively.

Figure 3.2: The CCD and heat sink assembly of the BI CCD flight model. The cover shield and base are removed in this picture. The bottom stage of the TEC can be seen under the CCD.

CCD to the nominal operating temperature of $-90°$C. The cold-end of the TEC is directly connected to the substrate of the CCD, which is mechanically supported by three Torlon posts (polyamide-imide plastic) attached to the head sink. The heat is transferred through a heat pipe to a radiator panel on the satellite surface, and is radiated away to space. The radiator and heat pipe are designed to cool the base below $-40°$C under the nominal TEC operating conditions. Figure 3.2 is a photograph of the BI CCD flight model on the heat sink assembly with the frame-store cover shield removed. The flex cable put at the bottom of the chip is seen at the left side. The bottom stage of the TEC can be seen under the FS region of the CCD.

Each XIS sensor has three ^{55}Fe calibration sources. One is attached to the door, and illuminates the whole IA almost uniformly. This calibration source was used on the ground and for initial in-orbit calibration before the door was opened. For

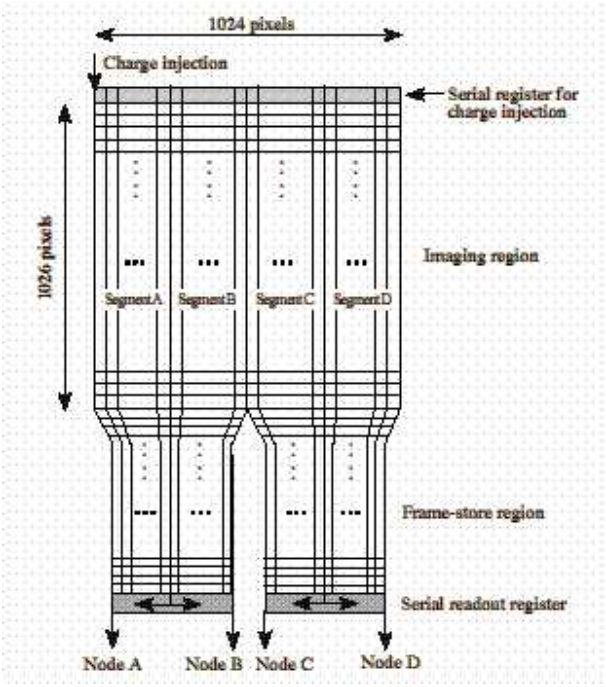

Figure 3.3: Schematic view of the CCD chip. A serial register is equipped at the top of the imaging area for CI capability. The chip has four read out nodes. Signals are readout simultaneously from these nodes.

normal observations, after the door is open, this source is out of the FOV of the CCD. The other two calibration sources are located on a side wall of the bonnet and illuminate the two far-end corners of the IA from the readout node. The fluxes of the these calibration sources were selected so that the gain can be determined at 5.9 keV with a statistical error of 0.1% within a single orbit early in the mission.

3.2 Specifications of X-ray CCDs

In order to see the function of the CCD, we give the schematic view of the XIS FI chip in figure 3.3. Each CCD chip has four segments (from A to D), and each segment has one readout node. A simplified model of the dead layers in the FI devices, in which the gate structure is approximated as a stack of nearly uniform slabs, has been fit to the ground calibration data. Then the dead layer thicknesses of $\sim$0.28 μm (Si) and $\sim$0.44 μm (SiO_2) are inferred. The surface dead layers of the BI CCD is very thin, consisting of 5 nm of HfO_2, 1 nm Ag, and 3 nm SiO_2. As for the depletion layer thickness, the ground calibrations verified that the thickness of the depletion layer is $\sim$ 65 μm for the FI chips, and $\sim$ 42 μm for the BI chip. This leads the QEs for the FI and BI CCDs as a function of energy as shown in figure 2.6.

Position in the IA is defined by the detector-fixed coordinates (ActX, ActY), where the origin (0, 0) is taken to be the first pixel readout of segment A in normal

clocking mode. The positive directions are shown by arrows in figure 3.3. In the IA, ActX runs from 0 to 1023 (from segment A to D), while ActY runs from 0 to 1023 (from the readout node to the CI register).

In this thesis, we converge to the description and experiment results of the normal clocking mode and 5×5/3×3 edit mode because most of the observations is conducted with the above configurations.

3.2.1 Transfer Mechanism

In the normal clocking mode of frame transfer type CCDs, after the exposure is over, the charge in the IA is transferred at a high speed into the X-ray shielded FS region (FS transfer). Once the FS transfer is completed, the IA begins its next exposure while the FS is slowly readout. The readout is accomplished by transferring the FS region row by row into the serial register (parallel transfer), where each row is clocked out serially into an output node (serial transfer).

3.2.2 Event Detection

When a CCD pixel absorbs an X-ray photon, the X-ray is converted to an electric charge, which in turn produces a voltage at the analog output of the CCD. This voltage ("pulse-height amplitude"; PHA) is proportional to the energy of the incident X-ray. In order to determine the true PHA corresponding to the input X-ray energy, it is necessary to subtract the Dark Levels and correct possible optical Light Leaks. Dark Levels are non-zero pixel PHA caused by leakage currents in the CCD. After each passage of South Atlantic Anomaly (SAA), the bias-level is determined for each pixel by taking average of the PHA during an exposure of about ten frames.

Another components of the bias-level is the light leak level. Optical and UV light might enter the CCD due to imperfect shielding ("light leak") and produce PHA that is not related to X-rays. The Light Leaks are calculated on board with the PHA data after the subtraction of the Dark Levels. Analysis of the *ASCA* SIS data showed that light leaks are considered to be rather uniform over the CCD, hence an average is calculated for 256×114 pixels (this size was 64×64 before January 18, 2006) in every exposure and its running average produces the Light Leak. In spite of the name of Light Leak, Light Leak does not represent in reality the optical/UV light leak to the CCD. It mostly represents fluctuation of the CCD output correlated to the variations of the satellite bus voltage. XIS has little optical/UV light leak, which is negligible unless the bright earth comes close to the XIS field of view.

The main purpose of the on-board processing of the CCD data is to reduce the total amount transmitted to ground. For this purpose, the DE searches for a characteristic pattern of charge distribution (called an event) in the pre-processed (post- Dark Levels and Light Leaks subtraction) frame data. When an X-ray photon is absorbed in the depletion layer with photo-absorption process, a primary electron cloud with a size of $\leq 1\mu$m is produced. The primary cloud grows in size to $\leq 5\mu$m as it drifts toward the electrode. Because the sizes of the clouds at the electrode are smaller than the pixel size, most of the clouds are captured by four neighboring pixels

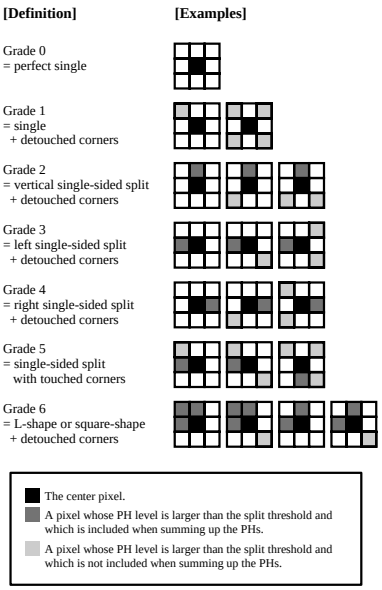

Figure 3.4: Grade definition and the rule to add PHA. The events out of these criteria are defined as Grade 7 to 11.

at most. An event is recognized when a valid PHA (one between the Event Lower and Upper Thresholds) is found that exceeds the PHA in the eight adjacent pixels. Then, the pulse height patterns around the local maximum pulse height pixels are classified into 12 kinds of so-called grades on ground. At the time of writing, the events classified as Grade 0, 2, 3, 4, and 6 (figure 3.4) are only regarded as X-ray events. On the other hand, charged particles events produce a larger electron cloud than X-ray events, hence the events are regarded as grade 7 or larger.

Determining the optimum split threshold level (figure 3.4) is important to measure the pulse height correctly. In the section 4.3, I will describe the results on the ground calibration to determine the optimum value.

3.2.3 Energy Resolution

Although the number of electron-hole pairs created is a function of the energy of the X-ray, it is a statistical process and there is a normal distribution around the actual X-ray energy. The energy resolution of the Si crystal detector is followed by

$$\mathrm{FWHM}(eV) = \sqrt{8\ln 2} \times W \sqrt{N^2 + \frac{E_0 F}{W}}, \tag{3.1}$$

where W is an energy required for one electron-hole pair creation (3.65 eV/pair), N is a rms readout noise in electrons, E_0 is an incident photon energy, and F is the Fano factor, which is the ratio of the observed statistical dispersion of the electron number to E_0/W, that is, the deviation from the Poisson statistics in the electron-hole creation process. Actually W and the Fano factor for Si semiconductor has

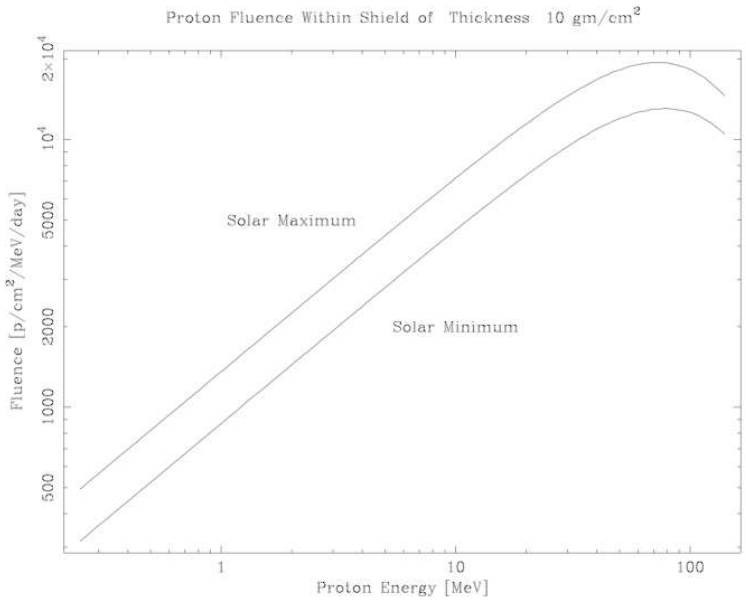

Figure 3.5: The predicted proton spectrum inside a simple model of the XIS shielding. The shielding is assumed to be spherically symmetric with a thickness of 10 g cm^{-2}.

the energy and temperature dependance. According to a Monte Carlo simulation, the former varies from $\sim$ 4.0 to $\sim$ 3.65 in the soft energy band of 0.1 - 2.0 keV, while nearly constant ($\sim$ 3.65) in the high energy band of 2.0 - 10.0 keV. The latter ranges from 0.08 to 0.16 according to various experiments (Knoll (1989) and references therein).

3.2.4 Radiation Environment

Suzaku operates in a low earth orbit with several daily passes through the SAA. The initial orbit is 568 km at an apogee, which is very close to that of *ASCA* (an apogee of 613 km). Results from a NASA charged particle environment study of the predicted *ASCA* orbit (Stassinopoulos & Barth 1991) indicated that geomagnetically trapped protons are the greatest concern for radiation damage. Figure 3.5 shows the predicted proton spectrum incident on the CCDs based on this study assuming a shielding depth of 10 g cm^{-2}. Figure 3.6 shows the specific energy loss for protons in silicon. Integrating the product of figure 3.5 and 3.6 yield the daily dose in "rads" of silicon expected to be about 0.5 rads per day (A rad is a unit of energy loss equal to 100 ergs per gram).

3.2.5 Charge Injection Capability

One drawback to an X-ray CCD in-orbit is the degradation of the gain and energy resolution due to an increase of the CTI and dark current. When a proton dislodges

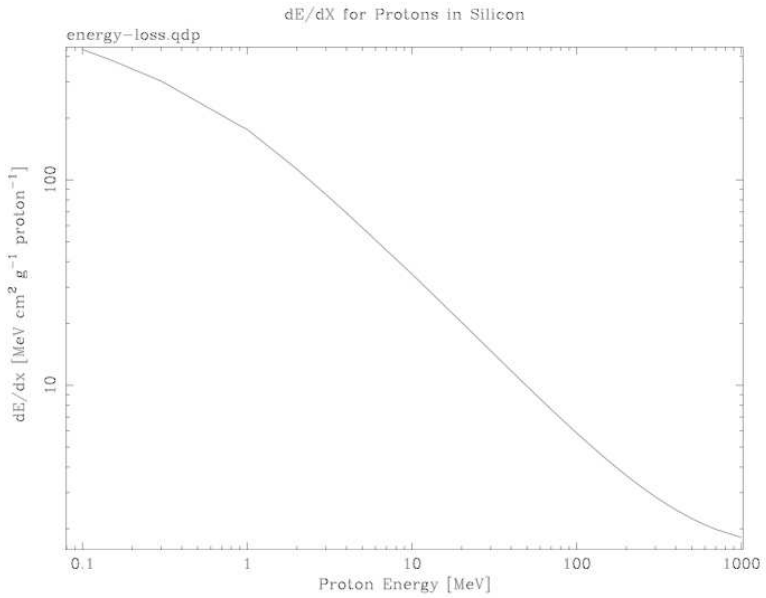

Figure 3.6: The specific energy loss for protons in silicon.

a silicon atom in the lattice of the CCD, the vacancy produced is fairly mobile.It will move through the lattice and possible reach the edge of the lattice where it is no longer a vacancy. Sometimes, the vacancy will come into the vicinity of another vacancy or an impurity atom also in the lattice. Often, the pair will form a complex which have a minimum energy and become physically stuck at a localized position in the lattice. The complex modifies the silicon band gap structure of the local lattice by introducing a mid band gap energy level, which is regarded as a charge trap (CT). The exact energy of this CT depends on the components of the trap complex. This defect is especially severe for low-energy protons because they deposit more energy than high-energy protons in the CCD transfer channel. The main origin of the CTI and consequent gain degradation is the increase of CTs. In fact, soon after the launch of the *Chandra*, all of the FI CCDs of the ACIS suffered the degradation of the CTI. Devices similar in type to ACIS CCDs have been tested by the high-energy protons (10 - 40 MeV) but not by the low-energy protons before the launch. The low-energy protons with an energy of $\sim$150 keV release a major part of their energy at the transfer channel of the ACIS CCDs, which is located roughly 1 μm below the electrodes. Although a thick shielding around the CCD camera can significantly reduce the proton flux on the CCD, the radiation damage cannot be ignored over a mission lifetime of several years.

Recently a CI technique has been developed (Prigozhin et al. 2004; Bautz et al. 2004; LaMarr et al. 2004; Smith et al. 2004; Meidinger et al. 2000). In principle, CPs are artificially injected through a CI gate (Tompsett et al. 1975) into each transfer channel (hereafter, we call this vertical transfer channel a column, and the horizontal channel a row) and are subsequently read after the charge transfer in the same manner as the X-ray events. This method allows the amount of charge loss

(δQ) on a column-to-column basis to be measured and/or mitigated, which in turn, can potentially be a powerful tool for CTI calibration. By referring to figures 3.3 and 2.7, here I explain the essential function of CI. For the brevity to describe the CI technique and its results, notations of parameters, which will be frequently used in this paper are listed in table 3.1.

Table 3.1: The notation list of parameters for the CI.

Parameters	Notation
Injected charge (for each column)	Q ($Q_{\rm COL}$)
Readout charge (for each column)	Q' ($Q'_{\rm COL}$)
Charge loss in the transfer (for one column)	δQ ($\delta Q_{\rm COL}$)
Charge Transfer Inefficiency (for one column)	CTI ($\rm CTI_{COL}$)
column-dependent CTI obtained with CI	$\rm CTI_{CI}$
column-averaged CTI obtained with the cal. source	$\rm CTI_{CAL}$

Because a fraction of the charge (δQ) is lost due to the CTs in the transfer channel, the readout charge (Q') is Q' =Q-δQ. On the other hand, we need the information of δQ in order to estimate the CTI. We hence need to adopt the injection pattern with which we can know both of of Q' and Q simultaneously with normal readout. Then we employ the following CI. After injecting a *test* CP with charge Q in one row, we inject the same charge (Q) in five subsequent rows: the preceding four rows are called the *sacrificial* CPs and the last one is the *reference* CP. Figure 3.7 shows a schematic view. The *test* charge is separated from trains of *sacrificial* charges at the request of the event detection algorithm.

The *test* charge Q may suffer from traps in the transfer channel (column), and therefore, the readout charge ($Q'_{\rm test}$) should be Q-δQ. On the other hand, the preceding *sacrificial* charges may fill the CTs, and hence, the subsequent *reference* charge Q may not be trapped if the clocking time is shorter than the de-trapping time scale (Gendreau et al. 1993), which is the time until the trapped charge is emitted to the conduction band.

We put the four CPs as *sacrificial* charges because if the loss in the first packet is large, the following packet may also lose some charge because as the first packet loses electrons, it occupies smaller volume and does not fill some of the traps inside the volume of the following larger packet. This effect can be seen in figure 3.8, which shows the PHA of the injected CPs before the dark-level subtraction as a function of Y coordinate averaged among columns in an arbitrary segment of the proton damaged chip (the ground experiment is described in chapter 4). This confirms that the technique of the *sacrificial* charges works well and four pixel is sufficient as the *sacrificial* CPs satisfy the technique. Figure 3.8 also shows the emission of trapped electrons back into the empty potential wells as a tail after the last injected packet.

Thus, the readout charge ($Q'_{\rm ref}$) from the *reference* CP should be approximately equal to Q. Figure 3.9 shows a frame image taken during our experiment. The positions of the CP trains are periodically shifted by one column and the *sacrificial*

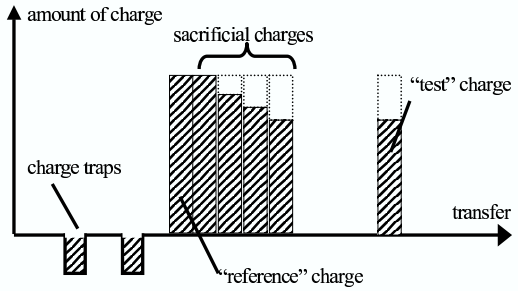

Figure 3.7: Schematic view of how to measure δQ using the *test* and *reference* charges. The amount of lost charges (δQ) can be estimated by comparing the PHA of *test* charge, which suffer from CTI, to that of *reference* charge, which is not affected by the traps.

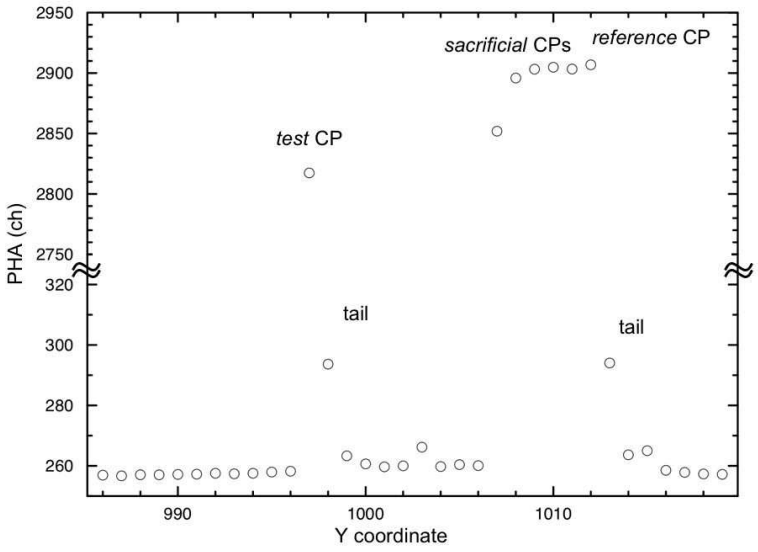

Figure 3.8: The PHA of injected charges averaged among columns in an arbitrary segment (seg.C) of the proton-damaged chip as a function of the Y coordinate. The vertical axis is chopped for the brevity.

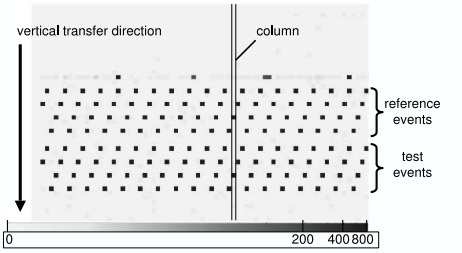

Figure 3.9: Frame image of the XIS during the CI experiment. The gray scale shows the pixel level, not the number of events. There are two events per each column: The lower one is the *test* charge and the upper one is the *reference* charge. Note that the sacrificial charges are not displayed at the request of the event detection algorithm.

CPs are not shown to allow the proper event detection algorithm. δQ during the transfer can be measured by the ratio of mean pulse height amplitude (PHA) of the *test* CP to that of the *reference* CP. By selecting different Qs, we can investigate the relation between Q and δQ. The results of the ground and in-orbit experiments on the CI capability will be described in section 4.6 and 5.2.

3.3 Charge Transfer Inefficiency

Shockley-Read-Hall theory (Shockley & Read 1952) describes the dependance of minority carrier capture and release time scales on temperature and carrier density. Traps capture electrons from passing charge packets on a capture time scale (t_c) is.

$$t_c = \frac{1}{v_t n \sigma}, \tag{3.2}$$

and the traps then release the captured electrons on an escape time scale (t_e) of

$$t_e = \frac{1}{v_t N_c \sigma e^{\frac{-(E_c - E_t)}{kT}}}. \tag{3.3}$$

The resulting trap occupancy rate is given by

$$\frac{dn_t}{dt} = -\frac{n_t}{t_e} + \frac{N_t - n_t}{t_c}, \tag{3.4}$$

where σ is the electron capture cross section, v_t is the thermal velocity of an electron, n is the number density of free electrons, N_c is the density of states in the conduction band, E_c is the band gap, E_t is the trap energy, k is Boltzmann's constant, T is the temperature, n_t is the number density of trapped electrons, and N_t is the number density of traps.

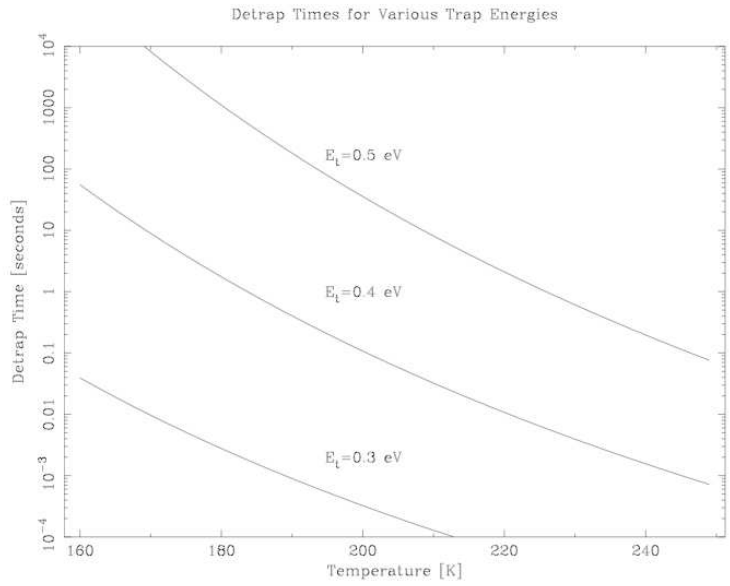

Figure 3.10: The detrapping times for traps of various energies as a function of temperature. The P-V center trap has an energy level of 0.3, 0.4, and 0.5 eV. The trap cross section is 3.5×10^{-15} cm^{-2} for each curve.

The phosphorus-vacancy (P-V) complex is a displacement induced trap which is the most significant in the phosphorus doped buried channels of CCD such as devices used in ACIS and XIS. The proton induced lattice vacancies combine with the phosphorus atoms and make P-V complexes. The P-V trap is characterized with a cross section of 3.5×10^{-15} cm^{-2} and a trap energy of $\sim$0.4 eV. With such a trap and a typical CP of 1000 electrons, the capture time is virtually instantaneous (less than 10^{-7} s) compared to transfer rates used in our devices (24 μs per shift). However, as shown in equation 3.2, trapping time is a function of the density. For small CPs (0 - 10 electrons for dark current and 50 - 3000 for X-ray signals), the density of electrons is difficult to calculate. However, the density should be within an order of magnitude of the phosphorus dopant density (2×10^{16} cm^{-3}). The detrapping times, however, are on the order of tens of milliseconds.

Figure 3.10 shows the detrapping times for traps of various energies as a function of temperature, using equation 3.3.

The P-V center trapping model explains the amount of charges, proton fluence, clock speed, and temperature dependance of our X-ray CCD performance. When a CP from an incident X-ray encounters an empty trap during a CCD readout, if the trapping time is sufficiently shorter than the time the CP is shifted away, it is very possible that the trap is left full and the CTs will contribute little to the gain and energy resolution. Each trap has a capacity to hold a single electron. Given an empty trap, the probability that a passing CP will lose an electron is nearly unity.

Once a CP has suffered a loss to a trap, if the detrapping time is long compared to the time till the next X-ray induced CP arrives, the trap will remain filled and

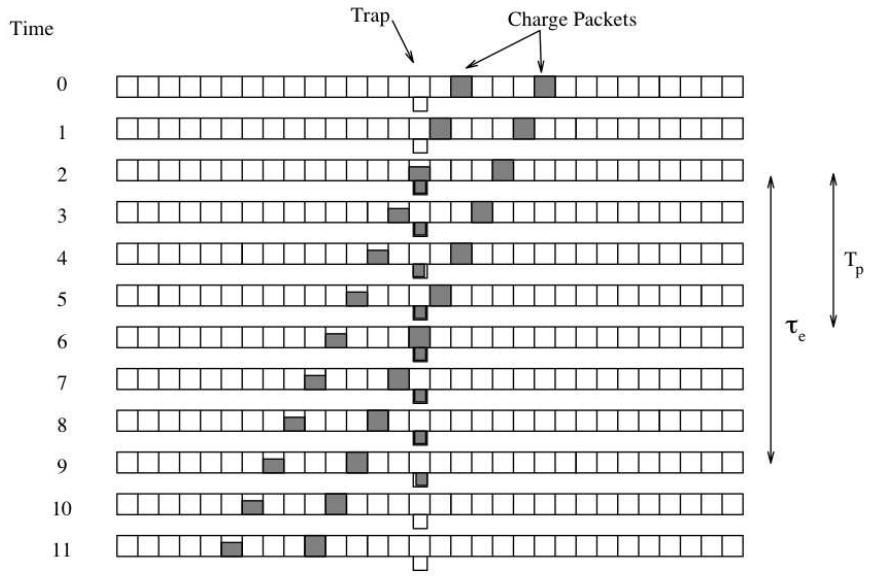

Figure 3.11: The case where only the preceding charge packet lose electrons to a given trap. The detrapping time is greater than the time between passing charge packets.

will not affect the second CP; thus minimizing the spectral degradation. If the detrapping time is short compared to the time till the next X-ray induced CP arrives, the trap will probably have emptied and would have a chance to degrade the second CP, and hence maximizes the damage to the spectral response. The former situation is shown in figure 3.11.

In this section, we call the preceding CP in figure 3.11 a *sacrificial* CP and following CP in figure 3.11 a *beneficial* CP. Figure 3.12 shows the spectra of ^{55}Fe data collected from the data obtained in 2005 (upper panels) and 2006 (bottom panels) in-orbit. We chose the ^{55}Fe data of XIS2 from the statistical point of view. As the distance between a *sacrificial* CP and *beneficial* CP increase (from (a) to (c) in figure 3.12), the line center of *sacrificial* CPs decrease against *beneficial* CPs. In other words, charges are lost with increasing distance between two CPs because increasing distance corresponds to an increasing time and an increasing probability that the traps filled by the *sacrificial* CP have trapped.

Because the XIS utilizes the frame transfer type CCD, even if the distance between the *sacrificial* CP and *beneficial* CP is fixed, the amount of lost charge is different among ActY. This is because the number of slow parallel transfer in the FS depends on ActY. Furthermore, the difference of the pixel sizes between the IA and FS makes more difficult to investigate the charge loss at each region. The total number of traps seen by CPs as a function of the distance to the *sacrificial* CP can be formulated as followings (Gendreau 1995) with an assumption that a trap can contain at most one electron.

Consider two CPs in one column of the IA. Both the IA and FS have N pixels.

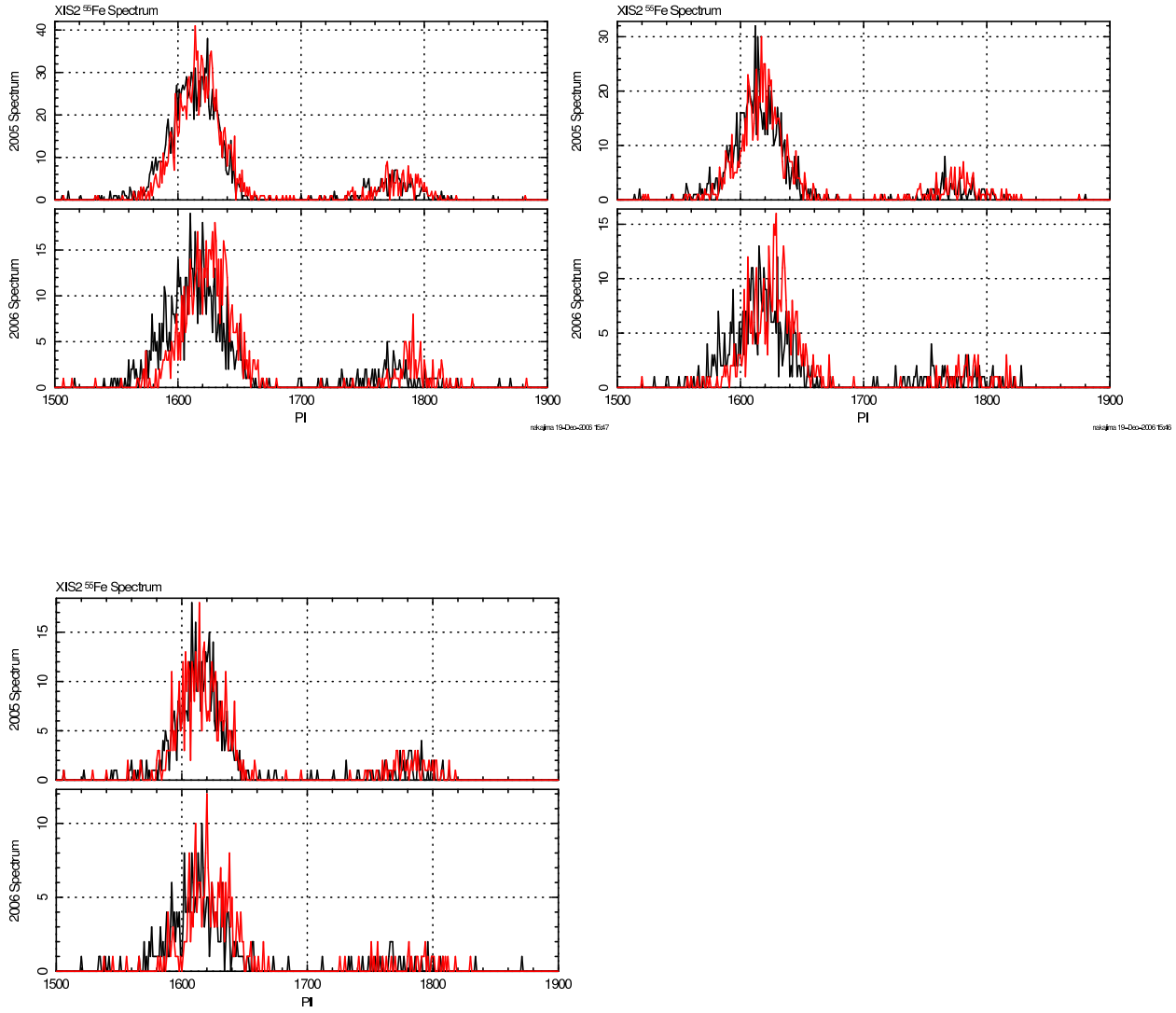

Figure 3.12: Energy spectra of ^{55}Fe events of XIS2 collected in orbit. For each figure, upper and bottom panels is the data collected in 2005 (from August to December) and 2006 (from January to June), respectively. The distance between a *sacrificial* CP and *beneficial* CP is shorter than 50 pixels (upperleft panel), from 50 to 100 pixels (upperright panel), and larger than 100 pixels (bottomleft panel). The black and red spectra show those of *sacrificial* CPs and *beneficial* CPs, respectively.

The *sacrificial* CP, Q_s is located at pixel y and the *beneficial* CP Q_b is located a distance d behind Q_s. The following constraint holds on y, d, and N:

$$y + d \leq N. \tag{3.5}$$

Thus, for a given distance to the *sacrificial* CP, the maximum row number that the *sacrificial* CP can come from is

$$y_{max} = N - d. \tag{3.6}$$

The number of traps per pixel in the IA and FS are respectively given as

$$N_i = N_L p_i, N_f = N_L p_f, \tag{3.7}$$

where N_L is the number of traps per micron along the transfer direction, p_i and p_f are the pixel length along the transfer direction in the IA and FS, respectively.

Then the number seen by the *sacrificial* CP is

$$N_s = NN_f + yN_i, \tag{3.8}$$

and the number seen by the *beneficial* CP is

$$N_b = NN_f + yN_i + dN_i. \tag{3.9}$$

For the simplicity, here is another assumption that the CPs are large enough so that the capture times are very short compared to the pixel to pixel transfer times so that empty traps have unity probability of capturing electrons from the passing packets. Then, the number of empty traps (N_e) seen by the *beneficial* CP is

$$\begin{aligned} N_e(y,d) &= N_i d + N_i y(1 - \exp(\frac{-dc_{if}}{\tau_e})) + N_f(N - y - d)(1 - \exp(\frac{-dc_{if}}{\tau_e})) \\ &\quad + N_f y(1 - \exp(\frac{-dc_{fs}}{\tau_e})) \\ &\quad + N_f \sum_{j=1}^{d}(1 - \exp(\frac{-dc_{if} + j(c_{if} - c_{fs})}{\tau_e})), \end{aligned} \tag{3.10}$$

where τ_e is the trap emission time constant, c_{if} and c_{fs} are the time it takes to transfer from one pixel to the next during the FS transfer and parallel transfer in the FS, respectively.

The first three terms in equation 3.10 describe traps encountered exclusively during the FS transfer. The first term corresponds to the traps which could not be touched by the *sacrificial* CP. The expression $(1 - \exp(\frac{-dc_{if}}{\tau_e}))$ is the availability of traps which increases with a time constant τ_e or equivalently with a position constant $\frac{\tau_e}{c_{if}}$. The fourth term corresponds to traps encountered by both packets exclusively during the slow parallel transfer in the FS. The availability of these traps have a position constant $\frac{\tau_e}{c_{fs}}$. For the XIS CCD, $c_{fs}/c_{if} = 277$. The fifth term is due to traps filled by the *sacrificial* CP during the FS transfer, but seen by the *beneficial*

CP during the slow parallel transfer in the FS. For these traps, the passing time between the *sacrificial* CP and *beneficial* CP is a function of position, hence each term in the summation corresponds to a different pixel. The summation term is given by

$$N_f \sum_{j=1}^{d}(1-\exp(\frac{-dc_{if}+j(c_{if}-c_{fs})}{\tau_e})) \\ = N_f d - \frac{\exp(c_{if}-dc_{if}-dc_{fs})\{\exp(dc_{fs}/\tau_e)-\exp(dc_{if}/\tau_e)\}}{\exp(c_{fs}/\tau_e)-\exp(dc_{if}/\tau_e)}. \quad (3.11)$$

Hence we get N_e as

$$\begin{aligned} N_e(y,d) &= N_i d + N_f N(1-\exp(\frac{-dc_{if}}{\tau_e})) - N_f\{d(1-\exp(\frac{-dc_{if}}{\tau_e})) \\ &\quad -d + \frac{\exp(c_{if}-dc_{if}-dc_{fs})\{\exp(dc_{fs}/\tau_e)-\exp(dc_{if}/\tau_e)\}}{\exp(c_{fs}/\tau_e)-\exp(dc_{if}/\tau_e)}\} \\ &\quad +y\{(N_i-N_f)(1-\exp(\frac{-dc_{if}}{\tau_e}))+N_f(1-\exp(\frac{-dc_{fs}}{\tau_e}))\}. \quad (3.12) \end{aligned}$$

Suppose that the flux of X-rays per row is given by the function $g(y)$, then we can calculate the average number of empty traps, $N_{avg}(d)$ seen by CPs a distance d away from the *sacrificial* CP. This would be the average loss of charge due to trapping and is given by

$$N_{avg}(d) = \sum_{y=0}^{y_{max}} f(y,d) N_e(y,d), \quad (3.13)$$

where

$$f(y,d) = \frac{g(y)}{\sum_{y=0}^{y_{max}} g(y)}. \quad (3.14)$$

In order to estimate the trap density for the XIS CCDs using the in-orbit data, the flux per row, $g(y)$, must be determined for a given observation by looking at the image. In general, the resulting $f(y,d)$ may be very complicated. In the case of uniform illumination,

$$f(y,d) = \frac{1}{y_{max}} = \frac{1}{N-d}. \quad (3.15)$$

Then the equation 3.13 becomes as

$$\begin{aligned} N_{avg}(d) &= \frac{1}{y_{max}} \sum_{y=0}^{y_{max}} N_e(y,d) \\ &= (N_i+N_f)d + N_f N(1-\exp(\frac{-dc_{if}}{\tau_e})) \end{aligned}$$

$$
\begin{aligned}
& -N_f\{d(1-\exp(\frac{-dc_{if}}{\tau_e})) \\
& +\frac{\exp(c_{if}-dc_{if}-dc_{fs})\{\exp(dc_{fs}/\tau_e)-\exp(dc_{if}/\tau_e)\}}{\exp(c_{fs}/\tau_e)-\exp(dc_{if}/\tau_e)}\} \\
& +\frac{(y_{max}+1)}{2}\{(N_i-N_f)(1-\exp(\frac{-dc_{if}}{\tau_e}))+N_f(1-\exp(\frac{-dc_{fs}}{\tau_e}))\} \\
= \quad & N_L\{(p_f+p_i)d+p_fN(1-\exp(\frac{-dc_{if}}{\tau_e})) \qquad (3.16) \\
& -p_f\{d(1-\exp(\frac{-dc_{if}}{\tau_e})) \\
& +\frac{\exp(c_{if}-dc_{if}-dc_{fs})\{\exp(dc_{fs}/\tau_e)-\exp(dc_{if}/\tau_e)\}}{\exp(c_{fs}/\tau_e)-\exp(dc_{if}/\tau_e)}\} \\
& +\frac{(y_{max}+1)}{2}\{(p_i-p_f)(1-\exp(\frac{-dc_{if}}{\tau_e}))+p_f(1-\exp(\frac{-dc_{fs}}{\tau_e}))\}\}
\end{aligned}
$$

In equation 3.16, N_L, p_i, and p_f are introduced to get rid of N_i and N_f. The only unknown parameters are the linear density of traps, N_L, and the detrapping time constant τ_e. In the case of the XIS CCDs, the following values hold: p_f is 18μm, p_i is 24μm, c_{if} is 24 μsec, and c_{fs} is 6.8 msec.

Although we cannot estimate N_L and τ_e precisely only with the ^{55}Fe data because of the poor statistics. Nevertheless in figure 3.13, we can see the tendency that the difference of the line center energy between the *sacrificial* and *beneficial* CPs decrease as the distance of the two CPs increase. This means that increasing distance corresponds to an increasing probability that the traps filled by the *sacrificial* CP have detrapped and that the *beneficial* CPs encounters the empty traps (equation 3.16).

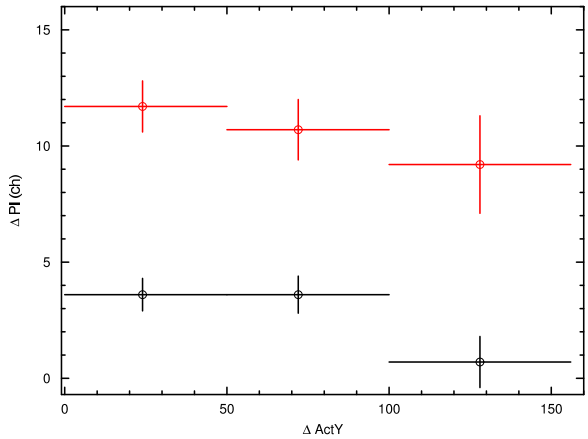

Figure 3.13: The line center of the *beneficial* CPs in figure 3.12 subtracted by that of the *sacrificial* CPs. The black and red data indicates the data of 2005 and 2006, respectively. The negative correlation means that increasing distance corresponds to an increasing probability that the traps filled by the *sacrificial* CP have detrapped.

Chapter 4

Ground Calibration of XIS

4.1 Goal for Calibration Accuracy

Figure 4.1 shows a spectrum of ^{55}Fe obtained with the XIS Flight Model (FM) sensor. We can see not only the main peaks of Mn Kα and Kβ, but also the escape peaks, fluorescent peak, tail, and constant component. The ratios between the intensities of these components are sensitive to the X-ray energy, gate structure, and thickness of the depletion layer. In order to interpret X-ray spectra obtained in orbit, we aim to construct a precise energy redistribution function (response function) for monochromatic X-rays.

The goals of our calibration are as follows:

1. The line center energy should be correctly measured with a systematic error of <0.1% of the incident X-ray energy.

2. The energy resolution should be determined within an accuracy of 1%.

3. The QE should be measured within an accuracy of 10%.

4. The spectral shape of monochromatic X-rays, including the Si fluorescent peak, escape peaks, tail, and constant component should be measured with errors of <3%.

4.2 Calibration System

The calibration was conducted with the fluorescent X-ray generation system at Kyoto University (Hamaguchi et al. 2000). The X-ray generation system involves continuous X-rays from an X-ray generator which shines an selected target within a chamber. The targets (Al, Cl, Ti, Fe, Zn, Se, and Polyethylene) are on a rotating stage. Secondary fluorescent X-rays are incident on the XIS in the other chamber. In the case that XIS is moved out of the beam line, the intensity and spectrum of the beam can be taken using a backward windowless solid-state detector (SSD).

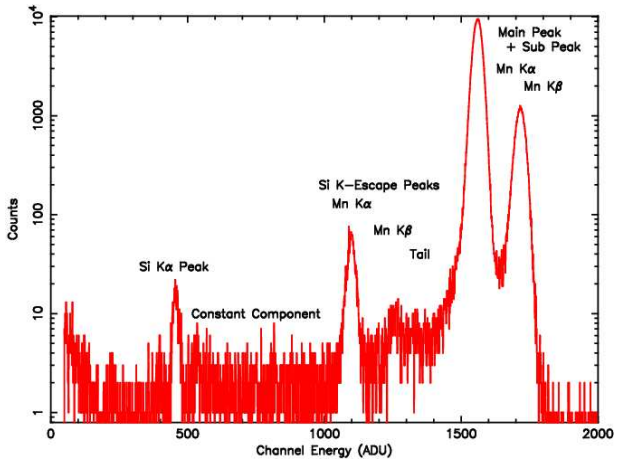

Figure 4.1: A spectrum of the XIS FI sensor of the ^{55}Fe source. There are several components in this spectrum such as the main peak, sub peak, constant component, escape peak, and Si Kα peak, all of which are labeled. The final purpose of calibration is to determine the flux of each component to within an error of 3%.

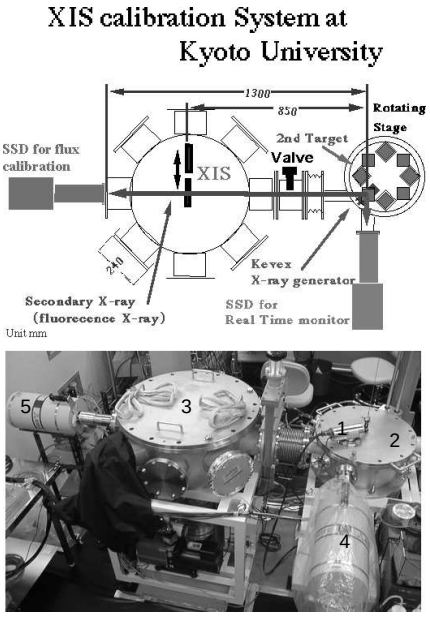

Figure 4.2: Schematic view and photograph of the X-ray generation system at Kyoto University. The primary X-rays from the Kevex X-ray generator irradiate the second targets and the secondary fluorescent X-rays irradiate the XIS sensor placed in the main chamber or the detector (SSD in this figure) behind the XIS.

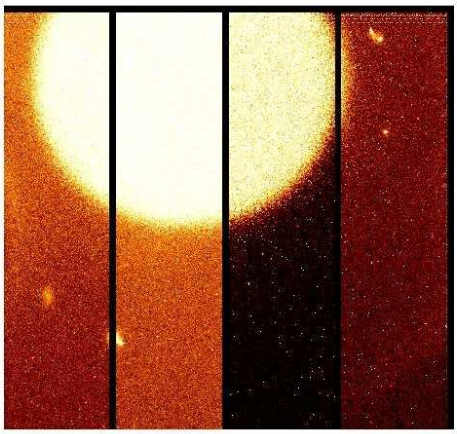

Figure 4.3: Frame image of the proton-damaged FI sensor used in the ground experiment. The gray scale is the pixel level, not the number of events. Gaps between segments are horizontal over-clock regions. Proton irradiation causes the circular region in segments A to C to have systematically different pixel levels due to the dark current.

We also conducted the experiments with the proton-damaged CCD chip at MIT for the CI issues. The CCD chip was damaged by protons utilizing the cyclotron at the Northeast Proton Therapy Center(NTPC) at Boston. The 160 MeV primary beam of protons was degraded with lexan blocks to a spectrum peaked at 40 MeV with an FWHM of about 4 MeV. The beam was irradiated onto the circular region shown in figure 4.3. The total fluence was 2.0×10^9 cm^{-2}, which is approximately the same as that the XIS receives during several years in orbit. For the ground test, we used the secondary fluorescent X-rays and a ^{55}Fe radioisotope at MIT. Figure 4.4 compares PHA spectra from ^{55}Fe source extracted from proton-damaged and undamaged region in segment B, respectively.

During the both calibrations, the sensors were in environments with pressures of $\sim 10^{-6}$ Torr and CCD temperatures of –90 °C. In the following, we describe the results of our calibration.

4.3 Readout Noise and Split Threshold

First, we investigated the readout noise of each sensor segment. All sensors showed noise levels of ∼2 - 3 ADU (RMS). From these values, we determined the split threshold for event extraction for the FI chips. In order to measure the pulse height correctly, it is essential to determine the value of the split threshold considering the readout noise. Then, ∼5 σ of the readout noise, that is, ∼ 15 ADU, is preferable as the split threshold. We then set the threshold to be 20 ADU considering the margin.

In the case of the BI chip, we found that the energy-dependent threshold level should be introduced in order to optimize the QE and energy resolution (Yamaguchi et al. 2006a). Contrary to the case of the FI chip, the electron clouds produced by

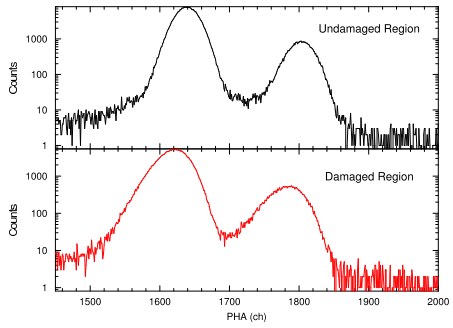

Figure 4.4: Spectra of ^{55}Fe extracted from the proton undamaged region (upper panel) and damaged region (bottom panel). The line center and width are both degraded in the bottom panel compared with that of upper panel.

the low energy X-ray photons drift in the depletion layer for a longer distance than those produced by the high energy X-ray photons. Then, the FWHMs of the spatial distribution of the electron clouds by the low energy X-rays are larger than those by the high energy X-rays, although the amount of the split charges is smaller than those by the high energy X-rays. As a result, if one set the low split threshold considering the large FWHM of low energy events, the significant part of the high energy events is regarded as grade 7 as long as one adopt the energy-independent split threshold. On the other hand, one fails to sum up the pulse height in the split pixel for the low energy events with the high split threshold optimized for the high energy events. In fact the grade distribution with the split threshold of 7 ch is as shown in figure 4.5.

Then, we made the spectra with various split threshold levels for each fluorescent line prior to calibrations of other issues and investigated the FWHM of the spectrum peak and the number of events as shown in figure 4.6. While the FWHM improves as the split threshold decrease, the event detection efficiency (*i.e.* QE) degrades. We determined the optimum threshold level from these plots so that the increment of the QE becomes less than 3% when one increments the split threshold level by one channel.

Then we determined the optimized split threshold levels as a function of energy as

$$\text{splitth.} = 2.21 \times \log 10E_0 + 10.36, \tag{4.1}$$

as shown in figure 4.7, where E_0 is the energy of X-rays. This improves the QE 13, 36, and 40% at the energy of 2.6, 6.4, 8.6 keV compared to the values with constant split threshold of 7 ch, respectively.

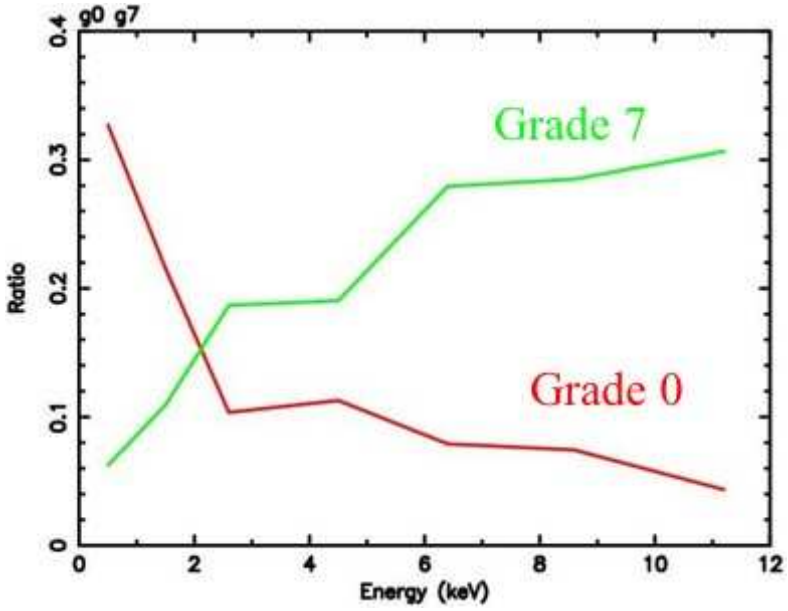

Figure 4.5: Percentage of the Grade 0 and 7 events as a function of the energy of incident X-rays. The significant percentage of the X-ray events are regarded as grade 7 in the high energy band and hence virtually diminish the QE of the BI chip.

4.4 Gain and Energy resolution

Adopting the split threshold determined in the above section, we extracted the X-ray events from each data set and made a spectrum. For the line spectrum of each fluorescent X-ray, we fitted each peak (Kα and Kβ) with two gaussians (main and sub peak component) considering the response distribution function (figure 4.1). Figure 4.8 shows the gain of XIS FI1 segment A. The grade of the extracted events are 0, 2, 3, 4, and 6. The energy-pulse height relation is quite linear in the energy band of 1 - 12 keV. The error of the gain is less than 0.1% for all segments of all sensors. The difference in gain among the segments is less than 10%.

Figure 4.9 shows the spectral resolution of XIS FI1 segment A. The grades of the extracted events are the same as in the previous section. We fitted the data with the equation 3.1. The free parameters are N and $\frac{F}{W}$. The best fit value of N and $\frac{F}{W}$ are 2.6$\pm$1.2 electrons and 4.34$\pm$0.06$\times 10^{-2}$, which corresponds to the Fano factor of $\sim$ 0.16$\pm$0.02 when we assume that $W = 3.65$. Considering the gain obtained in the previous section, the values for the noise and Fano factor are consistent with the results of Section 4.3 and with the literature (Knoll 1989). We achieve an energy resolution of $\sim$ 130eV@5.9 keV for all sensors. The error in the resolution is less than 1% for all segments of all sensors.

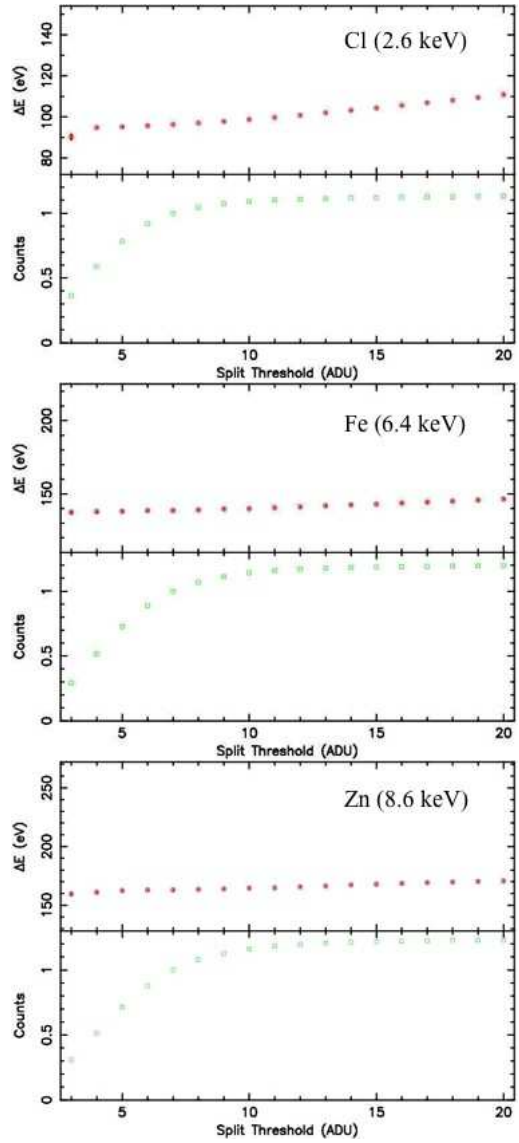

Figure 4.6: Energy resolution (FWHM) and detected number of events as a function of the split threshold. The latter is normalized to that in the case with a split threshold of 7 ch.

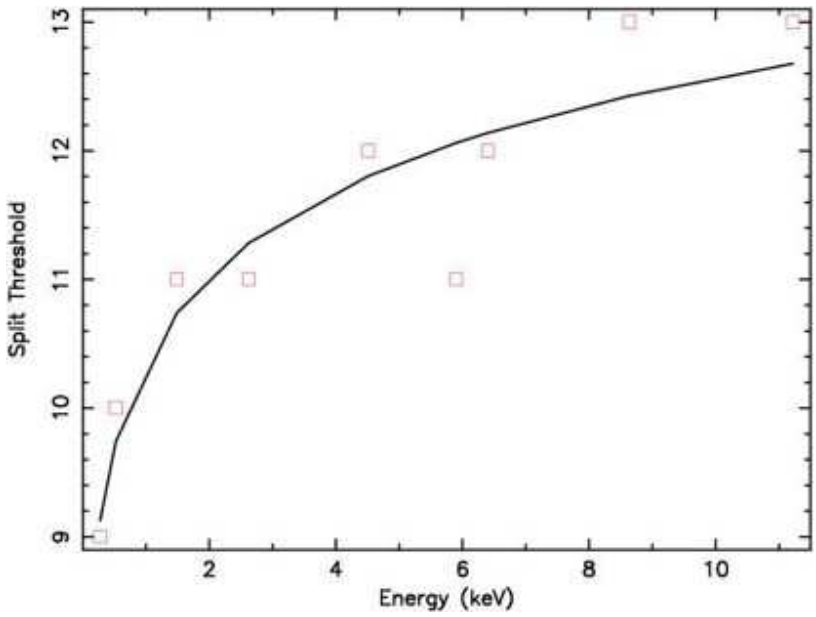

Figure 4.7: The optimized split threshold levels as a function of the energy of the X-rays. A solid line is the best-fit result of the data (equation 4.1).

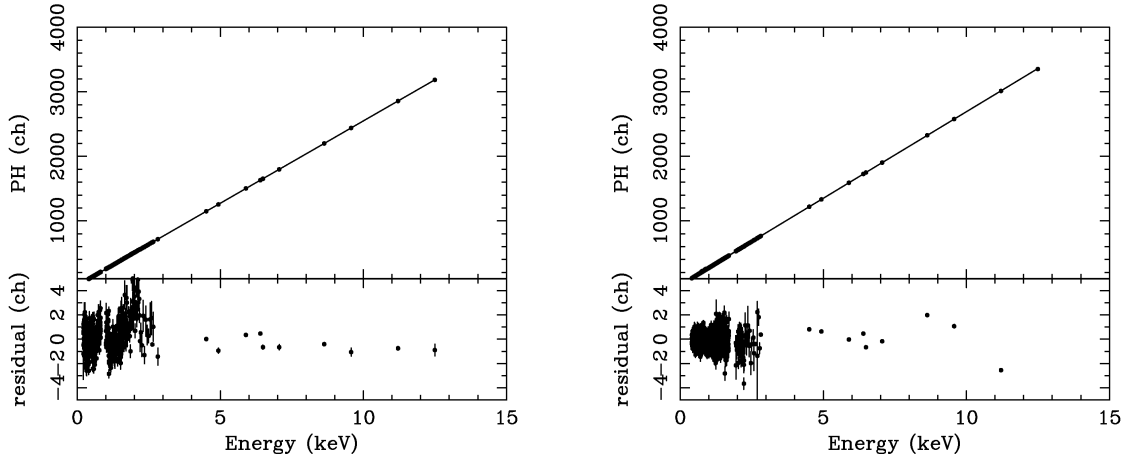

Figure 4.8: The XIS energy scale linearity of XIS1 segment C (left panel) and XIS2 segment C (right panel). We obtained a gain of 265.1 ch/keV.

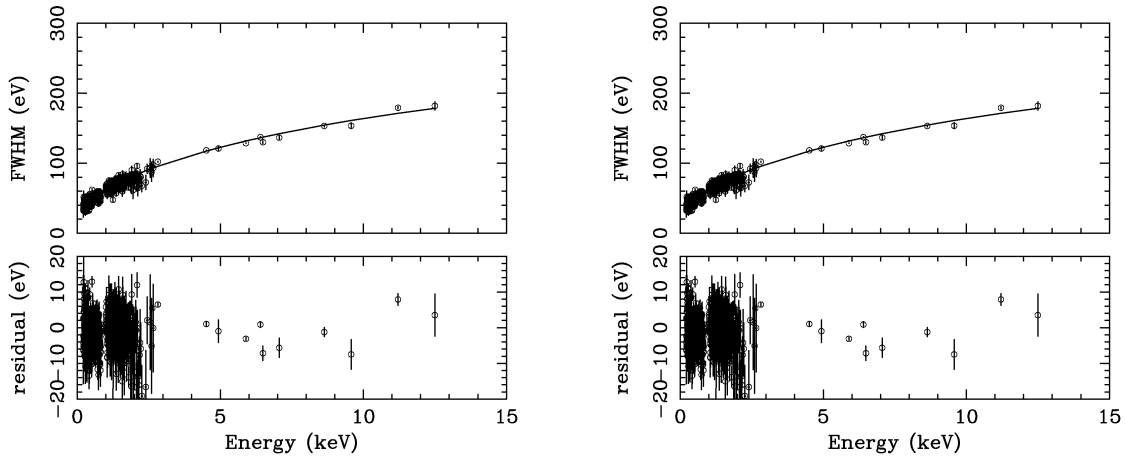

Figure 4.9: The spectral resolution as a function of energy for the XIS1 segment C (left panel) and XIS2 segment C (right panel). We obtained a resolution of 131 eV in FWHM at 5.89 keV.

4.5 Quantum Efficiency

Here we converge on the QE measurement in the high energy band executed at Kyoto University. Figure 4.10 shows the QE of XIS FI1 segment A. The solid curves represent the simulated function with a simple layer model described in the following.

The probability that the X-ray with energy of E_0 is absorbed within the depletion layer is

$$P_{\rm absorp} = \exp(-\mu_{\rm Si} d_m n_m) \exp(-\mu_{\rm SiO_2} d_o m_o)(1 - \exp(-\mu_{\rm Si} d_d n_d)), \qquad (4.2)$$

where d_m, d_o, d_d, n_m,n_o, and n_d are thicknesses and density of metal, oxide, depletion layers, respectively. $\mu_{\rm Si}$ and $\mu_{\rm O}$ are the mass absorption coefficients of silicon and oxygen, respectively. We assume that

$$\mu_{\rm Si} = 10^{4.3-2.78\log_{10}(E_0)} (E_0 \leq 1.839{\rm keV}) \qquad (4.3)$$

$$10^{3.19-2.71\log_{10}(E_0)+0.0755\log_{10}(E_0)^{2.0}+0.873\log_{10}(E_0)^3} (E_0 > 1.839{\rm keV}), \qquad (4.4)$$

$$\mu_{\rm O} = 10^{3.65-2.74\log_{10}(E_0)} (E_0 > 0.543{\rm keV}). \qquad (4.5)$$

The central curve assumes nominal values for the thickness of the electrode layer, insulation layer, and depletion layer, that is, 0.33 μm, 0.27 μm, and 74 μm respectively. The uppermost and lowermost curves represent the cases when the thickness of each layer deviates from the nominal value by $\sim \pm$ 10%. The QE value in the soft energy band is subject to the thicknesses of the ineffective layers, that is, the electrode and insulation layer. In the high energy band, the QE depends on the thickness of the depletion layer. As shown in figure 4.10, the QE of XIS at $\sim$4.5 keV

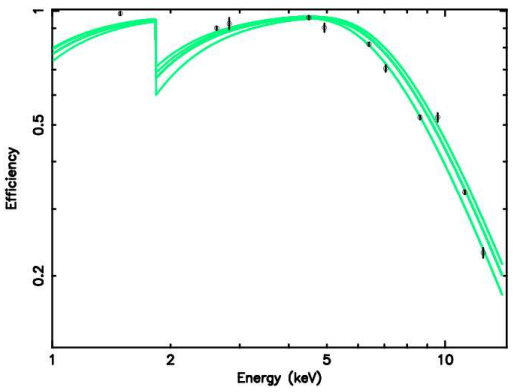

Figure 4.10: The QE as a function of energy for XIS FI segment A. The solid curves show simulated QE, where the input parameters are the thickness of the electrode layer, insulation layer, and depletion layer. We determined the nominal value to be 0.33 (0.25–0.45) μm, 0.27 (0.20–0.35) μm, and 74 (60–80) μm, respectively. Having confirmed that the QE at 4.5 keV is almost constant (96$\pm$0.7%), we normalized the QE to 96%@4.5 keV.

(Ti Kα line) is 96$\pm$0.7% as far as the thicknesses of each layer deviates 10% from its nominal values. Hence the QE value at 4.5 keV can be a good reference value considering the requested calibration accuracy. Hereafter we assume the QE at 4.5 keV is 96%.

After the data acquisition with the XIS, we shift the XIS and collect data with a windowless SSD, which is located behind XIS. Since the QE of the SSD is $\sim$ 100% at the energy band of $>$ 1 keV, we measured the normalized QE of XIS as a function of the intrinsic energy, and $\sim$52%@8.6keV is achieved. The error in the normalized QE is less than 3% for all segments of all sensors.

4.6 Performance of Charge Injection Capability

4.6.1 Stability of the Amount of Injected Charges

If the amount of injected charge (Q) can be more accurately controlled than that of charge dispersion of X-ray events, then CI capability offers obvious advantages over conventional CTI measurements using X-ray calibration sources. We hence checked the stability of Q' with the non-damaged chip, for which Q' most precisely reflect Q because of the small number of CTs. Throughout this experiment, a constant offset voltage was applied at the input gate.

Figure 4.11 shows the spectra of fluorescent X-rays (Ti Kα) and the CI *test* events, which have approximately the same equivalent energy as X-rays. The data is collected with a non-damaged chip and a duration of 350 frames (2.8 ksec). Events are extracted from a specified column for all data sets. The FWHM of the CI data (80$\pm$5 eV) is significantly better than that of the X-ray spectrum (130$\pm$10 eV). The former is due to the stability of the amount of injected charges and the noise on

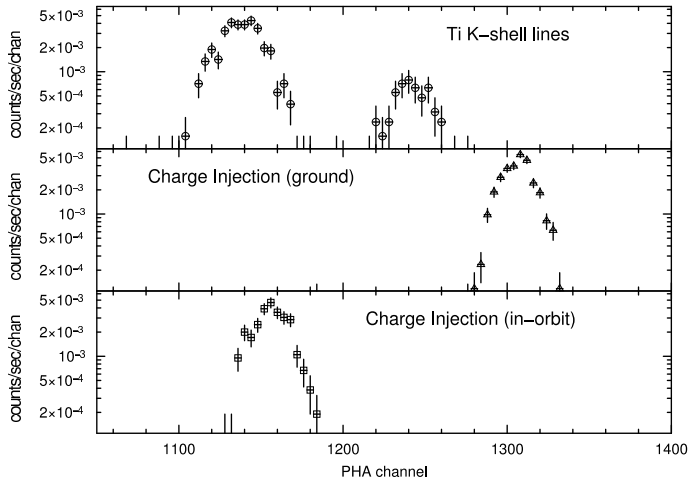

Figure 4.11: (Upper panel:) Spectra of Ti Kα fluorescent X-rays from an exposure of 350 frames taken in the ground experiments. (Middle panel:) Spectra of CI events collected on ground from an exposure of 400 frames. (Bottom panel:) Same as middle panel but collected in orbit from an exposure of 800 frames. The PHA level is slightly different from that in middle panel because the offset voltage is varied from that adopted in ground experiments. For all panels, the events are extracted from an arbitrary column (X=2). Horizontal axis is the dark-level-subtracted PHA.

the charges (Prigozhin et al. 2004) while the latter is primarily due to the Poisson statistics and the Fano factor. Thus, we verify that Q in a specified column is sufficiently stable to estimate δQ on a short timescale of several ksec.

Next, we investigate whether the ratio of $Q'_{\rm test}$ to $Q'_{\rm ref}$ is proportional to the CTI, which can be reflected by ^{55}Fe events, for each column with the damaged chip at MIT and non-damaged chip at Kyoto Univ. Due to the stability of Q over several hundreds of frames, the histograms of the PHA of $Q'_{\rm ref}$ and $Q'_{\rm test}$ are successfully fitted with a single Gaussian for each column. For the ^{55}Fe events, we extracted the events from upper and lower edges of the imaging area ($Q'_{\rm upper}$ and $Q'_{\rm lower}$). The extracting regions were 100 rows in order to satisfy the statistics requirement for the spectral fitting. Figure 4.12 shows the correlations between $Q'_{\rm test}/Q'_{\rm reference}$ of the CI events and $Q'_{\rm upper}/Q'_{\rm lower}$ of the ^{55}Fe events. For the non-damaged chip (the left panel), because δQ during the parallel transfer is 0 or 1 electron for ^{55}Fe events, the correlation can be hardly seen. In the case of the damaged chip, the CTI is significant and the most of the charge loss occur in the circular region as shown in figure 4.3. Then we can see a clear positive correlation between the ^{55}Fe and CI events for damaged chip (especially in segment A, B, and C). The best-fit slope is $\sim$1.05 and the correlation coefficient is 0.94 (d.o.f.=976). Hence, the ratio of the test and reference charges properly represents the CTI of each column.

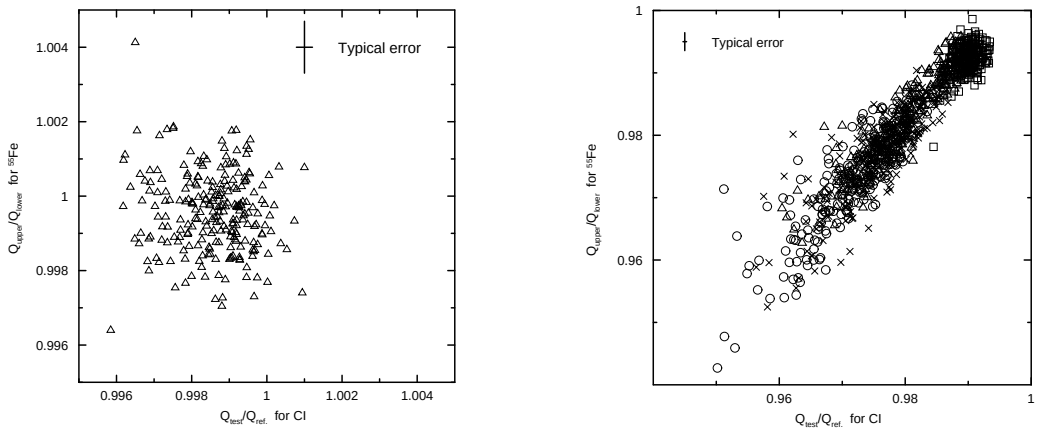

Figure 4.12: Ratio of $Q'_{\rm test}$ and $Q'_{\rm ref}$ for the CI events (horizontal axis) and that of $Q'_{\rm upper}$ and $Q'_{\rm lower}$ for the ^{55}Fe events (vertical axis). Open triangles, circles, crosses, and squares represent the columns in segment A, B, C, and D, respectively. Left:Plot for non-damaged chip. Note that plots for segments B, C, and D have the same distribution as segment A. Hence, segments B, C, and D are ignored from the figure for simplicity. Right:Plot for a proton-damaged chip.

4.7 Energy Redistribution Function

The branching ratio for each component such as in figure 4.1 is estimated. We then finally made the response function for FI and BI chips. determined with the ground experiments. Figure 4.13 shows the spectrum of ^{55}Fe collected with FI and BI chip. Although the response function reproduce the spectrum well over the entire energy band, some residual is seen between the Kα and Kβ line. This indicates the additional component in the spectra. The Radiative Auger Emission (RAE;Åberg 1971; Richard et al. 1975; Jamison et al. 1976) is the appropriate candidate to explain this residual as shown in figure 4.14.

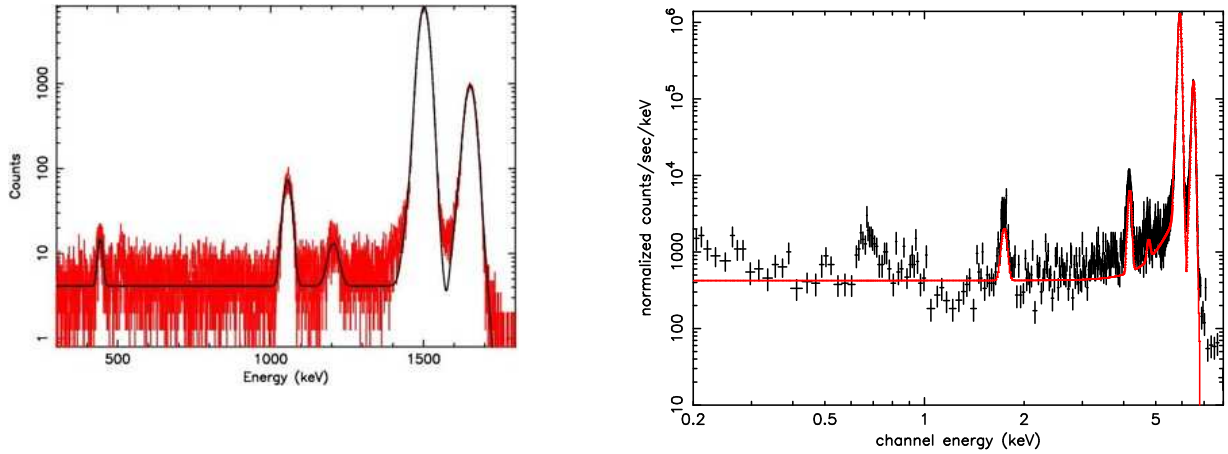

Figure 4.13: The spectra of ^{55}Fe collected the response function we obtained with ground experiments. The fitted model is the response function we determined with the ground experiments. Left and right panel show the spectra of the BI and FI chip, respectively.

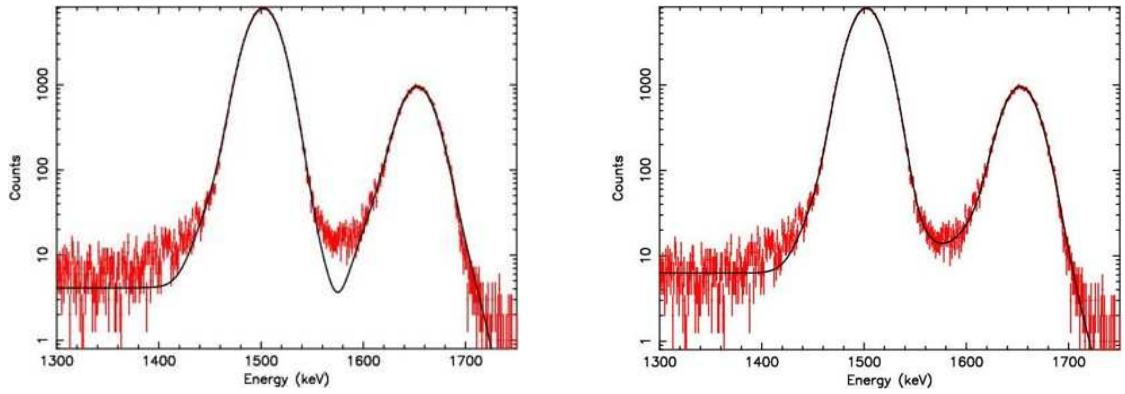

Figure 4.14: Fit results of ^{55}Fe spectrum with the response function around the Kα and Kβ line. (Left panel:) The XIS1 spectrum is fitted with a model of two monochromatic lines with energies of 5.9 and 6.5 keV. (Right panel:)The XIS1 spectrum is fitted with a model of two monochromatic line and a broad line emission, which approximate the RAE component.

Chapter 5

Onboard Calibration of XIS

5.1 Performance Degradation in Orbit

As described in 3.2.5, the radiation damage onto the CCD has been integrated by the protons in SAA. Figure 5.1 and 5.2 show the degradation of the line center energy and line width of ^{55}Fe Kα line without any CTI correction as a function of time from the first light to the June 2006. Here the line width means the value when one fits the main peak with single gaussian using the response function made from the ground experiments (see 4.7). The both parameters gradually decrease at a rate of $\sim$ 120 eV per year and $\sim$ 50 eV per year, respectively. The goal of the in-orbit calibration for the gain is the same as that in the ground calibration.

5.2 CTI correction with CI Capability

Most of the major X-ray missions are provided with one or more calibration sources to measure the CTI and gain. However, the limited flux of calibration X-rays impedes a detailed and frequent investigation of the spatial structure of the CTI over the chip, which makes it difficult to perform a column-to-column charge compensation. Hence we have been periodically executing CI to determine the CTI parameters.

5.2.1 CTI Measurement with Checker Flag CI

In order to apply the CI function to the observational data, the on-orbit CI experiment was conducted during the calibration observations of the SNR 1E0102–72.3 in the Large Magellanic Cloud. Table 5.1 summarizes the experimental logs. All the data was acquired with the normal clock and with the 3×3 or 5×5 mode (Koyama et al. 2006a). Table 5.1 also lists the equivalent energy of the CPs. Figure 3.9 shows a frame image taken during our experiments. The positions of the CP trains are periodically shifted by one column to allow the proper event detection algorithm. The *sacrificial* CPs are not read because of the same reason. The value δQ after the transfer can be measured by the difference of the mean PHA of the *test* events to

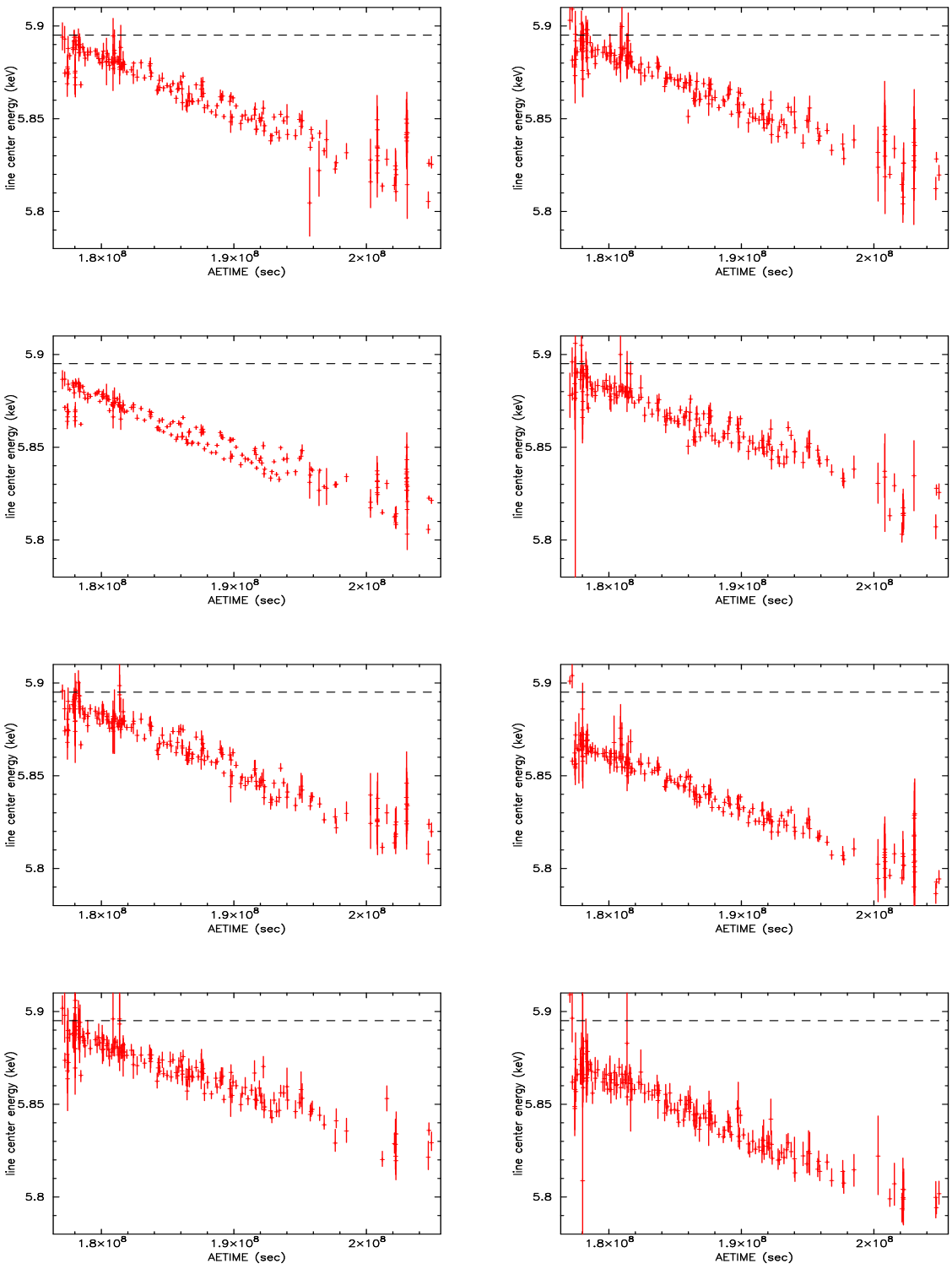

Figure 5.1: The line center energy of the each calibration source as a function of time without any CTI correction. The dashed lines indicate the intrinsic value of the Kα line center, 5.89507 keV (Bearden 1967; Krause & Oliver 1979). Each plot corresponds to a continuous exposure toward a celestial object. The horizontal axis AETIME is the time in seconds since 0000 UT Jan 1st, 2000.

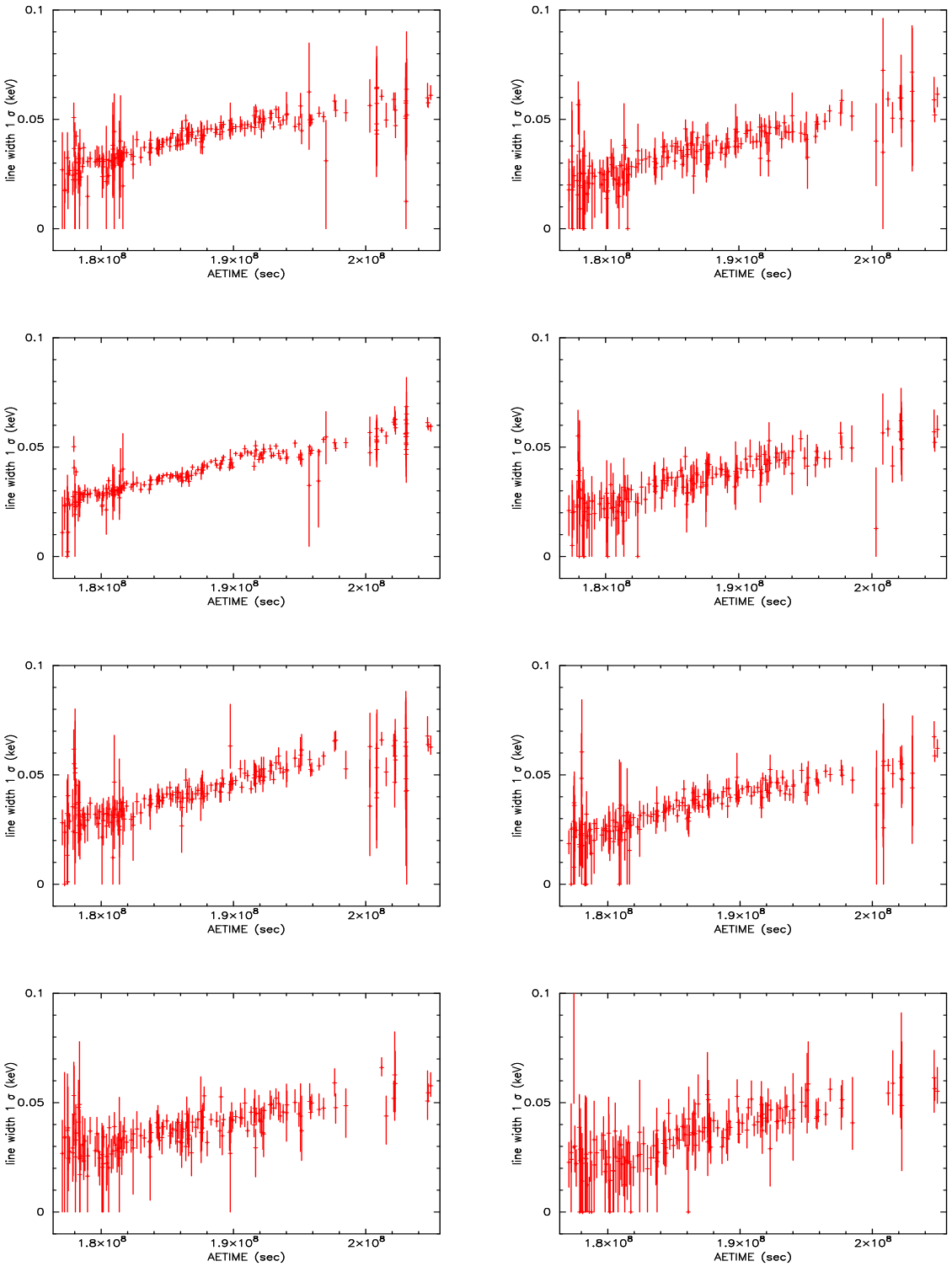

Figure 5.2: The line widths of the each calibration source as a function of time without any CTI correction when one fits the Kα main peak with single gaussian using the response function made from the ground experiments. Each plot corresponds to a continuous exposure toward any celestial object. The horizontal axis is the same as figure 5.1.

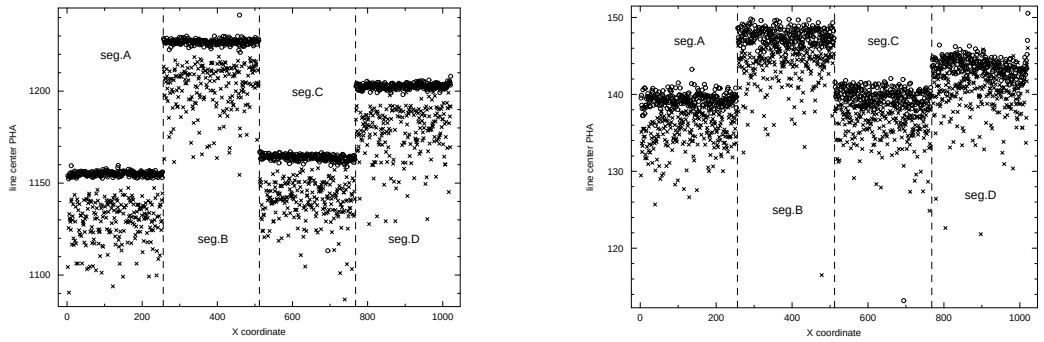

Figure 5.3: PHA distribution of the *test* and *reference* events as a function of the X coordinate of XIS3 for two different amounts of injected charges. The equivalent energies of the CPs are shown in table 5.1. Note that because each segment has its own readout transistor and analog-to-digital converter, the gain and zero level vary from segment to segment, and hence, the PHA level varies. Anomalous columns, including a hot or flickering pixel are eliminated.

that of the *reference* events. By selecting different Qs, we can also investigate the relation between Q and δQ.

Table 5.1: The log of the CI experiment on orbit.

	XIS0 & XIS2	XIS1 & XIS3
Date	2006/7/17	2006/6/26-27
Time	06:06:50-21:39:46	02:47:07-02:37:55
The equivalent energy (keV)	0.6/4.2/8.0 for XIS0	0.3/7.3 for XIS1
of the injected CPs	0.6/3.9/7.8 for XIS2	0.5/4.6 for XIS3
Effective Exposure (ksec)	6.0	5.2

5.2.2 Compensating for the Charge Loss

Given the results of the ground verification experiments (section 4.6.1), our next aim is to apply the CI techniques to the onboard data.

Figure 5.3 shows the PHA distribution for Q'_{ref} (open circle) and Q'_{test} (cross) as a function of X-coordinate (column). The $\delta Q_{\rm COL}$ is clearly observed in orbit for the first time. In order to estimate the δQ dependence on Q, we selected two or three different Q values for the in-orbit CI experiment (table 5.1). Assuming the single power law function of $\delta Q \propto Q^{\alpha}$ (e.g. Grant et al. 2004), we derive α for each column. The results are given in figure 5.4. The weighted mean values of α range 0.62 - 1.00 among sensors. These values are roughly consistent with another ground experiment (Prigozhin et al. 2004).

The CI data provides only the information on the δQ at the edge of the IA and hence we need to know the Y coordinate dependence of δQ from the data of celestial

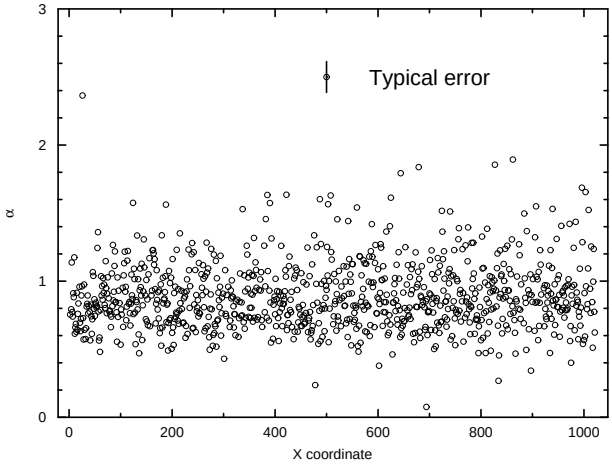

Figure 5.4: Distribution of the index in the relation between δQ and Q (XIS3). Some anomalous columns are eliminated.

objects that extend over the field of view of the XIS. Figure 5.5 shows the center energy of the 6.4 keV line as a function of the Y coordinate for the diffuse X-rays from the Sgr C region (Obs. Sequence = 500018010, Obs. Date = 2006-02-20). The line center at the lower edge of the image (Y=0) deviates from 6.40 keV due to the CTI during the quick transfer of all the data in the IA to the frame-store (FS) region (hereafter we call this FS-transfer). However, the origin of the deviations at the other image regions is complicated because the charges suffer from three kinds of the CTI: the CTI in the IA due to the FS-transfer, that in the FS region due to the both of the FS-transfer and subsequent slow vertical transfer. δQ during the horizontal transfer is ignored in this work. The CTI depends on the number density of CTs and the transfer speed (Hardy et al. 1998). The shielding depth and pixel size are different in the IA and FS. The CTIs therefore may be largely different between in these areas. However, we cannot estimate each CTI component separately from the total CTI seen in figure 5.5. Due to this limitation, we phenomenologically compensate charges utilizing figure 5.5 and CI data as followings. At first we estimate the column-averaged δQ as a function of Y coordinate at the energy of CI events from the Q dependance of δQ and figure 5.5. Then, we determine the ratio of the column-averaged δQ to the $\delta Q_{\rm COL}$ at Y=0. Finally we estimate $\delta Q_{\rm COL}$ as a function of Y coordinate so that the ratio of the column-averaged δQ to the $\delta Q_{\rm COL}$ at Y=0 is maintained at any other Y coordinate. Hence we can compensate charges correctly in the entire region of the IA.

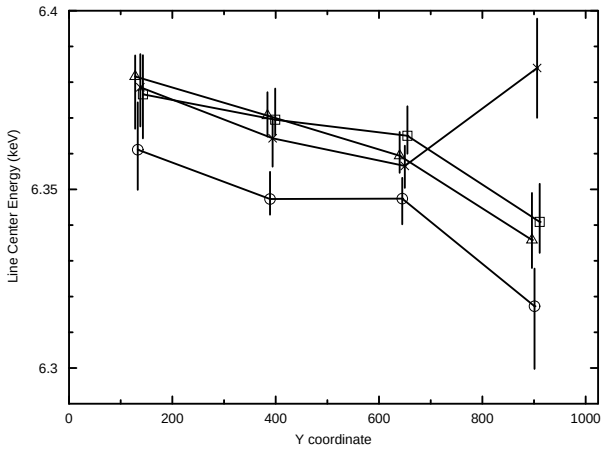

Figure 5.5: The Y coordinate dependence of the center energy of 6.4 keV line emission from the Sgr C region. Photons are each extracted from 1024 × 256 region. Open triangles, circles, crosses, and squares represent the plots of XIS 0, 1, 3, and 3, respectively.

5.2.3 Energy Resolution Improvement

Using the $\delta Q_{\rm COL}$ determined with the CI experiment, we make the new spectra for the calibration sources in the observations given in table 5.1. Figure 5.6 shows the calibration source spectra after the $\rm CTI_{CI}$ (upper) and $\rm CTI_{CAL}$ (lower) correction. The tail component seen after the $\rm CTI_{CI}$ correction is significantly reduced compared to that after the $\rm CTI_{CAL}$ correction. This strongly indicates that the origin of the tail component is the dispersion of the $\rm CTI_{COL}$ among columns. Figure 5.7 shows the FWHM of the calibration source spectra after the $\rm CTI_{CI}$ and $\rm CTI_{CAL}$ correction. On average, the FWHM is significantly improved from 193 eV to 173 eV. These are the first in-orbit results for the CI function.

Our final purpose is to demonstrate that δQ parameters are effective for celestial objects. We apply the δQ parameters to the Tycho's SNR data (Obs. Sequence = 500024010, Obs. Date = 2006-06-27). Figure 5.8 shows the spectra around the He-like Si Kα emission line in the west part of Tycho's SNR for the XIS3 after the $\rm CTI_{CI}$ correction and $\rm CTI_{CAL}$ correction. We see the same benefit as shown in figure 5.6. Note that the latter is multiplied by 0.8 to avoid confusion. Radiation damage continuously increases while in orbit, and hence, the benefit of the CI technique will become more apparent over time.

Because the $\rm CTI_{CI}$ correction parameters are time dependent, $\delta Q_{\rm COL}$ must be periodically measured. We make two sets of $\rm CTI_{CI}$ using $\delta Q_{\rm COL}$ derived from the CI experiment in May and July 2006, and apply to the calibration source data taken in May 2006 for the XIS0 and XIS2. The results are shown in figure 5.9. The CTI in July is normalized to that in May, while the relative variation in $\rm CTI_{CI}$ is preserved. If the observation time of the CI and ^{55}Fe data differs by two months, the FWHM is significantly degraded only for the brightest calibration source. This confirms that, in practical sense, the interval of two months between each CTI measurement

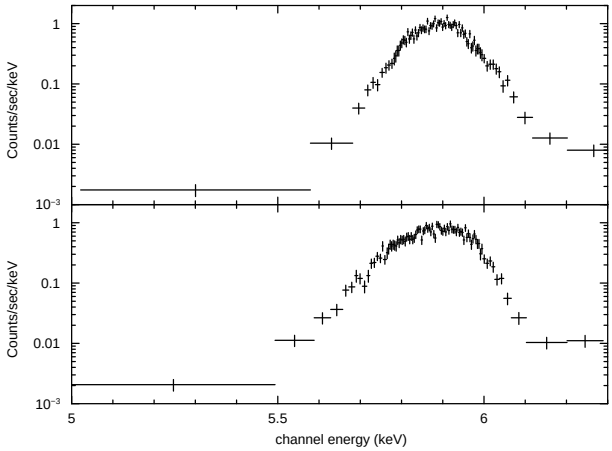

Figure 5.6: Energy spectra of the calibration source in the segment D of XIS2, after charge compensation with CI capability (upper panel) and with the calibration source itself (lower panel). Data is simultaneously obtained with the CI experiment.

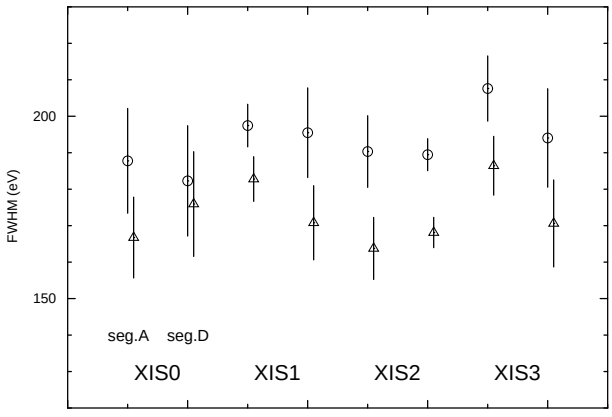

Figure 5.7: FWHM of the calibration source spectra simultaneously obtained with the CI experiments. Open triangles and circles represent the data after the charge compensation with the CI technique and with calibration source itself, respectively.

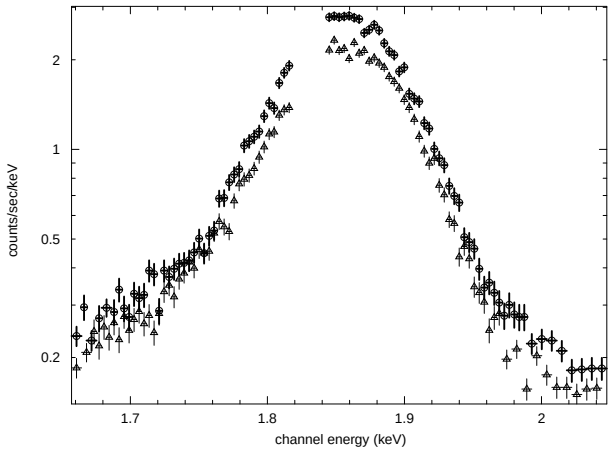

Figure 5.8: Spectra around the He-like Si Kα emission line of the west part of Tycho's SNR (XIS3). Data represented by open circles is charge-compensated using a calibration source, while the other (open triangles) is compensated using the CI technique. Note that the former is multiplied by 0.8 to avoid a complex expression, and the data around the Si K-edge (1.839 keV) is ignored due to an incomplete calibration.

is sufficient because there are few celestial objects which has emission line brighter than this calibration source.

Although the CI technique significantly improves the energy resolution of the calibration source spectra, the FWHMs are still larger than those before the launch (130 eV) as shown in figure 5.7. Because the charge trapping is a probability process, the number of trapped electrons (δQ) may also have a probability deviation, which would increase the line width after the transfer. Hence the CTI correction with CI technique cannot completely restore the line broadening. We confirm this effect in figure 5.10, which shows the FWHM of the CI *reference* events and those of the *test* events before and after the charge compensation for the XIS3 in-orbit data. In addition, the *test* events measured on ground (before the radiation damage) are shown. The smaller FWHMs in all segments of the *reference* events are due to the fact that the *reference* events may not loss charges because the CTs are already filled by the *sacrificial* events. In fact, the FWHMs of the *reference* events are consistent with those of the *test* events collected on ground although segment D show anomalous trend.

Another characteristic of the figure 5.10 is that the FWHMs increase along with X coordinate for the *reference* events and *test* events collected on ground. This is due to the CTI in the CI register. This influences the accuracy of the mean PHA of the *reference* events and hence the accuracy of δQ. However, the CTI in the CI register is rather lower than that in the IA and FS because the CPs are injected with an interval of 3 pixels and hence they can work as *sacrificial* charges (Gendreau 1995). In fact, as shown in figure 5.7, there is not significant difference between segment A and D for the improvement of the FWHM of the calibration source spectra.

These results lead us to use the CI capability to fill the traps in the transfer

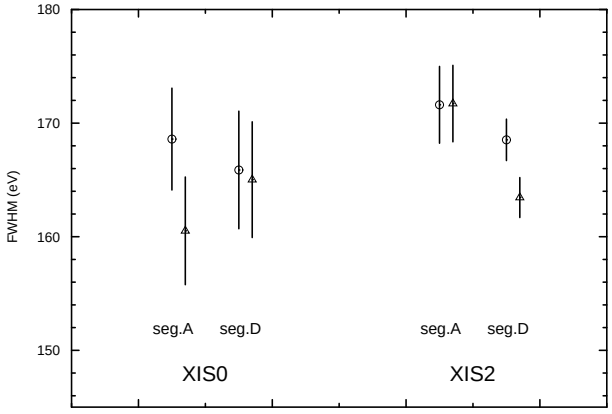

Figure 5.9: FWHM of the calibration source spectra simultaneously obtained with the CI experiment in May 2006. The δQ parameters derived from the CI data obtained in May (open triangles) and July 2006 (open circles) are also applied.

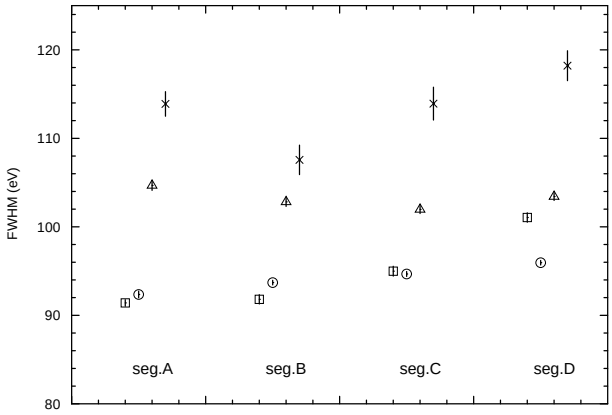

Figure 5.10: FWHM of the CI *test* events spectra before (cross) and after (open triangle) charge compensation, and that of the *reference* events (open circle) for each segment of XIS3. The *test* events collected on ground are also shown (open square). Even after the compensating, the FWHM of the *test* events spectra are larger than those of the *reference* events due to the probability process of the charge trap.

channel by periodically injection of Q. A ground experiment shows that charges injected into every 54^{th} row improve the energy resolution (Bautz et al. 2004). We are trying to utilize this CI technique for the onboard observations. The results will be presented in a separate paper.

5.3 Gain and Charge Transfer Efficiency

After the CTI correction, we determined the gain parameters as a function of time for each segment. With these CTI and gain parameters, the systematic error of Kα line center energy of ^{55}Fe became $\leq 2\% \approx 12eV$ as shown in figure 5.11. The line width is also improved after the CTI correction (figure 5.12).

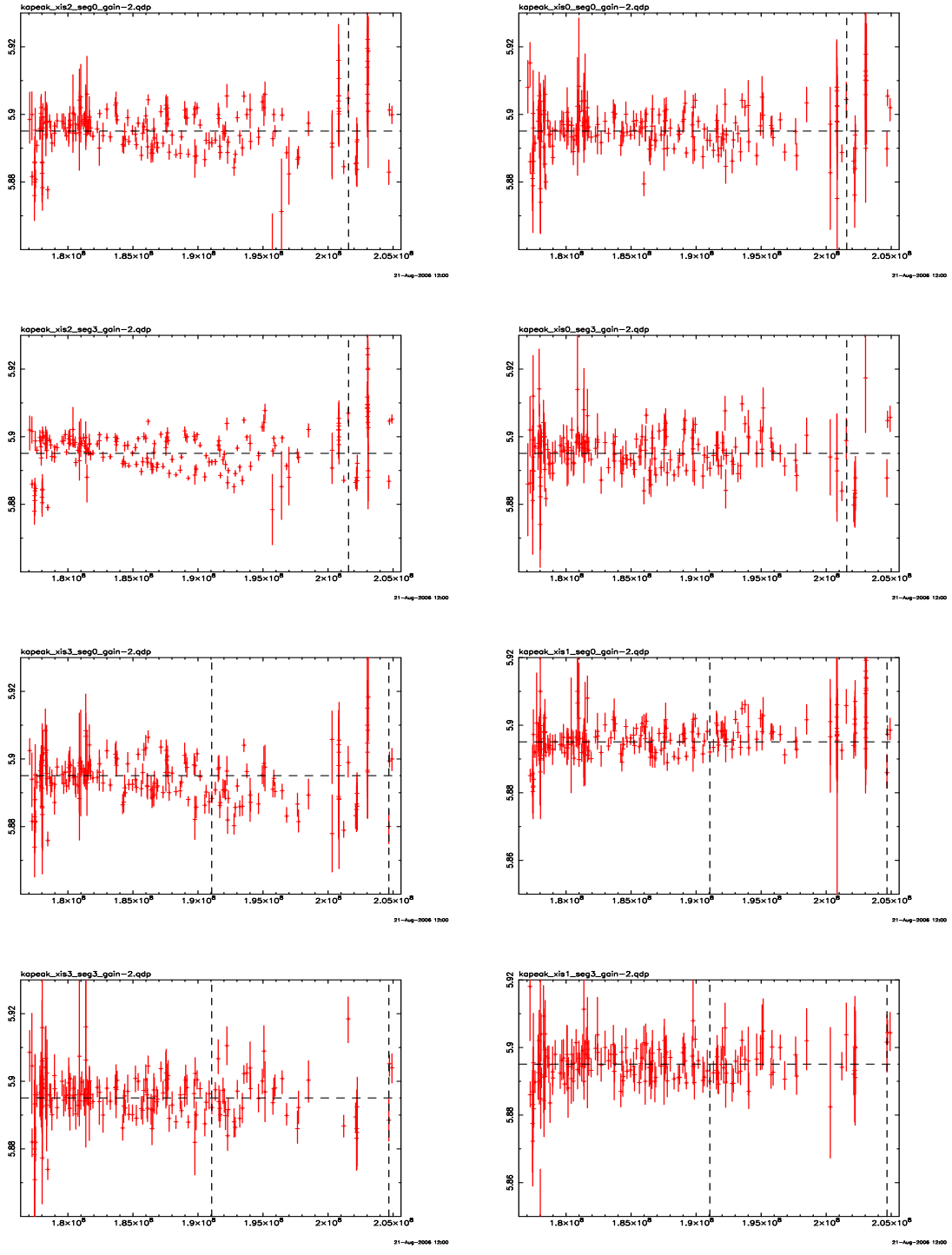

Figure 5.11: The same as figure 5.1, but after the $\mathrm{CTI_{CI}}$ correction.

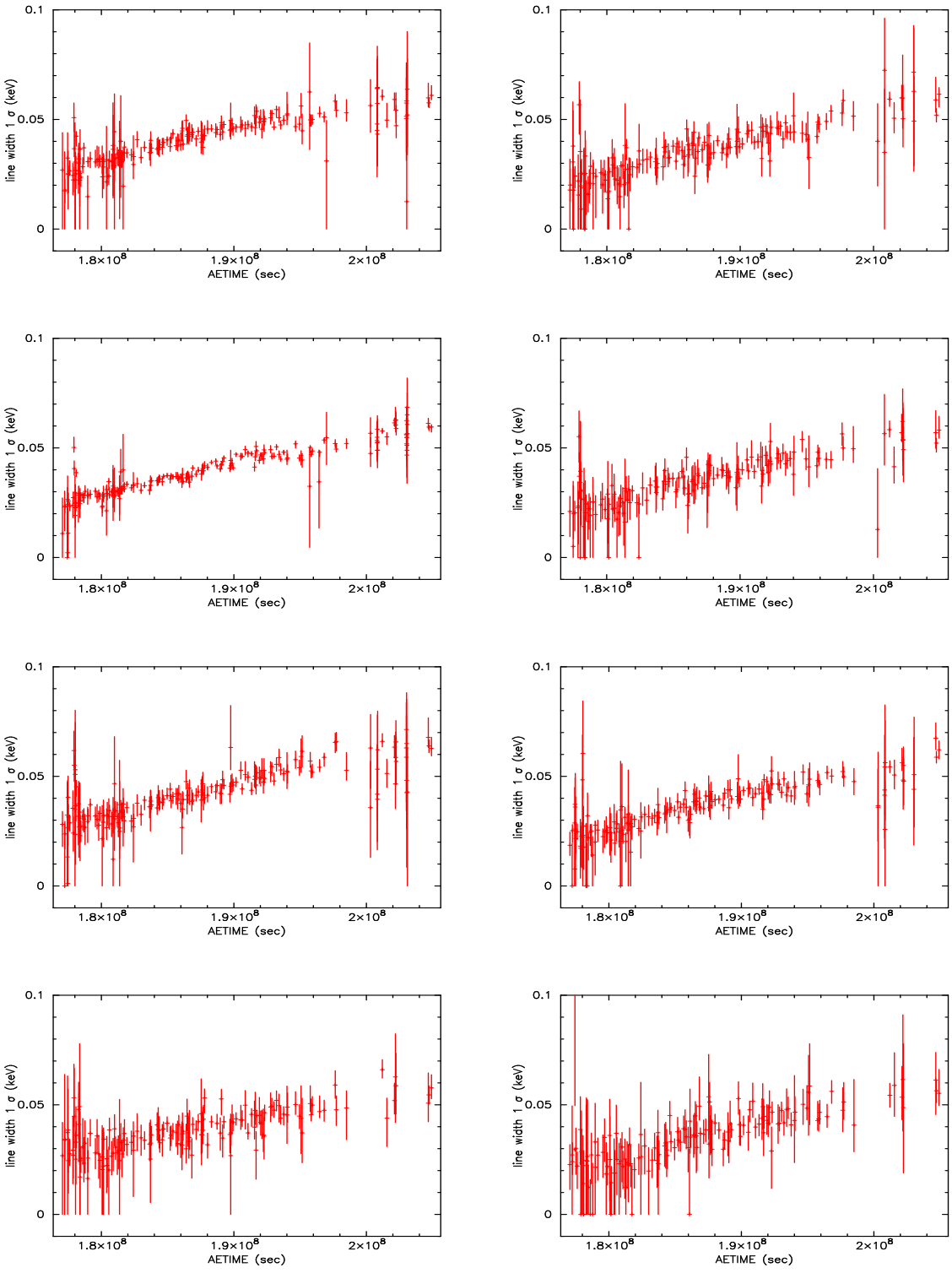

Figure 5.12: The same as figure 5.2, but after the CTI_{CI} correction.

Chapter 6

Review of Multiple Supernovae and Superbubble

6.1 Supernova Explosion

6.1.1 Shock Waves

Shock waves play the essential roles in the dynamics in SNRs. It is a transition region between upstream and downstream states of a fluid through which there is a net mass flux and across which mass, momentum, and energy flux are conserved but entropy per unit mass and mass density increase. Here we describe fluid equations and relations between some physical parameters.

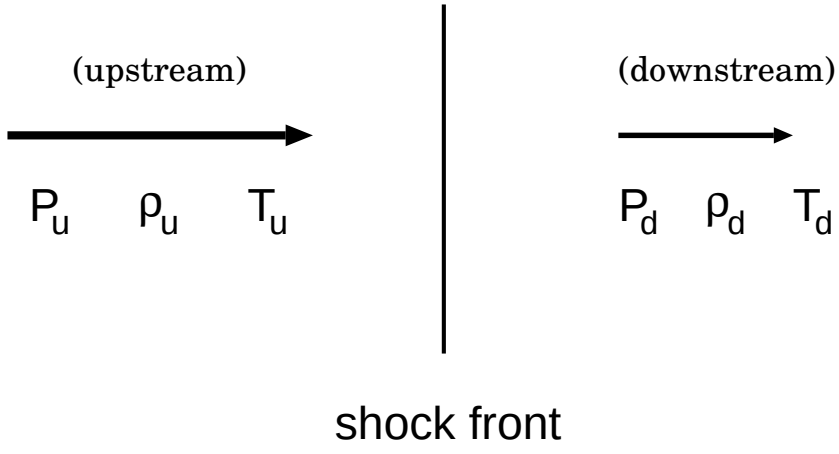

Figure 6.1: A schematic view around the shock front.

In a coordinate at the shock front, the conservation of mass, energy, and momentum are described as

$$\frac{\partial \rho}{\partial t} + \frac{\partial (\rho v)}{\partial x} = 0 \tag{6.1}$$

$$\frac{\partial(\rho v)}{\partial t} + \frac{\partial(\rho v^2 + P)}{\partial x} = 0 \tag{6.2}$$

$$\frac{\partial}{\partial t}\{\rho(\frac{1}{2}v^2 + E)\} + \frac{\partial}{\partial x}\{Pv + \rho(\frac{1}{2}v^2 + E)v\} = 0 \tag{6.3}$$

where ρ, v, P, and E are density, velocity, pressure, and energy per unit mass, respectively. These continuity equations can be rewritten as follows in a Lagrangian coordinate for the situation in figure 6.1.

$$\rho_{\rm u} v_{\rm u} = \rho_{\rm d} v_{\rm d} \tag{6.4}$$

$$\rho_{\rm u} v_{\rm u}^2 + P_{\rm u} = \rho_{\rm d} v_{\rm d}^2 + P_{\rm d} \tag{6.5}$$

$$v_{\rm u}\{P_{\rm u} + \rho_{\rm u}(\frac{1}{2}v_{\rm u}^2 + E_{\rm u})\} = v_{\rm d}\{P_{\rm d} + \rho_{\rm d}(\frac{1}{2}v_{\rm d}^2 + E_{\rm d})\} \tag{6.6}$$

where subscripts u and d denote upstream and downstream, respectively. The equation 6.6 for the ideal gas is changed to the formula, together with the equation 6.4

$$\frac{1}{2}v_{\rm u}^2 + \frac{\gamma}{\gamma-1}\frac{P_{\rm u}}{\rho_{\rm u}} = \frac{1}{2}v_{\rm d}^2 + \frac{\gamma}{\gamma-1}\frac{P_{\rm d}}{\rho_{\rm d}} \tag{6.7}$$

where γ is specific-heat ratio. From the equations 6.4, 6.5, 6.7, and the equation of state for ideal gas, we obtain

$$\frac{\rho_{\rm d}}{\rho_{\rm u}} = \frac{v_{\rm u}}{v_{\rm d}} = \frac{(\gamma-1)P_{\rm u} + (\gamma+1)P_{\rm d}}{(\gamma+1)P_{\rm u} + (\gamma-1)P_{\rm d}} \tag{6.8}$$

$$\frac{T_{\rm u}}{T_{\rm d}} = \frac{P_{\rm u}}{P_{\rm d}} \cdot \frac{(\gamma-1)P_{\rm u} + (\gamma+1)P_{\rm d}}{(\gamma+1)P_{\rm u} + (\gamma-1)P_{\rm d}}. \tag{6.9}$$

These formulae holds between thermodynamic quantities on the two sides of the surface of discontinuity and is known as Rankine-Hugoniot relations. For the velocities of the gas across the shock wave, we have

$$v_{\rm u}^2 = \frac{1}{2\rho_{\rm u}}\{(\gamma-1)P_{\rm u} + (\gamma+1)P_{\rm d}\} \tag{6.10}$$

$$v_{\rm d}^2 = \frac{1}{2\rho_{\rm u}}\frac{\{(\gamma+1)P_{\rm u} + (\gamma-1)P_{\rm d}\}^2}{\{(\gamma-1)P_{\rm u} + (\gamma+1)P_{\rm d}\}} \tag{6.11}$$

Here we supply some useful equations for the ratio of densities, pressures, and temperatures in terms of the Mach number $M_{\rm u} = v_{\rm u}/C_{\rm u}$, where $C_{\rm u}$ is the sound velocity.

$$\frac{\rho_{\rm d}}{\rho_{\rm u}} = \frac{(\gamma+1)M_{\rm u}^2}{(\gamma-1)M_{\rm u}^2 + 2} = \frac{4M_{\rm u}^2}{M_{\rm u}^2 + 3} \tag{6.12}$$

$$\frac{p_{\rm d}}{p_{\rm u}} = \frac{2\gamma M_{\rm u}^2}{\gamma+1} - \frac{\gamma-1}{\gamma+1} = \frac{5M_{\rm u}^2 - 1}{4} \tag{6.13}$$

$$\frac{T_{\rm d}}{T_{\rm u}} = \frac{\{2\gamma M_{\rm u}^2 - (\gamma-1)\}\{(\gamma-1)M_{\rm u}^2 + 2\}}{(\gamma+1)^2 M_{\rm u}^2} = \frac{(5M_{\rm u}^2 - 1)(M_{\rm u}^2 + 3)}{16M_{\rm u}^2} \tag{6.14}$$

The Mach number $M_{\rm d}$ is also given in terms of $M_{\rm u}$ by

$$M_{\rm d}^2 = \frac{2+(\gamma-1)M_{\rm u}^2}{2\gamma M_{\rm u}^2-(\gamma-1)} = \frac{M_{\rm u}^2+3}{5M_{\rm u}^2-1} \tag{6.15}$$

In the case of $P_{\rm u} \ll P_{\rm d}$ (strong shock),

$$\frac{\rho_{\rm d}}{\rho_{\rm u}} = \frac{v_{\rm u}}{v_{\rm d}} = \frac{\gamma+1}{\gamma-1} \tag{6.16}$$

$$v_{\rm u} = \sqrt{\frac{1}{2}(\gamma+1)\frac{P_{\rm d}}{\rho_{\rm u}}} \tag{6.17}$$

$$v_{\rm d} = \sqrt{\frac{1}{2}\frac{(\gamma-1)^2 P_{\rm d}}{(\gamma+1)\rho_{\rm u}}} \tag{6.18}$$

$v_{\rm u}$ and $v_{\rm d}$ are defined in a coordinate where the shock front has null velocity. In the observer's coordinate, $v_{\rm u}$ equals the shock velocity ($\equiv v_{\rm s}$) . Using the equation of state, the post-shock velocity $v_{\rm p} \equiv v_{\rm u} - v_{\rm d}$, post-shock pressure $P_{\rm p} \equiv P_{\rm d}$, and the post-shock temperature $T_{\rm p} \equiv T_{\rm d}$ are obtained as

$$v_{\rm p} = \frac{2v_{\rm s}}{\gamma+1} \tag{6.19}$$

$$P_{\rm p} = \frac{2\rho_{\rm u}v_{\rm s}^2}{\gamma+1} \tag{6.20}$$

$$kT_{\rm p} = P_{\rm p}\frac{\mu}{\rho_{\rm d}} = \frac{2(\gamma-1)}{(\gamma+1)^2}\mu v_{\rm s}^2 \tag{6.21}$$

where μ is the mean atomic weight, and k is the Boltzmann constant. In the case of $\gamma = \frac{5}{3}$ (monoatomic gas), we obtain The post-shock temperature is determined by the shock speed only.

$$kT_p = \frac{3}{16}\mu v_{\rm s}^2 \tag{6.22}$$

$$\frac{\rho_{\rm d}}{\rho_{\rm u}} = \frac{v_{\rm u}}{v_{\rm d}} = 4 \tag{6.23}$$

6.1.2 Nuclear Synthesis

Just after the Big Bang, the universe contained only hydrogen and helium with tiny traces of other light elements like lithium. Heavier elements were, and continue to be, "synthesized" deep in the interiors of stars by step-by-step process of nuclear fusion, so-called nucleosynthesis. These newly formed chemical species were spewed out into the interstellar space by the supernova explosions, together with still heavier atomic nuclei that were fused during the explosion.

How far the process of nucleosynthesis proceeds in a star depends on its mass. Stars like Sun normally produce elements as heavy as carbon and oxygen, but their

densities and temperatures are too low to fuse these into heavier elements. More massive stars do support the required conditions to synthesize elements such as oxygen, magnesium, silicon, and iron, as well as some heavier ones. Therefore, different types of SNe have different progenitors, thus producing different heavy elements on different time-scales during the chemical evolution of galaxies.

Tsujimoto et al. (1995) predicted nucleosynthesis products of Type Ia and Type II SNe, assuming that the stars initially more massive than 10 $M_\odot$ explode as Type II SNe if they are single stars, or as Type Ib/Ic SNe if they belong to close binary systems. Figure 6.2 shows the predicted relative abundances of synthesized heavy elements by Tsujimoto et al. (1995), which are normalized to the corresponding cosmic abundances of Tokunaga (2000). The abundance of Mg is normalized to 1.

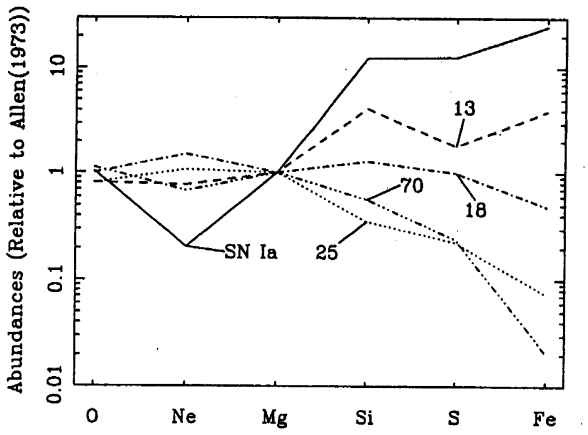

Figure 6.2: The predicted relative abundances of synthesized heavy elements (Tsujimoto et al. 1995). The predicted relative abundances of synthesized heavy elements. The ratios to the cosmic abundances of Tokunaga (2000) are plotted for SN Ia and SN II of 13, 18, 25, and 70$M_\odot$ stars.

6.1.3 Evolution of Supernova Remnants

At the time of SN explosion, most of the mass of the progenitor is ejected outward with high velocity. The evolution of the SNR depends on the ejected mass (M_0), swept up mass (M_b), and radiated energy. Here we describe the brief summary of SNR evolution.

The almost all of the initial explosion energy is converted to the kinetic energy of the ejecta. Just after the explosion, the ejecta flies supersonically with respect to the background and thus establishes the main shock that sweeps the surrounding gas. At first, the ejecta is undecelerated and the remnant is in its "free expansion" phase ($M_0 > M_\mathrm{b}$). The velocity of the ejecta is as high as $v_0 \sim(5 - 10)\times10^3$ km s^{-1}. Soon a reverse shock, built and supported by the high pressure of the increasing amount of swept up matter, begins to thermalize it.

When the thermalized ejecta mass and that of the swept up ISM become comparable, the radius and age of the remnant are

$$R_{\rm s} = \frac{(3M_0)^{(1/3)}}{(4\pi\mu m_H n_{\rm b})^{(1/3)}} = \left(\frac{M_0}{1M_\odot}\right)^{1/3} \left(\frac{\mu}{1.36}\right)^{-1/3} \left(\frac{n_0}{1\,{\rm cm}^{-3}}\right)^{-1/3} {\rm pc} \quad (6.24)$$

$$t \approx R_{\rm s} v_0^{-1} \approx 190 \text{ yr}. \quad (6.25)$$

Here we assumed that the mean ambient hydrogen density of n_0= 1 cm^{-3}, and with $M_0 = 1M_\odot$, $v_0 = 10^4$ km s^{-1}, and $\mu = 1.36$ (mean atomic weight of cosmic material per H atom; Tokunaga 2000). The thermalized ejecta radiates X-ray, hence the X-ray spectroscopy of this phase of SNRs can be a powerful tool to investigate the chemical composition of heavy elements synthesized by SN events.

The free expansion lasts until the reverse shock runs through the whole ejecta. By then, the remnant would have enter the so-called "adiabatic" or "Sedov" phase of its evolution. Shklovskii (1962) proved that the SN explosion within the ISM can be linked to a powerful point explosion in a gas with constant heat capacity. He also proved that the self-similar (Sedov 1959) solution was applicable to this phenomena. However, as shown by Gull (1973), a mass comparable to ten times that of the ejected matter must be swept up before the outer portions of the remnant begin to resemble the standard (Sedov 1959) solutions, and some 50 times the ejected mass should be swept up before full thermalization of the ejecta is completed. Thus, free expansion, thermalization and the beginning of the Sedov phase overlap in time. Ostriker & McKee (1988) introduced the equations which describes the motion during Sedov phase as follows:

$$R_{\rm s} = 0.31\ n_0^{-0.2}\ E_{51}^{0.2}\ t^{0.4}\ {\rm pc} \quad (6.26)$$

$$V_{\rm s} \equiv \frac{dR_{\rm s}}{dt} = \frac{2}{5}\ \frac{R_{\rm s}}{t}. \quad (6.27)$$

$R_{\rm s}$, $V_{\rm s}$, n_0, E_{51}, and t are the radius, velocity of the shock front, ambient density, initial explosion energy in the unit of 10^{51} ergs, and the age in the unit of year, respectively.

With the equation (6.22), the shock temperature is given as

$$kT_{\rm s} = \frac{3}{16}\ \mu\ V_{\rm s}^2 = 1.7 \times 10^4\ n_a^{-0.4}\ E_{51}^{0.4}\ t^{-1.2}\ {\rm keV} \quad (6.28)$$

During the Sedov phase, remnants conserve energy, both thermal ($E_{\rm th} = 0.72E_0$) and kinetic ($E_{\rm th} = 0.28E_0$) energy (Chevalier 1974), and grow with time as $t^{2/5}$ while the leading shock velocity decays as $t^{-3/5}$.

The decay in shock speed leads eventually to a cooling time comparable to the dynamical time, and this marks the beginning of the radiative phase which promotes the formation of a dense shell at the edge of the remnant (Cox 1972). At this moment, the shock velocity is decelerated down to $\sim$ 200 km s^{-1} and the gas temperature is about $kT \sim (4-5) \times 10^{-2}$ keV. By this time, about half of the thermal energy has been radiated away. In the early radiative stages, the interior of

the remnant is still filled with the hot ejecta and the hot ISM, shocked earlier in the evolution, and both do work on the outer shock front for as long as the pressure is continuous across the remnant and with the same value across the dense shell. According to Falle (1981) and Falle (1988), the age $t_{\rm cool}$, radius $R_{\rm cool}$, and expansion velocity $V_{\rm cool}$ of SNR in the radiative cooling phase are expressed as,

$$t_{\rm cool} = 2.7\times10^4 E_{51}^{0.24} n_0^{-0.52}\ {\rm yr}, \quad (6.29)$$
$$R_{\rm cool} = 20 E_{51}^{0.295} n_0^{-0.409}\ {\rm pc}, \quad (6.30)$$
$$V_{\rm cool} = 277 E_{51}^{0.0554} n_0^{0.111}\ {\rm km\ s^{-1}}. \quad (6.31)$$

The remnant is then in the "pressure-driven snowplow" phase (Oort 1951). The law of motion governing the shell at this stage can be derived from the adiabatic expansion condition imposed on the interior hot gas,

$$\frac{{\rm d}E_{\rm T}}{{\rm d}t} = -4\pi R_{\rm s} P \frac{{\rm d}R_{\rm s}}{{\rm d}t}, \quad (6.32)$$
$$\frac{4\pi}{3} R_{\rm s}^3 P = (\gamma-1) E_{\rm T} \quad (6.33)$$

and the equation for the mass and momentum of the shell

$$M = \frac{4\pi}{3} R_{\rm s}^3 \rho_0, \quad (6.34)$$
$$\frac{{\rm d}(MV_{\rm s})}{{\rm d}t} = 4\pi R_{\rm s}^2 P, \quad (6.35)$$
$$\frac{{\rm d}R_{\rm s}}{{\rm d}t} = V_{\rm s}. \quad (6.36)$$

Here P is the pressure of the hot gas, the thickness of the shell is assumed to be small compared to its radius, and the mass of the hot gas is assumed to be much less than that of the shell. With equation(6.33) and equation(6.36), McKee & Ostriker (1977) and Blinnikov et al. (1982) got a solution as follows,

$$R_{\rm s} = 38(\epsilon E_{51})^{5/21} n_0^{-5/21} (\frac{t}{10^5 yr})^{2/7}\ {\rm pc}, \quad (6.37)$$
$$V_{\rm s} = \frac{2}{7}\frac{R_{\rm s}}{t}, \quad (6.38)$$

where $\epsilon = E_{\rm T}/E_0 = 0.2$ - 0.35.

Once the interior pressure becomes negligible, the remnant evolves as a pure "momentum-driven snowplow", its radius then grow as $t^{1/4}$, and the shock speed decays as $t^{-3/4}$, even faster than in the Sedov phase. When the expansion velocity is as small as ~ 10 - 20 km s^{-1}, which is about the same as the velocity of proper motion of the ambient interstellar matter, the remnant begins to melt into the ISM. If the remnant structure does not interact with other ones, it will eventually disappear by fragmentation of the shell and by replacement of the cooling low-density gas by expanding cooler material from the ISM (Cox & Smith 1974).

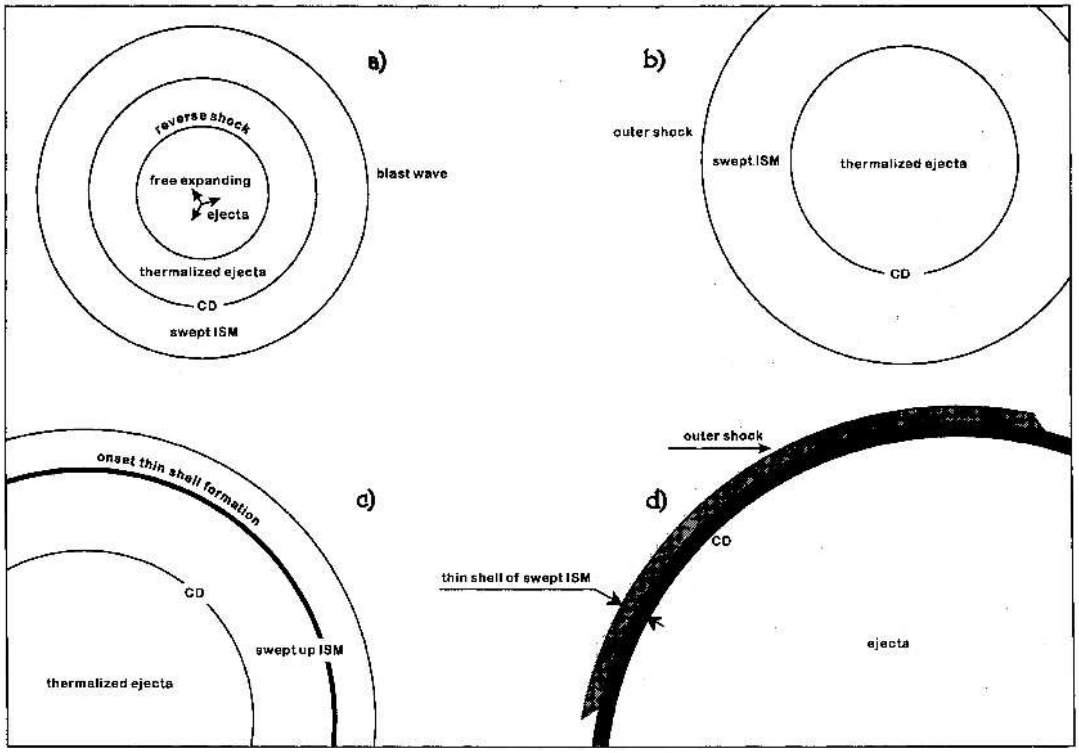

Figure 6.3: The evolution of SNRs. Schematic representation of the main structural changes adopted by the shocked gases as a result of a sudden release of energy ($E \sim 10^{51}$ergs) into a uniform density medium ($n \sim 1$ cm^{-3}). This figure is adopted from Tenorio-Tagle (1996).

6.2 Superbubble

6.2.1 Formation of Superbubble

Young massive stars which have strong winds and explode as type Ib/Ic or II SN are known to be spatially and temporally correlated with OB associations. Massive stars are formed in groups by the collapse of molecular clouds. Because of their short lifetimes of 3 - 20 Myr (Schaller et al. 1992) and small dispersion velocities of 4 - 6 km s^{-1} (Blaauw 1991; Mel'nik & Efremov 1995), SN progenitors remain and explode close to their birth place. Although identifying the membership of a given OB association is not an easy task from the observational point of view, it is reliably estimated that between 60% (Garmany 1994) and 95% (Higdon et al. 1998) of all OB stars belong to such associations, which contains up to several OB stars within regions of radius $R_{\rm OB} \sim 35$ pc (Garmany 1994; Bresolin et al. 1999; Pietrzyński et al. 2001, and references therein).

For evenly distributed stars, the mean distance between two closest neighbours can be evaluated as $D_{\rm dis} \simeq (4\pi R_{\rm OB}^3/3N_{\rm OB})^{1/3}$, so that each star can be considered as occupying an individual spherical volume of radius $R_{\rm dis} \simeq D_{\rm dis}/2$, with typical value:

$$R_{\rm dis} \simeq 6 \text{ pc } \left(\frac{R_{\rm OB}}{35{\rm pc}}\right)\left(\frac{N_{\rm OB}}{100}\right)^{1/3}. \tag{6.39}$$

An important characteristic of such stars is that they experience strong winds during most of their lifetime. The mass-loss rate and the wind velocity, and thus the wind power, are not constant during stellar evolution (Meynet et al. 1994), but the total wind energy, integrated over a massive star's lifetime, amounts typically to 10^{51} erg and is therefore comparable to the final SN explosion energy itself. When considering the energy output of OB stars in the Galaxy, one thus has to include the contribution of the winds, which can roughly double the energy imparted to cosmic rays if the wind energy can somehow be used to accelerate particles.

After a few ($\leq$5) explosions and/or strong stellar winds, once the remnant has grown to a large radius, all subsequent explosions lead to blast waves which, by evolving into the hot gas produced by former SNe decay into sound waves (Tenorio-Tagle et al. 1987; Mac Low & McCray 1988; De Young & Gallagher 1990; Tenorio-Tagle 1996). In this way, the kinetic energy deposited by the stellar cluster is fully thermalized without disrupting the pattern shown in figure 6.3. Following SN explosions may occur in the cavity formed by preceding ones and/or strong stellar winds from OB-type stars. As a result, the correlated core-collapsed SNe explosions create giant cavities of hot, tenuous plasma, which is called SBs, rather than many smaller isolated remnant bubbles (McCray & Snow 1979).

Higdon & Lingenfelter (2005) determined quantitatively the fraction of Galactic core-collapse SN that occur in SBs. The fraction of core-collapse SN (Type II and Ib/c) occurring in SBs is high, ranging from ∼80% (solely temporal correlations) to ∼90% (only spatial sorrelations). Core-collapse SNe constitute 85% of Galacic SNe (van den Bergh & McClure 1994); only a small fraction of the remaining SNe, Type

Ia, occur in SBs. Thus, ∼75% of all Galactic SNe are expected to occur within SBs.

The deficiency of bright Galactic radio SNR shells is well-known issue (Clark & Caswell 1976). This can be most simply seen from the fact that there are only a few SNR shells (Green 2004) with radio surface brightness >1% of that of the brightest remnant, the ∼300 yr old Cas A. From various models (Berezhko & Völk 2004) of radio emission in the Sedov phase of SN expansion, the radio surface brightness of Cas A would be expected to remain above 1% of its present value for another 2000 - 4000 yr, so with a Galactic SN rate of one every 40 yr, we could expect to find between 50 and 100 radio SNR at least that bright. This is more than 10 times that observed. Higdon & Lingenfelter (1980) suggest that this discrepancy results from the fact that most SN occur in the hot, tenuous ($\sim 3\times10^{-3}$ cm^{-3}) phase of the ISM, where their remnants have to expand to much larger volumes than in the denser phases of the ISM to sweep up enough matter to enter the Sedov phase. As a result, the peak surface brightness of remnants is the hot, tenuous phase is much lower than that of those in the denser phases (Berezhko & Völk 2004). Koo & Kang (2004) have recently suggested that the same effect may account for the deficiency of observed HI SNRs in the inner Galaxy.

6.2.2 Evolution of Superbubble

The theories of SB evolution are based on the standard wind bubble theory (Weaver et al. 1977). In order to grasp the typical values of basic physical quantities inside the SB, here we follow Mac Low & McCray (1988) and assume that the SB is expanding in a homogeneous medium of density n_0, powered by the activity of an OB association providing a constant mechanical luminosity of $L_{\rm OB}$. Although the energy release is not continuous and experience strong peaks when an OB star enters the Wolf-Rayet stage or when a new SN explodes, the variation of the driving power are smoothed out for sufficiently evolved SBs because the shells of individual SN shocks become subsonic before they reach the shell. In addition, star formation is a sequential process in giant molecular clouds, and massive stars have a whole range of lifetimes. Hence as a first approximation, it can be assumed that the energy release is indeed roughly constant inside the SB, which allow us to treat the whole SB as a very large wind bubble.

With the above assumption, Mac Low & McCray (1988) follow Weaver et al. (1977) and Castor et al. (1975) to find the temperature and density inside the SB:

$$\begin{aligned} T_r &= (3.1\times10^6 \text{ K})\ L_{37}^{8/35}\ n_0^{2/35}\ t_6^{-6/35} \times (1-x)^{2/5} \qquad (6.40)\\ &= T_c(1-x)^{2/5} \\ n_r &= (1.1\times10^{-2} \text{ cm}^{-3})\ L_{37}^{6/35}\ n_0^{19/35}\ t_6^{-22/35} \times (1-x)^{-2/5} \qquad (6.41)\\ &= T_c(1-x)^{-2/5} \end{aligned}$$

where the n_0 is the external ISM density in cm^{-3}, t_6 is the age of the SB in units of 10^6 yr, $x = r/R$ is the relative distance from the SB center, and $(1-x)^{2/5}$ is a function giving the temperature and density gradient inside the SB, assuming that the energy

is injected at $x = 0$. The internal pressure, i.e. the product $P_{\rm SB} = \mu n_{\rm SB} k_{\rm B} T_{\rm SB}$, which independent of $(1-x)^{2/5}$ as the sound crossing time is lower than the SB dynamical time. Here we assume a particle multiplicity $\mu \simeq 2.3$, taking into account the contribution of the electrons to the pressure (the SB interior is here assumed to be fully ionized, with solar abundances).

The SB internal pressure thus reads:

$$P_{\rm SB} = (4.3 \times 10^{-12} \text{ dyne cm}^{-2}) \; L_{37}^{2/5} \; n_0^{3/5} \; t_7^{-4/5} \tag{6.42}$$

Given the $P_{\rm SB}$, one can calculate the radius of a stellar wind terminal shock, around a given OB stars with a wind power ($L_{\rm w}$) and a wind velocity ($V_{\rm w}$) by considering the condition of $P_{\rm SB}$ is equal to the wind ram pressure ($P_{\rm ram}$). Then one obtain

$$R_{\rm term} = (20 \text{ pc}) \; L_{\rm w,37}^{1/2} \; V_{\rm w,3}^{-1/2} \; L_{\rm OB,38}^{-1/5} \; n_0^{-3/10} \; t_7^{2/5} \tag{6.43}$$

This radius can be larger than R, hence the direct wind-wind interaction should occurs inside SBs. Due to the low pressure inside the SB, the region containing unshocked wind material extends far enough around the star so that it may enter directly into contact with the unshocked wind material of another star, that is, the winds actually terminate each other, instead of being terminated by the surrounding medium. Then, the wind energy is efficiently converted into strong turbulence, and since the material is fully ionized, plasma waves should also rapidly develop and produce a magnetic turbulence with values of the magnetic field close to the equipartition value.

We now discuss in what differs the revolution of SNRs in SBs from those which explode in the average ISM, that is, isolated SNe.

A major difference is the fact that the density and temperature of the internal cavity are modified by subsequent explosions, and soon achieve values typical of a "coronal medium" ($n = 10^2$ - 10^3 cm^{-3}, $T > 10^6$ K). Thus, all SN exploding after the first one at the center of the evolving remnant encounter an increasingly hotter and rarefied medium. The lower density results in a quicker growth of the SNR shell, and a higher temperature in a higher sound speed. The transition to a Sedov-like expansion occurs when a mass of roughly 1.6 M_{eje} is swept-up by the ejecta (McKee & Truelove 1995). In a medium of density 4×10^{-3}cm^{-3}, which corresponds to the case of typical SB after 10^7 yr of evolution, this occurs when the SNR reaches a radius $R_0 \simeq 30$ pc$M_{10}^{5/6} t_7^{0.21}$, i.e. $\sim 1.3 \times 10^4 yrs M_{10}^{5/6} t_7^{0.21} E_{51}^{-1/2}$ after the explosion (Truelove & McKee 1999).

In the Sedov-like phase, the SNR expands almost selfsimilarly, as from a point explosion, according to:

$$R_{\rm SNR} = (38 \text{ pc}) \; t_{\rm SNR,4}^{2/5} \; t_{\rm SB,7}^{22/175} \tag{6.44}$$

and

$$V_{\rm SNR} \simeq (1470 \text{ km s}^{-1}) \; t_{\rm SNR,4}^{-3/5} \; t_{\rm SB,7}^{22/175} \tag{6.45}$$

where we have replaced the ambient gas density by that of the SB interior given by equation 6.41 and used the values corresponding to typical SB, and where $t_{\rm SB,7}$ is the age of the SB in units of 10^7 yr and $t_{\rm SNR,4}$ the age of the SNR in units of 10^4 yr.

The above equations allow one to calculate the time when the shock becomes subsonic. Replacing the temperature $T_{\rm SB}$, from equation 6.40, in the expression of the sound velocity, $c_s = \sqrt{\gamma p/\rho} \simeq \sqrt{\gamma kT/(1.4 m_{\rm p})} \simeq 99 {\rm km\ s^{-1}} (T/10^6\ K)^{1/2}$ for γ= 3/5, one finds that $V_{\rm SNR} > c_s$ until

$$t_{\rm sub} \simeq (3.1 \times 10^5 \text{ yr})\ t_{\rm SB,7}^{37/105}. \tag{6.46}$$

By that time, the SNR has reached a radius

$$R_{\rm sub} \simeq (150 \text{ pc})\ t_{\rm SB,7}^{4/15}. \tag{6.47}$$

which can be compared to the radius of the SB itself:

$$R_{\rm SB} \simeq (267 \text{ pc})\ L_{\rm OB,38}^{1/5}\ n_0^{-1/5}\ t_7^{3/5}. \tag{6.48}$$

$R_{\rm sub} < R_{\rm SB}$ is satisfied even in the very early phase in the evolution of a SB (i.e. for the very first SN), and that $R_{\rm sub}/R_{\rm SB}$ still decrease as $0.56 t_7^{-1/3}$ as the SB evolves. This justified the statement above that the discrete energy release inside the SB are actually smoothed out and the growth of the SB can be worked out by assuming a continuous driving power.

Another characteristics is that the shell of a SN exploding inside a SB becomes subsonic before becoming radiative phase. Indeed, evaluating the cooling time of the shocked gas compared to the age of the SNR, Blondin et al. (1998) obtained the timescale for the end of the Sedov-like phase and the formation of a radiative shell as $t_{\rm rad} = 2.9 \times 10^4$ yr$E_{51}^{4/17}\ n_0^{-9/17}$. Replacing n_0 by the SB density and dividing by the time corresponding to the sonic transition, one find that

$$t_{\rm rad}/t_{\rm sub} \simeq 1.7 \times t_7^{-1/51} \tag{6.49}$$

is always larger than 1, indicating that the SNR will never become radiative inside the SB. One may therefore expect that SN shock waves remain in the Sedov-like phase (and thus keep its initial energy) until they die well inside the SB.

The radii of SBs formed as mentioned above range from those of ordinary SNR (<100 pc) to more than 1000 pc, and kinetic energies of expansion are up to 10^{54} ergs.

6.2.3 Cosmic Ray Acceleration in Superbubble

The question over the origin of cosmic rays (CRs) has persisted ever since they were first detected in 1912 by Victor Hess using a balloon-borne electroscope device (Hess 1912). Recently the spectra of CRs up to energies of 10^5 TeV were taken in balloon measurements by Apanasenko et al. (2001). These are power-law spectra without any features in this energy spectrum at energies $E = 10^2$ - 10^5 GeV per nucleon is approximately constant and close to $\gamma \approx 2.75$. The spectrum of heavy

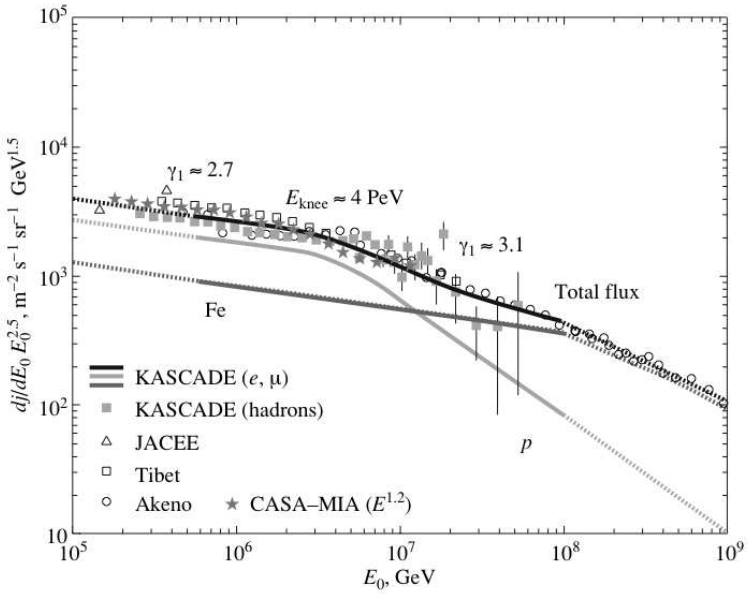

Figure 6.4: The CR spectrum for all nuclei, as measured with various facilities, and the expected behavior of the proton and iron spectra (Kampert et al. 2001). dj/dE_0 is the differential CR intensity related to the distribution function $F(E_0)$ by $dj/dE_0 = cF(E_0)$, where c is the speed of light.

nuclei in the same energy range is flatter, and its index appears to be close to $\gamma \approx 2.65$. These results were obtained both from observations of extended air showers and by direct measurements. At energies $E = 10^5$ - 10^7 GeV per nucleus, there is a feature (apparently a kink or a knee) in the CR energy spectrum summed over all nuclei. The shape of the feature has not been studied adequately. After the knee, the spectrum is again close to a power law with $\gamma \approx 3.1$ - 3.2 at energies $E \approx 10^7$ - $10^{9.5}$ GeV per nucleus (Bird et al. 1993). The spectrum breaks at energy $E \approx 10^{9.5}$ GeV per nucleus, and $\gamma \approx 2.7$ at $E \approx 10^{9.5}$ - $10^{10.6}$ GeV per nucleus (Bird et al. 1993).

In the energy band of $E \leq 10^{10.6}$ GeV, the gyro radius due to the Galactic magnetic field is significantly smaller than the thickness of the Galactic disk, and CR is blocked up in the Galactic disk changing its direction. In the case $E > E_{\rm knee}$, it is hard to bound CR inside the disk and they leak outside the disk, although the firm confirmation has not been obtained yet. In the very-high energy band of $E \geq 10^{10}$ GeV the gyro radius is almost the same or larger than the Galactic disk, hence it is hard to bound the CR in the disk. Because the CR of $E \geq 10^{10}$ GeV show almost uniform distribution, the origin of them seems to be extragalactic objects. There is now broad consensus that the shocks in the expanding blast waves of SNRs accelerate the bulk of the CR ions up to energies of $\sim$300 TeV nucleon^{-1}.

In fact, the discovery of power-law (non-thermal) X-rays from SN 1006 (Koyama et al. 1995) indicates the existence of extreme high energy charged particles by the first order Fermi process. This lead a successive discovery of new class of shell-like

SNRs such as RCW 86 (Bamba et al. 2000; Borkowski et al. 2001b), G266.2–1.2 (Slane et al. 2001), and G28.6–0.1 (Ueno et al. 2003). Some of the Galactic SNRs are also observed with γ-rays. RX J1713.7–3946 has proven to be a source of non-thermal X-rays, GeV γ-rays, and TeV γ-rays. The CANGAROO collaboration detected TeV γ-ray emission from the northwest rim, and the spectrum taken in the γ-ray band is consistent with π^0-decay γ-rays (Enomoto et al. 2002), which indicates SNR molecular cloud interaction. A molecular cloud has indeed been found at the northern perimeter by CO observation (Butt et al. 2001). Another SNR, γ Cygni, is associated with one of the brightest EGRET sources, and is also interacting with a dense cloud (Uchiyama et al. 2002)

However, according to the most optimistic estimates, the acceleration by single shock waves from SN explosions cannot account for the origin of the particles above the knee in the energy spectrum. Hence we take notice of SBs as potential candidates of the accelerator above the knee.

Although the diffusive shock acceleration mechanism is not fundamentally modified inside a SB, there are some important differences compared to the isolated SNRs.

First, the presence of a turbulent and magnetized medium in front of the shock exits. Recent study of diffusive shock acceleration has shown that the efficiency of particle acceleration around strong shocks and the maximum energy ($E_{\rm max}$) crucially depend on the level of turbulence and the value of the magnetic field (Lucke & Hodge 1970; Berezhko et al. 2003; Ptuskin & Zirakashvili 2003). Since the size of SNRs and the acceleration duration is limited, large values of $E_{\rm max}$ require low diffusion coefficient. A lower limit to the diffusion coefficient along magnetic field lines is provided by the so-called Bohm scaling, where $D_{\rm B} = \frac{1}{3} v r_g$ and $r_g = \gamma m v / qB$ is the gyro radius of the particle of mass m, charge $q = Ze$ and Lorentz factor γ in a field of strength B. These give $D_{\rm B} \simeq 3.1 \times 10^{22} \gamma \beta^2 Z^{-1} B_{\mu{\rm G}}^{-1}$ cm^2 s^{-1}. To lower this value, and thus increase $E_{\rm max}$, one needs larger magnetic fields. Although direct measurements of the magnetic fields inside SBs are not available, one can estimate that it is indeed larger than in the average ISM, due to the mechanisms such as turbulence generation through direct wind-wind interactions. Assuming the equipartition of the mechanical energy released by the massive stars between thermal pressure, turbulence and magnetic fields, one can obtain magnetic fields of the order of 10 - 20 μG.

Furthermore, the turbulence flow inside the SB should also make the acceleration efficiency higher than an isolated SNR. In the isolated SNR, particle injection in the acceleration process is provided by the tail of the thermal distribution (Völk et al. 2003), which limits the fraction of particles flowing through the shock front to be eventually accelerated to about 10^{-4} or 10^{-3} at most. In the case of an SNR in a SB, all the pre-existing energetic particles passing through the shock will see the discontinuity and be able to gain energy by diffusing back and forth across the shock front.

Assuming an amplification factor $\alpha_{\rm B}$, one can roughly estimate the maximum energy obtained from standard diffusive acceleration inside SBs by following Ptuskin & Zirakashvili (2003) as

$$E_{\max} \simeq (1.7 \times 10^{17}\ \mathrm{eV}) \times Z \left(\frac{\alpha_{\mathrm{B}}}{20}\right) \left(\frac{B_{\mathrm{SB}}}{10\mu G}\right). \tag{6.50}$$

We see that values of $E_{\max}$ of the order of $Z \times 10^{17}$ eV (as would be required in order to reach the ankle of the CR energy distribution), require values of α_{B} of the order of 10 - 20. This corresponds to enhanced values of the magnetic field at the shock of the order of 100 - 200 μG, which is unreasonable compared to what is usually assumed in isolated SNRs.

According to Bykov & Fleishman (1992), CR acceleration time is estimated to be about 3×10^5 yr and the maximum energy should exceed 3×10^{14} eV.

Because the lifetime of an SN blast wave is of the same order as the time scale between two explosions ($\sim 3 \times 10^5$ yr), the number of coexisting primary SN shocks inside an SB must be small ($\leq$2). Then multiple strong spherical SN shocks simultaneously in one SB would require an extreme SN rate in SB. However, repeated shock acceleration is possible and must actually occur for relatively low-energy particle. If the time required for them to leave the SB is larger than the typical time between two SN explosions, they may be overcome by a subsequent shock, and thus be injected into a new Diffusive Sshock Acceleration (DSA) site.

The typical escape time is given by $\tau_{\mathrm{esc}} \sim R^2/2D$, where $D(E)$ is the average diffusion coefficient in the SB. Casse et al. (2002) showed that variation law of the diffusion coefficient with rigidity depends on the ratio of the particle gyro radius to the principal length scale of the turbulence. The diffusion coefficient is estimated for a turbulent length scale of the order of the typical distance between massive stars. For the characteristics of typical OB association, one obtains $D_E \simeq (1.0 \times 10^{27} \mathrm{cm}^2\ \mathrm{s}^{-1}$.

Then maximum energy acquired by the repeated shock acceleration can be estimated to be

$$E_{\max} \simeq 11\ \mathrm{TeV} \times \eta_{\mathrm{T}} \left(\frac{B_{\mathrm{SB}}}{10\mu G}\right) \left(\frac{\lambda_{\max}}{6\mathrm{pc}}\right)^{-2}, \tag{6.51}$$

where $\lambda_{\max}$ is the principal length of the turbulence.

6.2.4 X-ray emission from SBs

To find L_{X}, we integrate the X-ray emissivity Λ_{X} in the layer of shocked stellar wind:

$$L_{\mathrm{X}} = \int n(r)^2 \Lambda_{\mathrm{X}}[T(r)]\, d^3 r \tag{6.52}$$

For the temperature range of $10^6 - 10^7$ K, then emissivity within the soft energy band of <2 keV is virtually independent of temperature, and $\Lambda_{\mathrm{X}}(T)$ can be approximated by a constant, $3 \times 10^{-23} \mathrm{ergscm}^3\mathrm{s}^{-1}$ for a solar abundance (Raymond & Smith 1977). On the context of equations 6.40 and 6.41, the radius of the bubble is

$$R = (42\ \mathrm{pc})\ L_{37}^{1/5} n_0^{-1/5} t_6^{3/5}. \tag{6.53}$$

The X-ray luminosity can be driven by integrating equation 6.52 from the center to a radius $R_{\rm max}$, while the temperature drops to the minimum that will emit in the soft-energy band, $T_{\rm min}$. Defining a dimensionless temperature $\tau = T_{min}/T_c$, the X-ray luminosity can be expressed as

$$L_{\rm X} = (1.1 \times 10^{35}\ {\rm ergs\ s^{-1}})\ \xi I(\tau) L_{37}^{33/35} n_0^{17/35} t_6^{19/35}, \tag{6.54}$$

where the dimensionless integral is $I(\tau) = (125/33) - 5\tau^{1/2} + (5/3)\tau^3 - (5/11)\tau^{11/2}$, and the metallicity relative to the Galactic (or solar) value is ξ. In scaled units here, $\tau = 0.16\ L_{37}^{-8/35} n_0^{-2/35} t_6^{6/35}$, so $I(\tau) \sim 2$. For the practical use, the X-ray emission should be expressed in physical parameters that are observable, such as size, expansion velocity, and density. The time derivative of equation 6.53 gives expansion velocity $V_{\rm exp}$,

$$V_{\rm exp} = (0.59\ {\rm km\ s^{-1}})\ R_{\rm pc}/t_6, \tag{6.55}$$

where the $R_{\rm pc}$ is the radius in units of pc. Combining equations 6.53, 6.54, and 6.55,

$$L_{\rm X} = (8.2 \times 10^{27}\ {\rm ergs\ s^{-1}})\ \xi I(\tau) n_0^{10/7} R_{\rm pc}^{17/7} V_5^{16/7}, \tag{6.56}$$

where V_5 is the expansion velocity in units of km s^{-1}. The ambient density n_0 cannot be measured directly, but it can be determined indirectly from the electron density in the shell, $n_{\rm e}$. For a pressure-driven SB, the ambient density is related to the shell density by

$$n_0 = (9/7)\ n_e k T_{\rm e}/(\mu_{\rm a} V_{\rm exp}^2), \tag{6.57}$$

where $T_{\rm e}$ is the electron temperature in the shell and $\mu_{\rm a} = (14/11) m_{\rm H}$ (Weaver et al. 1977; Chu & Mac Low 1990). The shell electron density $n_{\rm e}$ can be approximated by the rms electron density $n_{\rm e}$ (rms) determined from the Hα surface brightness. For a shell of thickness ΔR, measured in pc,

$$n_{\rm e} = \langle n_{\rm e}^2 \rangle = \frac{\rm EM}{2R_{\rm pc}[2(\Delta R/R_{\rm pc}) - (\Delta R/R_{\rm pc})^2]^{1/2}}, \tag{6.58}$$

where EM is the peak emission measure in units of cm^{-6} pc. It may be further assumed that the interstellar matter in the volume within radius R has been swept into a shell of thickness ΔR, hence

$$\frac{\Delta R}{R} = \frac{1}{3}\frac{n_0}{n_{\rm e}}. \tag{6.59}$$

If the expansion velocity, electron temperature, and peak emission measure of a SB are known, shell thickness and ambient density may be derived from equations 6.57, 6.58, and 6.59. equation 6.54 indicates that $L_{\rm X}$ grows as a bubble ages. However, detectability depends on the surface brightness, which is proportional to $L_{37}^{19/35} n_0^{31/35} t_6^{-23/35}$. Hence, the detectability actually diminishes as a bubble ages.

6.2.5 Past Observations

The observations of SBs have been concentrated on the Large Magellanic Cloud (LMC) because the LMC is an ideal laboratory for the observation of SBs. Because we know the distance to the LMC as 50 kpc with small uncertainty (Feast 1999), we are able to derive diameter of SBs (1 pc = 4 arcsec). There are many extended HII regions of 75 - 150 pc in size connected with OB associations in the LMC (McGee et al. 1978; Mathewson et al. 1985), which have the radio-bright emission. A weak linear polarization has been detected in the radio emission from 30 Dor nebula in the LMC (Haynes et al. 1990). Hence it can be said that the radio fluxes are produced by the synchrotron emission of non-thermal electrons. Calculated synchrotron flux fits the observed one if $N_{\rm e} \sim 10^{-11}$ cm^{-3} (Bykov & Fleishman 1992). Here the energy density of the non-thermal electrons appears to be equal to a few percent of the kinetic energy density of the system.

An excess of diffuse X-ray emission in SBs indicates the presence of interior supernova remnants shocking the inner walls of the SB shell (Chu & Mac Low 1990; Wang & Helfand 1991; Dunne et al. 2001). In Chu & Mac Low (1990), *Einstein* observations were used to show that seven LMC SBs are diffuse X-ray sources with luminosities much higher than those expected by the wind-blown, pressure-driven bubble models of Weaver et al. (1977). Off-center SNRs are proposed to be responsible for the excess X-ray emission. *ROSAT* observations of the SB N44 confirmed its diffuse X-ray emission and provided the first useful X-ray spectra of N44 for determinations of plasma temperatures (Chu et al. 1993). To illustrate that excess X-ray emission from SBs is caused by an intermittent process, Chu et al. (1995) analyzed the *ROSAT* observations of four X-ray–dim SBs and showed that these SBs do not have excess X-ray emission. However, comparing the observed X-ray luminosities to the predicted luminosities, they found that the observed values are surprisingly similar to the theoretical predictions. For high-resolution spectral analysis, *ASCA* observations of N44 were made. The *ASCA* data showed that the hot gas in the breakout region is slightly cooler than that in the SB interior (Magnier et al. 1996). *ROSAT* observations of the HII complex N11 were analyzed to study the interaction between OB associations, HII regions, and SBs (**?**). In the latest study, Dunne et al. (2001) analyzed *ROSAT* observations of eleven Hα-identified SBs in the LMC.

In this study, the derived X-ray luminosities of the SB were compared with the pressure-driven bubble model of Weaver et al. (1977). Assuming that the shell thickness is small compared to the radius of the bubble, that the electron temperature in the shell is $T_{\rm e} \sim 10^4$ K, and that the mean atomic mass of the ambient medium $\mu_{\rm a} = (14/11)\ m_{\rm H}$, the X-ray luminosity can be derived from the equations 6.56 - 6.59 as follows:

$$L_{\rm X} \simeq (6.7 \times 10^{29}\ {\rm ergs\ s^{-1}})\ {\rm EM}^{5/7} \xi I R_{\rm pc}^{12/7} v_{\rm exp}^{1/7}, \tag{6.60}$$

where the $v_{\rm exp}$ is the expansion velocity in km s^{-1}. They used the $v_{\rm exp}$ from the Hα broad line spectra, EM from the continuum-subtracted Hα images. The predicted X-ray luminosities range from $10^{34.3}$ to $10^{35.1}$ ergs s^{-1}. These luminosities range from $\sim$3 to $\sim$50 times lower than the X-ray luminosities determined from

Table 6.1: Best-Fit LMC SB X-Ray Spectral Fits.

Object	log $N_{\rm H}$ ($\rm cm^{-2}$)	kT (keV)	log $L_{\rm X}$† (ergs $\rm s^{-1}$)	$N_{\rm e}\sqrt{f}$ (10^{-2} $\rm cm^{-3}$)
N11 shell 1...	21.9	0.13	37.17	31.
N44...	20.6	0.71	35.73	3.8
N51 DEM L 192...	20.4	0.28	35.18	1.5
N51 DEM L 205...	20.5	0.25	34.86	3.7
N57...	20.6	0.33	35.32	1.8
N103B...	21.3	0.72	34.85	0.8
N105...	21.6	0.31	35.40	4.6
N144...	20.5	0.32	34.74	1.3
N154...	20.7	0.29	35.52	1.8
N158...	20.7	0.60	35.85	3.0
N160...	20.9	3.40	35.80	1.9
N206...	20.7	0.31	35.09	2.2
30 Dor C East...	21.1	1.19	35.49	4.0
30 Dor C est...	22.0	1.22	35.84	7.4

†: In the energy band of 0.5 - 2.4 keV.

the *ROSAT* data. This suggests that the majority of the X-rays are produced by mechanisms different than those described in the pressure-driven bubble model, confirming that the SBs in their sample are X-ray bright. They also compared the SB volume, Hα luminosity, expansion velocity, and and bright star count (based on the OB association star counts in Lucke & Hodge (1970)) with the X-ray luminosity. The most significant positive correlation was found between the X-ray luminosity and bright star count, although the moderate positive correlation could be seen also in other parameters. This correlation demonstrate that the X-ray luminosity of a SB is affected by the richness and age of OB associations within its shell walls.

Recently the some observations of SBs with *Chandra* and *XMM-Newton* have been done. The X-ray bright SBs in the LMC, N51D, and N11 were observed with *XMM-Newton* (Nazé et al. 2004). In addition to the X-ray emission from massive stars, possible hidden SNRs, colliding-wind binaries, numerous pre-main sequence stars of some dense clusters inside the SB, they found that the SB may be leaking some hot gas in the ISM. Cooper et al. (2004) observed the N51D, which is one of the X-ray brightest SBs in the LMC and from which the emission line features in the X-ray spectra suggest an overabundance in oxygen and neon which is used argue for the occurrence of SN explosion (Bomans et al. 2003). The X-ray spectrum of the diffuse emission from N51D requires a power-law component to explain the

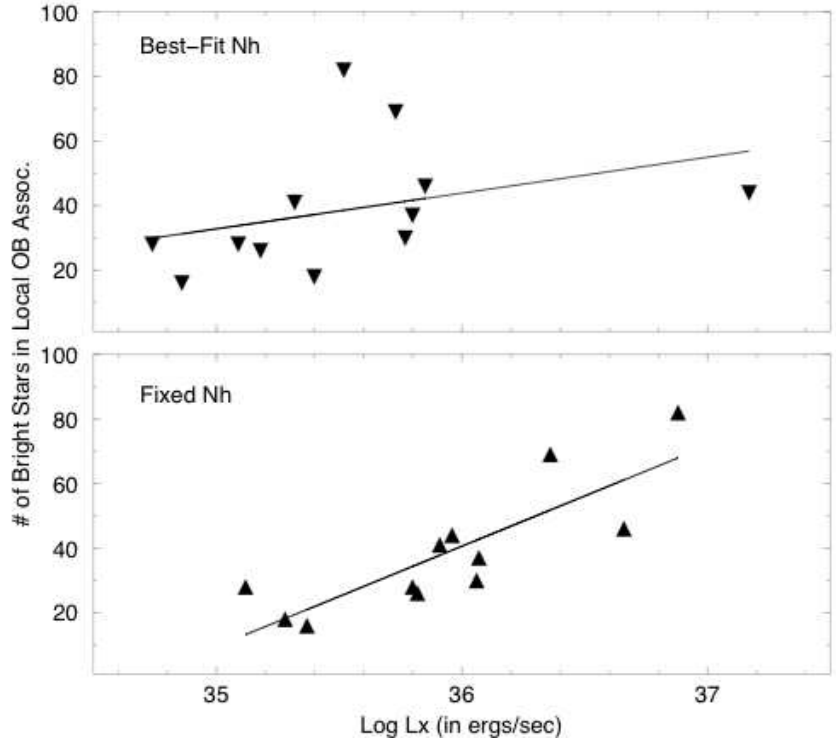

Figure 6.5: SB X-ray luminosity vs. bright star count for the best-fit $N_{\rm H}$ X-ray spectral fits (top) and fixed $N_{\rm H}$ X-ray spectral fits (bottom). Luminosity is plotted on a logarithmic scale. Bright star counts are based on the star counts in local OB associations (Lucke & Hodge 1970).

featureless emission at 1.0 - 3.0 keV. The origin of this power-law component is unclear, but it may be responsible for the discrepancy between the stellar energy input and the observed interstellar energy in N51D.

Chapter 7

Observations and Results

Here we describe the results on the analyses of SBs and/or SB formation sites.

7.1 30 Dor C

First we describe the X-rays observation of the SB 30 Dor C in the LMC. As we mentioned in section 6.2.5, the LMC provides a sample of numerous SBs at a common distance that is resolvable by modern X-ray detectors. For this study, we singled out 30 Dor C as being the best target for our research. A radio source was discovered by Le Marne (1968) southwest of 30 Dor and was named 30 Dor C, which is now categorized as an SB. Mills et al. (1984) found a shell-like structure in the 843 MHz band observation with a radius of about $3'$ (40 pc on 50 kpc distance). Along the radio shell, complex Hα, Hβ, and [S II] emissions were found, which are bright in the southeast but dim in the other side (Mathewson et al. 1985). In the X-ray band, *Einstein* Observatory detected the eastern shell of the 30 Dor region for the first time (Long et al. 1981; Chu & Mac Low 1990). Dunne et al. (2001) reported that the *ROSAT* spectrum required a thermal model with a rather high temperature (1 keV). Itoh et al. (2001) found non-thermal X-rays in the *ASCA* data but could not spatially resolve the thermal and non-thermal components in the SB. Recently, Dennerl et al. (2001) found a complete ring in soft and hard X-rays with a diameter of $6'$ with *XMM-Newton*. The hard X-rays from the shell resemble the synchrotron X-rays in the shock front of SNRs, which is a site of cosmic-ray acceleration. Therefore, 30 Dor C would be the first and best candidate of cosmic-ray accelerating SBs.

Chandra observed SN 1987A several times with the ACIS-S array. Some of the SN 1987A observations covered the 30 Dor C region by chance, which is located at about $5'$ northeast from SN 1987A. In order to study the diffuse structure of 30 Dor C, we selected two observations in which the grating instrument is removed from the X-ray mirror axis (observation IDs [Obs. IDs] 1044 and 1967; hereafter Obs. 1 and 2). The observed dates and targeted positions are given in table 7.1. Data acquisition from the ACIS was made in the timed-exposure faint mode with a readout time of 3.24 s in both observations. The data reductions and analyses were made using the *Chandra* Interactive Analysis of Observations (CIAO) software, version

2.3. For level-1 processed events provided by a pipeline processing at the *Chandra* X-Ray Center, we made a charge transfer inefficiency correction and selected *ASCA* grades 0, 2, 3, 4, and 6 as the X-ray events. High-energy events due to charged particles and hot and flickering pixels were removed. There are some "streaks" in the CCD chip S4, which are caused by a random deposition of a significant amount of charges in pixels along the row during the serial readout process. These "streak" events were removed by using the program *destreak* in CIAO. The total available times for each observation, after the screening, are listed in table 7.1.

Table 7.1: Observation Log around 30 Dor C

Obs.	Satellite	Obs. ID	R.A. (J2000.0)	Decl. (J2000.0)	Date	Exposure (ks)
1...	*Chandra*	1044	05 32 22.0	-69 16 33.0	2001 Apr 25	18
2...	*Chandra*	1967	05 32 22.0	-69 16 33.0	2000 Dec 07	99
3...	*XMM-Newton*	0104660301	05 35 28.0	-69 16 11.0	2000 Nov 25	21
4...	*XMM-Newton*	0113020201	05 37 47.6	-69 10 20.0	2001 Nov 19	16

Note.—Units of right ascension are hours, minutes, and seconds, and units of declination are degrees, arcminutes, and arcseconds.

XMM-Newton also observed SN 1987A and the 30 Dor region several times. We selected two observations (Obs. IDs 0104660301 and 0113020201, hereafter Obs. 3 and 4), which cover 30 Dor C and are relatively free from high background flares because of low-energy protons. The observed dates and targeted positions are shown in table 7.1. In both observations, only the MOS CCDs were operated in the full-frame mode with the medium filter (Stephan et al. 1996; Villa et al. 1998) for blocking ultraviolet photons. The data reductions and analyses were made using the *XMM-Newton* Standard Analysis System (SAS; Watson et al. 2001) version 5.4.1; we performed the basic pipeline process following the SAS guide. The background level was changed significantly, particularly in Obs. 4. Hence, we removed the data with a high background level (>0.6 counts s^{-1} in the 10.0 - 15.0 keV band). The exposure times in each observation after the screenings are listed in table 7.1.

Figure 7.1 shows the soft (0.7 - 2.0 keV) and hard (2.0 - 7.0 keV) band *Chandra* images around 30 Dor C, in which the two observations (Obs. 1 and 2) are combined with a correction of the exposure times. A clear shell-like structure with a radius of $\sim 170''$ (R $\sim$ 40 pc radius at the 50 kpc distance) is seen in both bands. In detail, however, the morphologies differ from each other; the entire shell is seen in the soft band, whereas the hard X-rays are visible only at the western part. Cataloged SNRs, the Honeycomb nebula (SNR 0536–69.3), and SN 1987A are also seen mainly in the soft band (see figure 7.1). The X-ray features of these objects have been reported with *XMM-Newton* (Dennerl et al. 2001) and *Chandra* (Burrows et al. 2000; Park et al. 2002; Michael et al. 2002) monitoring observations.

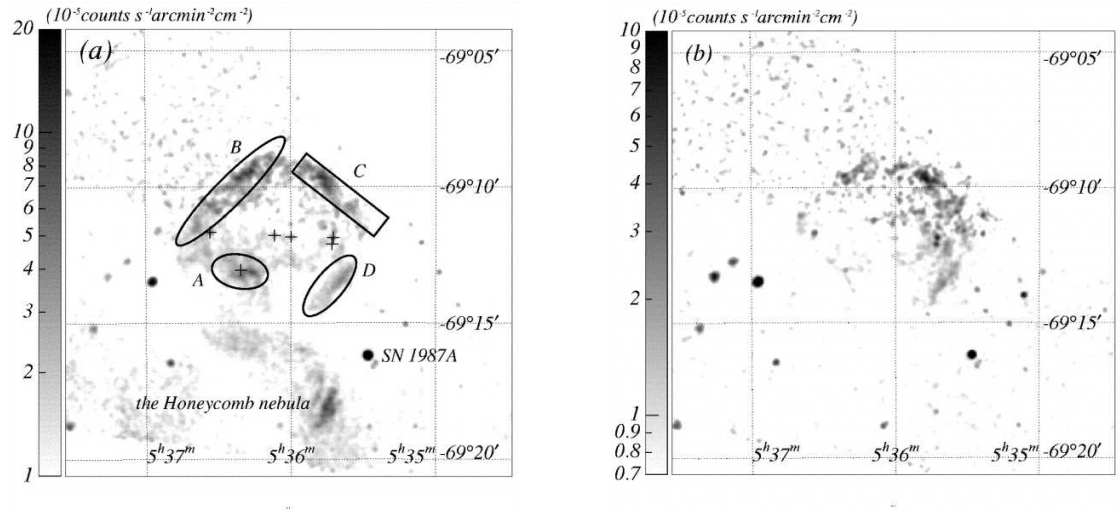

Figure 7.1: *Chandra* ACIS images around 30 Dor C in the (a) 0.7 - 2.0 keV band and (b) 2.0 - 7.0 keV band, with J2000.0 coordinates. The scales are logarithmic, with units of $\times 10^{-5}$ counts s^{-1} $arcmin^{-2}$ cm^{-2}, as shown in the left bar for each image. The source regions used for the spectral analyses are shown by the solid lines in the left panel (figure 7.2, tables 7.3 and 7.4). The plus signs represent the position of the detected point sources shown in table 7.2. The position of SN 1987A (Burrows et al. 2000; Park et al. 2002; Michael et al. 2002) and the Honeycomb nebula (Dennerl et al. 2001) are also shown.

In addition to the diffuse structure, some pointlike sources are found inside 30 Dor C. The exposure times of the *XMM-Newton* observations are short, most of the data suffer from a high background, and the spatial resolution is not sufficient. Hence, we concentrated on the *Chandra* data for the point-source search and analysis. At first, point sources were searched for with the *wavdetect* software in the 0.5 - 8.0 keV band images, then manually inspected for any spurious pointlike structure due mainly to a part of the diffuse emission. We thus found six point sources with a significance level of greater than 7.0 σ, as shown in figure 7.1 and table 7.2. For these six point sources, we searched for optical, infrared, and radio counterparts and found that three (sources 1, 3, and 4) coincide at the positions of the brightest star clusters: α, β, and γ (Lortet & Testor 1984). We therefore checked further for any X-ray emission from the other clusters (δ, ϵ, and ζ), which are also members of the OB association LH 90 (Haberl & Pietsch 1999; Sasaki et al. 2000) but found no candidate.

In the *Chandra* observations, we can see that the diffuse structure consists of several shell fragments (see figure 7.1), and the whole structure is widely spread over the two observed regions with different configurations of the CCD types (BI and FI). Therefore, a spectral analysis on all of the diffuse structure is technically and scientifically complicated. For this reason, we divided the diffuse structure into four regions (hereafter shells A - D), as shown in figure 7.1), and performed the spectral analysis separately for each shell. We excluded all of the detected point sources (see 7.1) from each shell. The background regions were also selected separately for each

Table 7.2: Point Source Data around 30 Dor C

Num.	CXO J05	SM[a]	Γ/kT[b] /(keV)	N[b,c] ($\times 10^{22}$ Hcm^{-2})	Flux[d] (ergs cm^{-2} s^{-1})	χ^2/d.o.f.
1...	3542.4-691152	MK	2.1 (1.4 - 3.6)	3.5 (2.5 - 5.1)	1.8 $\times 10^{-14}$	9.53/12
2...	3542.9-691206	PL	2.1 (1.4 - 3.2)	7.7 (4.4 - 13)	2.0 $\times 10^{-14}$	8.25/13
3...	3559.9-691150	PL	1.7 (1.3 - 2.6)	0.13 (<1.3)	6.5 $\times 10^{-15}$	4.03/7
4...	3606.6-691147	MK	1.0 (0.19 - 1.3)	0 (<1.9)	2.8 $\times 10^{-15}$	8.64/9
5...	3620.7-691303	PL	1.9 (1.5 - 2.4)	0 (<0.22)	8.9 $\times 10^{-15}$	19.8/20
6...	3633.3-691140	PL	1.8 (1.5 - 2.3)	0.5 (0.08 - 1.1)	2.0 $\times 10^{-14}$	21.4/18

Notes.—Sources 1, 3, and 4 have the optical counterparts, the stellar clusters α, β, and γ, respectively (Lortet & Testor 1984).
a: Spectral model. PL: power law, MK: thin-thermal plasma in collisional equilibrium (Mewe et al. 1985; Kaastra 1992), with abundance of 0.3 solar.
b: Parentheses indicate single-parameter 90% confidence regions.
c: Absorption column in the LMC. The abundance is assumed to be the average LMC values (Russel & Dopita 1992; Hughes et al. 1998).
d: Absorbed flux in the 0.5 - 9.0 keV band. (Feast 1999).

shell from the source-free regions in the same CCD and observations as those of the shells.

The *XMM-Newton* fields covered the whole diffuse structure. However, for consistency with the *Chandra* analysis, we divided the diffuse structure into shells A - D, the same as in the *Chandra* case. The background regions were selected from the source-free regions in the same observation. The spectra of each shell taken from all the available observations with *Chandra* and *XMM-Newton* were analyzed simultaneously. However, for brevity, we show only the *Chandra* spectra (background-subtracted) and the fitting results in figure 7.2.

For spectral analyses, we used *XSPEC*, version 11.00 (Arnaud 1996). The spectrum of shell A shows many line-like structures with the center energies at 0.58, 0.68, 0.92, and 1.35 keV, which correspond to the emission lines of He-like O Kα and Kβ, He-like Ne, and He-like Mg, respectively. We therefore fitted the spectrum with a thin thermal plasma model in non-equilibrium ionization (NEI; Borkowski et al. 2001a) with the mean LMC abundances (Russel & Dopita 1992; Hughes et al. 1998). The interstellar absorption in our Galaxy and LMC were treated separately. The Galactic absorption column was estimated using the H I data by Dickey & Lockman (1990) as $N = 6.35 \times 10^{20}$ cm^{-2}. Arabadjis & Bregman (1999) reported that the value of $N_{\rm H}$, measured in the X-ray band, is twice that of N in the case of $|b| > 25^\circ$ and $N > 5 \times 10^{20}$ cm^{-2}. Therefore, we fixed the galactic absorption column to be $N_{\rm H} = 1.27 \times 10^{21}$ cm^{-2}; we used the cross sections of Morrison & McCammon (1983) and the solar abundances of Anders & Grevesse (1989). The absorption column in

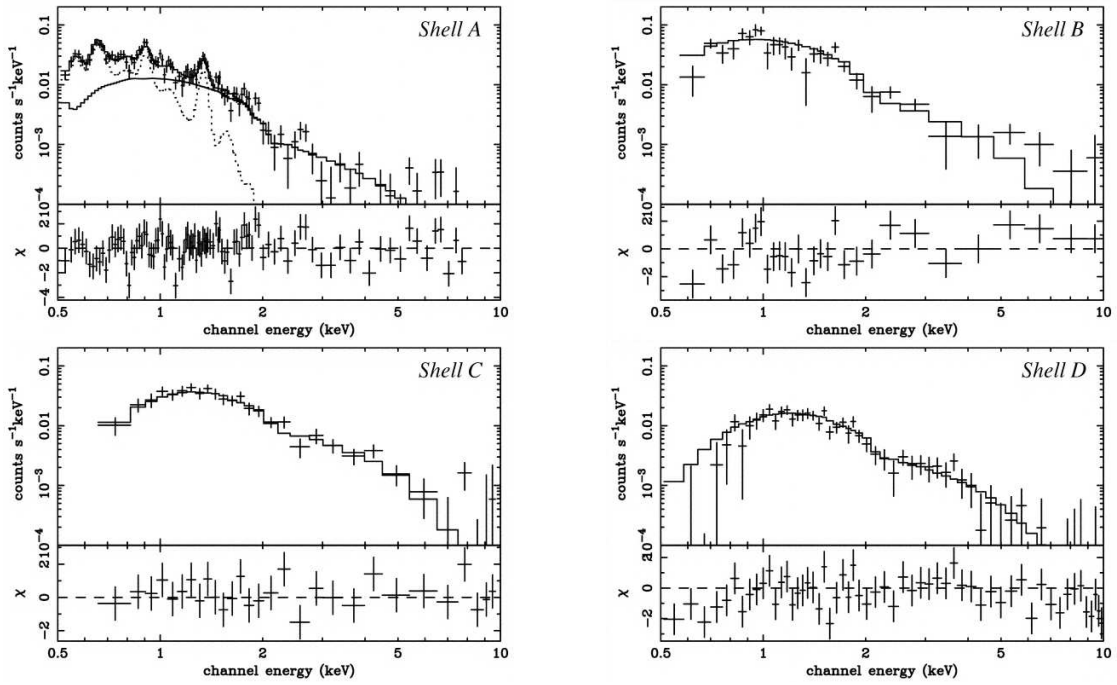

Figure 7.2: (Upper panels:) Background-subtracted spectra for shells A - D (plus signs). Although the spectral fittings were made with both the *Chandra* and *XMM-Newton* data simultaneously, only the *Chandra* data and results are shown for brevity. The best-fit models are shown with solid (power-law) and dotted (NEI) lines. (Lower panels:) Data residuals from the best-fit models.

the LMC was, on the other hand, treated as a free parameter with the mean LMC abundance (Russel & Dopita 1992; Hughes et al. 1998).

This thin-thermal plasma model was rejected with a χ^2/degrees of freedom (d.o.f.) $= 331.8/211$, even if we allow the abundances to be free, leaving a systematic data residual at the high-energy band. We hence added a power-law component on the thin-thermal model. Since the two-component model still leaves large residuals at about 0.8 and 1.3 keV, we allowed the abundance of Fe and Mg in the thermal plasma ("NEI" component) to be free. The fitting was then greatly improved with a χ^2/d.o.f $= 264.6/209$. Although this two-component model is still rejected in a statistical point of view, further fine-tuning on the model is beyond the scope of this paper. Figure 7.2 and table 7.3 show the best-fit models and parameters, respectively.

Table 7.3: Best-Fit Parameters of Shell A

Parameters	NEI	Power Law
kT/Γ (keV/M)...	0.21 (0.19 - 0.23)	2.9 (2.7 - 3.1)
$n_e t_p^a$ (10^{12} cm^{-3} s)...	9.9 (>1.4)	...
EM^b (10^{58} cm^{-3})...	2.6 (2.1 - 2.8)	...
[Mg/H]^c...	3.3 (2.5 - 4.0)	...
[Fe/H]^c...	0.10 (0.06 - 0.14)	...
Flux^d (ergs cm^{-2} s^{-1})...	6.8×10^{-14}	8.4×10^{-14}
$N_{\rm H}^{{\rm LMC}e}$ ($\times 10^{22}$ cm^{-2})...	0.24 (0.21 - 0.28)	...^{f}

Notes.—Parentheses indicate single-parameter 90% confidence regions.
a: Ionization timescale, where ne and tp are the electron density and age of the plasma.
b: Emission measure EM $= \int n_e n_p dV \simeq n_e^2 V$ where n_p and V are the proton density and the plasma volume, respectively. The distance to LMC is assumed to be 50 kpc.
c: Abundance ratio relative to the solar value (Anders & Grevesse 1989).
d: Absorbed flux in the 0.5 - 9.0 keV band.
e: Absorption column in the LMC. The abundances are assumed to be the average LMC values (Russel & Dopita 1992; Hughes et al. 1998).
f: Fixed to the same value as that for the NEI component.

Unlike shell A, the X-ray spectra of shells B - D are hard and featureless, suggesting a non-thermal origin. In fact, a thin-thermal model fitting requires an unrealistically high temperature (>2 keV) and low abundances ($z < 0.3$). We therefore fitted the spectra with a power-law model with absorption, which was calculated in the same way as that for shell A, and found acceptable fits for all of the spectra. The best-fit models and parameters are shown in figure 7.2 and table 7.4, respectively.

It is conceivable that the spectra of shells B - D may include a small fraction of the thin-thermal component found in shell A. We therefore added the same thin-thermal spectrum as that for shell A and fitted them with this composite model (thin-thermal plus power-law). The free parameters are normalizations of the two

Table 7.4: Best-Fit Parameters of Shell B - D

Parameter	Shell		
	B	C	D
Power Law			
Photon index	2.7 (2.5 - 2.9)	2.3 (2.1 - 2.4)	2.5 (2.3 - 2.7)
Flux[a] (ergs s^{-1} cm^{-2})	4.7×10^{-13}	4.5×10^{-13}	1.5×10^{-13}
N_H^{LMC}[b] (10^{22} cm^{-2})	0.10 (0.06 - 0.19)	1.1 (0.94 - 1.4)	1.0 (0.85 - 1.3)
χ^2/d.o.f.	193.0/138	68.3/84	121.5/110
SRCUT ($\alpha = 0.5$)			
$\nu_{rolloff}$ (10^{16} Hz)	6.2 (4.1 - 7.9)	24 (15 - 47)	12 (6.4 - 23)
Flux density at 1 GHz (10^{-2} Jy)	1.9 (1.5 - 3.0)	0.71 (0.67 - 0.75)	0.42 (0.25 - 0.83)
N_H^{LMC} (10^{22} cm^{-2})	(<0.04)	1.0 (0.90 - 1.1)	0.89 (0.75 - 1.0)
χ^2/d.o.f.	195.5/138	67.0/84	120.2/110
SRCUT ($\alpha = 0.6$)			
$\nu_{rolloff}$ (10^{16} Hz)	8.0 (5.3 - 11)	36 (20 - 75)	16 (8.3 - 35)
Flux density at 1 GHz (10^{-2} Jy)	11 (8.2 - 16)	4.1 (3.9 - 4.3)	2.5 (1.6 - 4.6)
N_H^{LMC} (1022 cm^{-2})	(<0.01)	1.0 (0.91 - 1.2)	1.1 (1.0 - 1.3)
χ^2/d.o.f.	195.2/138	67.1/84	121.8/110

Note.—Parentheses indicate single-parameter 90% confidence regions.
a: Flux in the 0.5 - 9.0 keV band.
b: Absorption column in the LMC. The abundances are assumed to be the average LMC values (Russel & Dopita 1992; Hughes et al. 1998).

components: the power-law index and N_H value. However, no significant fraction of the thin-thermal component is found from shells B - D.

For all of the point sources, the X-ray photons are collected from an ellipse with the radii of the PSF, as listed in table 7.2. We note that all of the sources are located far from the on-axis position of the X-ray mirror, and hence the PSFs are larger than the best value of the *Chandra* PSF ($\sim 0.5''$ on the aim point). The background regions were selected from source-free regions in the same way as the diffuse emissions. We first fitted the spectra with a thin-thermal plasma model in collisional equilibrium (MEKAL; Mewe et al. 1985; Kaastra 1992) with an absorption calculated in the same way as diffuse emission. The abundances are fixed to be 0.3 solar, the average value of the interstellar medium in the LMC. The fittings are acceptable for two sources (1 and 4) with reasonable temperature (2.1 and 1.0 keV), but for the spectra of the other four sources, the models are

either rejected or require an unreasonably high temperature. We therefore fitted the spectra of these sources with a power-law model. The best-fit parameters and the reduced χ^2 are listed in table 7.2.

The absorption columns of the northeastern shells (shells A and B) are similar to those of most sources in the LMC ($\sim 10^{21}$ cm^{-2}), whereas those of the other shells (C and D) are significantly larger ($\sim 10^{22}$ cm^{-2}) than the typical LMC absorption. A similar trend was found for the point sources; those in the western half, sources 1 and 2, have a larger $N_{\rm H}$ ($\sim 10^{22}$ cm^{-2}) than those in the eastern half, sources 3 - 6 ($\leq 10^{21}$ cm^{-2}). Since Dunne et al. (2001) have already reported this tendency, we have thus confirmed the results with the better spatial and spectral capability of *Chandra*. This systematic increase of absorption toward the western region of 30 Dor C may be due to extra absorption of a molecular cloud located in front of the western half of 30 Dor C. To verify our conjecture, we searched for the molecular cloud in the CO map (Yamaguchi et al. 2001, uppermost panel of figure 7.2) and found a candidate with intensity of $I({\rm CO}) \sim 3.6$ K km s^{-1}. With a conversion factor of $N({\rm H_2})/I({\rm CO}) \sim 9 \times 10^{20}$ cm^{-2}(K km s^{-1})$^{-1}$ (Fukui et al. 1999), the estimated absorption column due to the molecular cloud is $N_{\rm H}^{\rm MC} \sim 6.5 \times 10^{21}$ cm^{-2}, which is consistent with our result.

7.2 N44 (DEM L 152)

N44 is a bright H II complex containing an 44 pc$\times$67 pc SB cataloged as DEM L 152 around the OB association LH 47. The Hα shell is well detected with well-defined shell walls as shown in figure 7.3. A variety of Hα-bright structures are seen in N44, and identifications of the components, both bright knots and large filamentary arcs, have been made by Henize (1956) with labels N44 A - N Davies et al. (1976) and with labels DEM L 140 - 170. The radio emission from the ring of N44 is thermal (Mathewson & Clarke 1973), and the expansion velocity within the ring is 30 km s^{-1} (Georgelin et al. 1983).

At the southwest corner, coinciding with a bright shell-like H II region in which high-velocity material moving at –120 km s^{-1} with respect to the main component has been detected (Goudis & Meaburn 1984). The expansion patterns of the main shell and the large shell to the east are studied by Meaburn & Laspias (1991). The main shell was modeled as SB using energy input implied by the observed massive stellar component. It is shown that the expansion velocity of the main shell is much higher than expected (Oey & Massey 1995). This discrepancy may due to the significant energy/pressure lost by the blowout shown at the southwest of the SB. Another important result they reported is that the stellar component interior to the shell is generally older than the population immediately exterior to the shell ($\sim$ 10 Myr vs. $<$5 Myr), suggestive of sequential star formation.

Because the shell is one of the brightest SB in the LMC in the soft X-ray band (see table 6.1) and then has been observed with many instruments. Diffuse X-ray emission from various portions of the N44 region was detected by the *Einstein* Observatory (Chu & Mac Low 1990; Wang & Helfand 1991). Chu et al. (1993)

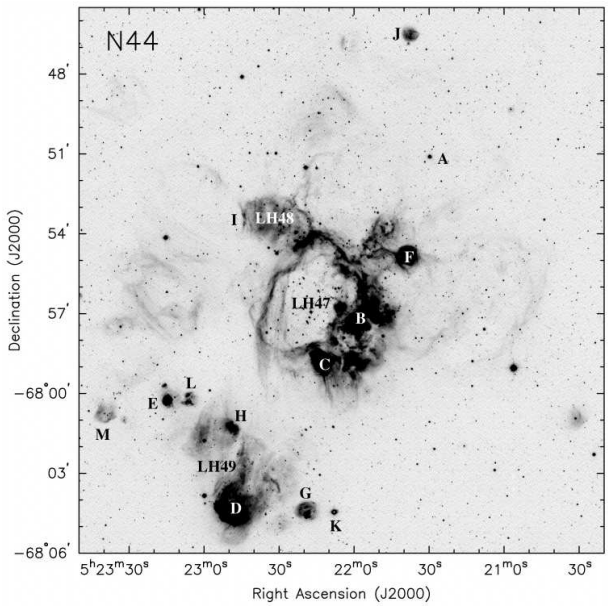

Figure 7.3: Hα image of N44, showing the nebular components defined by Henize (1956) and the OB associations cataloged by Lucke & Hodge (1970). This figure is adopted from Nazé et al. (2002).

reported a breakout region on the southern edge of the SB and an X-ray blister on the eastern edge of the shell are detected in the *ROSAT* image as well. The high temperature plasma indicated by the *ROSAT* results stimulates us to search non-thermal X-ray emission as well as 30 Dor C.

N44 was observed with EPIC onboard *XMM-Newton* on the 2004 December 4 - 5 (Obs. ID 0205740101). The original exposure time was ∼50 ks. The telescope optical axis position on the EPIC was R.A. = $05^{\rm h}22^{\rm m}20\overset{\rm s}{.}00$, Decl.= $-67°56'40\overset{''}{.}0$ (J2000). Thanks to the large FOV ($30'$ of diameter), the whole region of N44 including nearby SNR was covered. We used the Observation Data Files (ODF) data provided by the *XMM-Newton* Science Operations Centre. For the data reduction, we used *emchain* and *epchain* in the analysis software SAS version 6.5.0 with the bad pixel finding algorithm on. Then we cut the events in the duration of background flare with the following way. First, we made light curves of the Pattern 0 (single pixel) events in the energy band of 10 - 15 keV with the 100 sec binning and made histogram of the count rate. Then we fit the distribution of count rate with gauss function and cut the noisy duration in which the count rate is higher with 2 σ significance than the gaussian peak. Second, we did the same cutting but using the events detected in the region of $>12'$ from the center of FOV in the energy band of 1.0 - 5.0 keV and Pattern <12 for MOS and <4 for pn chip. Then, the effective exposure times were ∼23 ks for MOS and ∼17 ks for pn chip. Hereafter, we used those events that has Pattern < 12 for MOS, <4 for pn chip in order to eliminate the events due to charged particles and hot and flickering pixels.

Figure 7.4 shows soft (0.2 - 2.0 keV) and hard (2.0 - 7.0 keV) band X-ray image of

N44. As shown in the past X-ray observations, the distribution of the X-ray emission has clear correlation with that of Hα (Magnier et al. 1996). In the soft band, there is an almost uniform X-ray emission from entire region of main shell, some blowout regions, and the nearby SNR 0523–67.9. However in the hard band, there seems to be almost no significant diffuse emission in the main shell and blowout regions. This feature is obviously different from that was seen in 30 Dor C (Bamba et al. 2004).

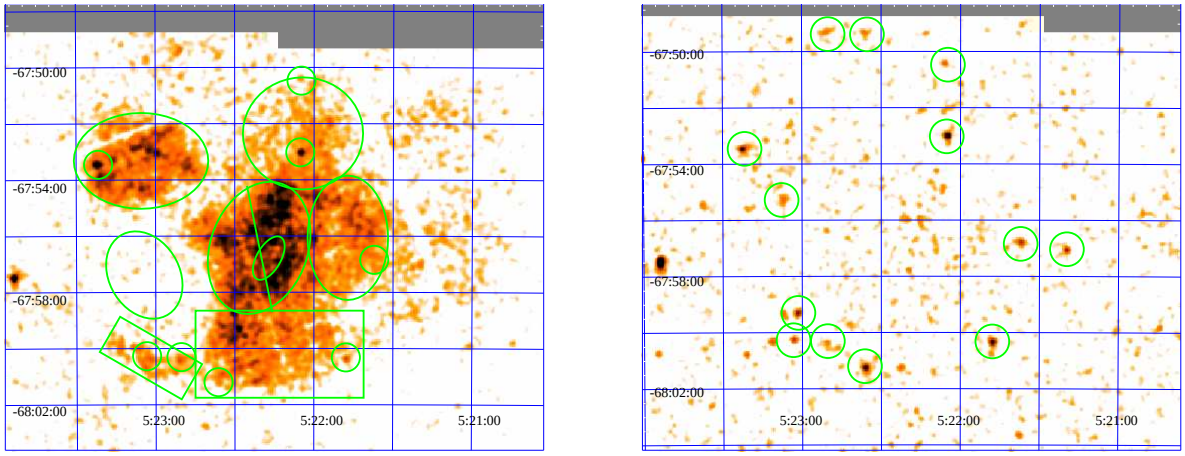

Figure 7.4: Soft (left panel; 0.2 - 2.0 keV) and hard (right panel; 2.0 - 7.0 keV) band X-ray image of the N44 region. The regions from which we extracted photons are shown in the soft band image. The main shell are divided into northwest and southeast regions. Hereafter we concentrate our study on the main shell. In the hard band image we show the point sources detected in the band.

We conducted the point source search with *eboxdetect* and *emldetect* command in SAS 6.5.0 in the soft (0.2 - 2.0 keV) and hard (2.0 - 7.0 keV) energy band. The detection minimum likelihood was 6 for *eboxdetect* and 10 for *emldetect*. While we did not detect any plausible point source in the soft band, we detected 13 sources from the surrounding region of the main shell (7.4) in the hard band. However, we could not detect any point source from the OB association in the vicinity of main shell (LH 47 and LH48). Since the HEW of the XRT is $\sim 15''$ (see section 2.2.1), the mean distance between the closest neighbours in the typical OB association ($R_{\rm dis} \simeq 6$ pc $\simeq 27''$ at the distance of 50 kpc) can be resolved. Our result indicates that the luminosities of the members in LH 47 and LH 48 is not so high that they are detected as point sources.

Figure 7.5 shows the spectrum of MOS 1 and 2 chip extracted from the entire main shell region (the left panel in figure 7.4). For the brevity to see the spectra, we only show the spectra of EPIC MOS detectors and hide that of pn detector, although we used all of them in the fitting. As in the case of 30 Dor C, some emission lines from He-like O Kα and Kβ, He-like Ne, and He-like Mg. The instrumental background component (Neutral Al line; 1486 eV) is also seen. Hence we tested thin-thermal plasma model in NEI with the mean LMC abundance and composite (thermal and non-thermal) plasma model in the spectral fit. We fixed the galactic absorption column to be $N_{\rm H} = 1.27 \times 10^{21}$ cm^{-2} (see section 7.1). In the case of the latter

model, fit result was statistically rejected while the thin-thermal model was accepted with a χ^2/d.o.f. = 188.24/153. The fitting parameters are shown in table 7.5.

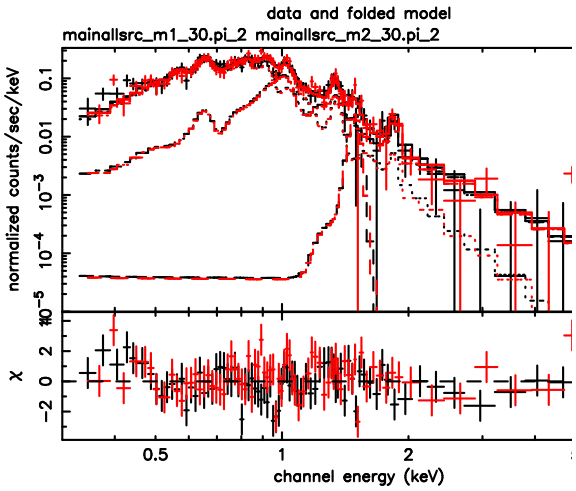

Figure 7.5: Background-subtracted spectrum extracted from entire main shell region. We fit this spectrum with thin thermal plasma model with two temperature. Al fluorescence line is also considered.

We then further divide main shell into three regions: northwest, southeast, and the region around LH 47 (figure 7.4). The energy spectra from formers are shown in figure 7.6 and their fitting parameters are presented in table 7.5. Northwest region shows the high temperature feature seen in figure 7.5 and significantly low ionization parameter than southeast region.

The plasma temperature seen in the northwest region is exceedingly high compared with other SBs (Nazé et al. 2004; Cooper et al. 2004). This feature suggests that N44 is the most active, that is, experienced the latest SN among these SBs.

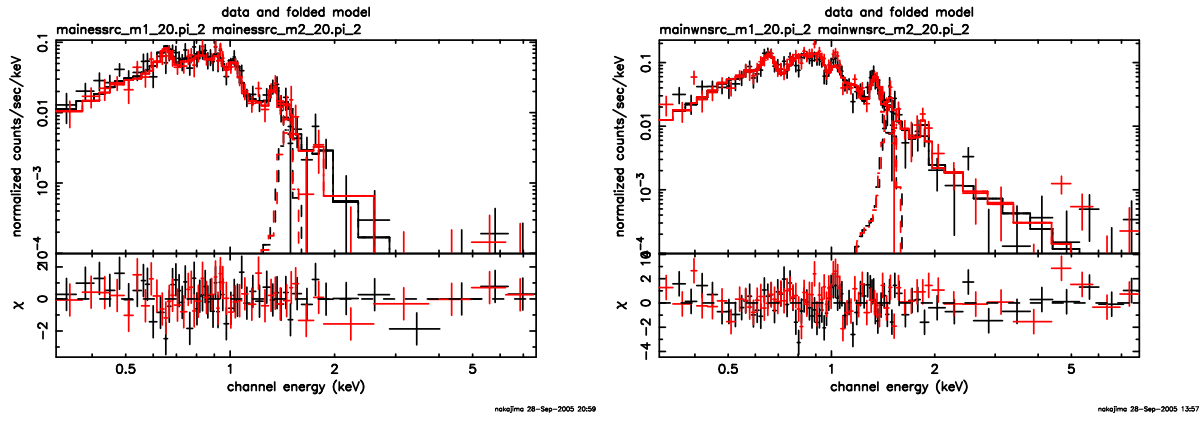

Figure 7.6: Background-subtracted spectrum extracted from northwest and southeast region of main shell (left and right panel, respectively). Al fluorescence line is also considered.

Oey & Massey (1995) and Will et al. (1997) have observed OB associations LH 47, which is located inside the main shell and its surrounding regions with

Table 7.5: Fitting parameters for each region.

Region	$N_{\rm H}$	kT	τ	flux[a]	χ^2/d.o.f.
	($\times 10^{21}$Hcm^{-2})	(keV)	($\times 10^{10}$ s cm^{-3})		
Entire Main Shell					
($kT_{\rm low}$ component)	2.92 (2.42–3.46)	0.6(0.4–0.8)	2.5 (1.9–3.8)	3.51	188/153
($kT_{\rm high}$ component)	–	2.2(1.5–2.5)	5.3 (4.6–7.0)	–	–
North-West	2.40 (1.51–3.03)	1.8 (1.7–1.9)	1.4 (1.1–1.7)	1.30	180/139
South-East	1.00 (0.73–1.19)	0.40 (0.39–0.43)	91 (68–240)	0.35	72/95
Vicinity of OB-stars	1.81 (<2.20)	0.40 (0.32–0.64)	820 (48–5000)	0.12	22/20

Note.—Parentheses indicate single-parameter 90% confidence regions.
a: Absorption corrected flux in the 0.5 - 7.0 keV band ($\times 10^{-12}$ ergs cm^{-2} s^{-1}).

optical light. Oey & Massey (1995) investigated spectroscopic data of the 62 bluest stars ($> 10\ M_\odot$)in the LH 47/48, and derived the spectral types of 54 stars in LH 47. Will et al. (1997) also took spectra of V band brightest 14 stars and got almost consistent spectral types of them. On the whole, OB-type stars are concentrated at center of main shell.

Hence we defined the regions from which we extract the photons in figure 7.4 and got the spectrum shown in figure 7.7 and fitting parameters presented in table 7.5. Furthermore in the case of this region, we set the abundance of O, Ne, and Mg to be free. Then we got the abundance of 0.46 (>0.10), 1.15 (>0.26), 0.91 (>0.21), respectively.

7.3 Sgr C

Sgr C region, the complex of the massive molecular clouds and hence the promising candidate for the clustering of massive stars and SNe. It is located at $\sim 34'$ southwestward from the GC, near the base of one of the two large radio continuum arcs and many other bright non-thermal filaments (NTFs) as shown in figure 7.8. The neutral and ionized gas distribute hard against not only the H II region but the bright portion of Sgr C's NTF (Liszt & Spiker 1995).

The spectra of $J = 1 - 0$ ^{13}CO emission near Sgr C show the terrifically complex distribution around Sgr C. Hence it is very easy to make false physical associations based on random spatial coincidence. However, most possibly associated component which we should pay attention is at the recombination-line velocity of Sgr C ($\sim$65.5 km s^{-1}). The sum of all the emission integrated over the range (-84 km s$^{-1} < v < -24$ km s^{-1}) shows a cavity or cleft. The Sgr C shell-like H II region sits within the cavity of the associated molecular gas. The origin of this cavity

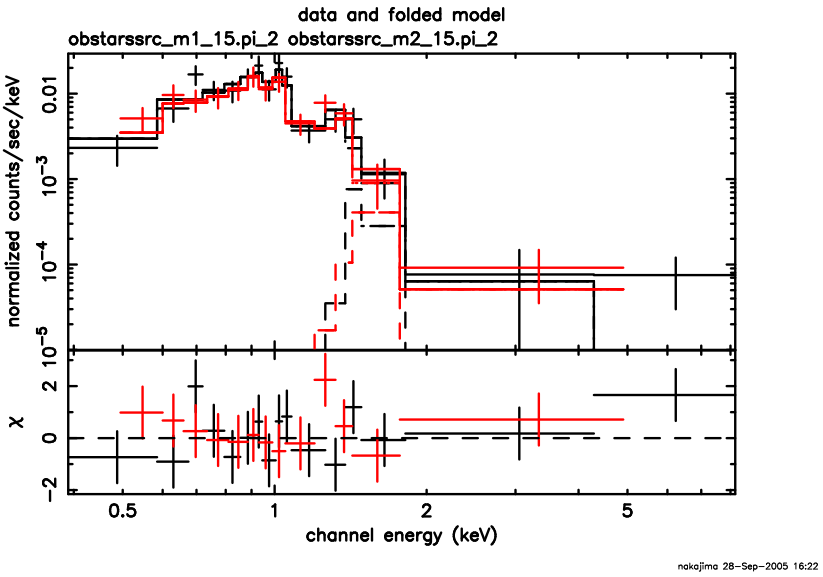

Figure 7.7: Background-subtracted spectrum extracted from vicinity of OB-type stars association LH 47. Al fluorescence line is also considered.

must be the energetics of the H II region, which is dominated by two influences. One is the thermal pressure maintained by photoionization, and the other is the strong stellar winds expected from early O-type stars (Abbott 1982) which was inferred by Odenwald & Fazio (1984). The mass of the main body of this cavity gas below Sgr C (M359.5–0.15 in Liszt & Spiker 1995), calculated by assuming that ^{13}CO is 20% as bright as ^{12}CO, taking a CO-H_2 conversion of 3×10^{20} H_2 cm^{-2} (K km s^{-1})$^{-1}$ is $6.1\times10^5 M_\odot$.

In the X-ray band, Murakami et al. (2001) discovered the strong 6.4 keV line emission, which is the key characteristic of X-ray Reflection Nebula (XRN; Koyama et al. 1996; Sunyaev & Churazov 1998). The 6.4 keV band image shows an X-ray peak near the molecular cloud (MC) CO 359.4+0.0 (Oka et al. 1998), which is one of the giant MC in the Sgr C complex. The spectrum from X-ray peak show a large absorption in the low energy band, which was also a good evidence that Sgr C is a new XRN. Although the absorption of Sgr C was smaller than that of Sgr B2, the well-established XRN, by an order of magnitude, this is reasonable because the mass of the Sgr C cloud is about one-seventh that of the Sgr B2 cloud (Oka et al. 1998).

Suzaku observed Sgr C complex region from 20^{th} to 23^{rd} February 2006 during the Performance Verification stage. After the data reduction, the effective time is 115 ks for each XIS. The observation mode is the 3×3 mode for almost all (∼97%) of the data.

Figure 7.9 shows the X-ray intensity maps at various energies. 6.4 keV line (upperleft panel) emission consists of primarily neutral Fe atoms of which a K-shell electron is released. 2.45 keV and 6.7 keV lines are from He-like S and He-like Fe, respectively. Thanks to the *Suzaku*'s superior energy resolution, we could reliably

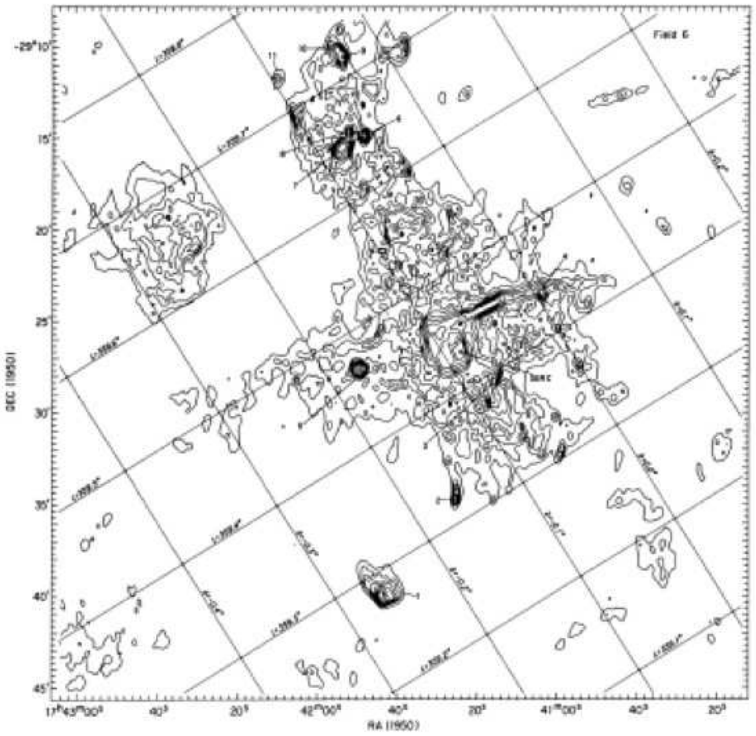

Figure 7.8: Contour map of radio continuum emission around Sgr C region taken at 1616 MHz with Very Large Array. The beam width was 13″.2 by 23″ ($\alpha \times \delta$).

make narrow-band images. We can see some new structures. First, new 6.4 keV clump around (l,b) = (359.5, –0.2), which is consistent with the position of M359.5–0.15 in Liszt & Spiker (1995) can be seen. Second, a strong emission around the center of FOV in the 2.45 keV map (hereafter we call this emission G359.4–0.1) and somewhat "blowout" structure which extends upperward in the figure from G359.4–0.1.

G359.4–0.1 and "blowout" structure indicate that there is thin-thermal plasma component superposed on the GC hot plasma and 6.4 keV clumps. In order to see the characteristics of this component, we extract spectra from these regions. Figure 7.10 shows the XIS spectra from G359.4–0.1 and "blowout" region. Since the three components shown in figure 7.9 overlap each other, the contamination by the other two components is inevitable. So we add the 6.4 keV (Kα) and 7.1 keV (Kβ) line and power-law components to the fitting model in the case of G359.4–0.1. the interval and intensity ratio of the Kα and Kβ was fixed to the value obtained with ground experiments. For the "blowout" spectrum, we also add the GC hot plasma component, of which all the parameter such as absorption, temperature and abundance is fixed to the value in Koyama et al. (2006b) and only the normalization is free. The derived parameter for the component we interested in is shown in table 7.6. Both emissions are well fitted with thin-thermal plasma model with strong absorption and temperature of $\sim$0.7 keV.

Table 7.6: Best-Fit Parameters of G359.4–0.1 and "blowout" region

Parameters	G359.4–0.1	"blowout"
$N_{\rm H}$ ($10^{22}{\rm cm}^{-2}$)...	12.0 (11.0 - 15.1)	9.6 (8.9 - 9.9)
kT (keV)...	0.71 (0.56 - 0.94)	0.71 (0.56 - 0.75)
[S/H]^a...	1.6 (1.1 - 2.0)	1.3 (1.0 - 1.7)
[Ar/H]^a...	2.0 (1.0 - 2.8)	2.7 (1.5 - 3.7)
[Ca/H]^a...	2.2 (0.6 - 3.8)	1.4 ($<$ 4.1)
Flux^b (ergs cm^{-2} s^{-1})...	3.6×10^{-13}	2.9×10^{-13}
χ^2/d.o.f. ...	54.0/82	79.0/84

Note. Parentheses indicate single-parameter 90% confidence regions.
a: Abundance ratio relative to the solar value (Anders & Grevesse 1989).
b: Absorbed flux in the 2.0 - 10.0 keV band.

7.4 CTB 37A

CTB 37A is one of the radio-bright SNRs in the CTB 37 complex. Figure 7.11 shows a contour map from the radio (90 cm) observation. A bright radio shell with a radius of $\sim 3'$ can be clearly seen, overlapping G348.5–0.0 in the east side. CTB 37A is actually two SNRs overlapped in projection (Kassim et al. 1991). One of them, G348.5+0.1 (to the west in figure 7.11), is a partial shell with a faint extension out the open end of the shell ("breakout" morphology), while the other one, G348.5–0.0 (to the east in figure 7.11), is a partial shell. CTB 37B, another radio SNRs complex locates near from CTB 37A ($\sim 20'$), hence this region can be categorized to be the SB formation site. Caswell et al. (1975) concluded by H I observations that CTB 37A is beyond the tangential point, and Frail et al. (1996) obtained the consistent result of 11 pc by OH maser (1720 MHz) observations, which corresponds with a shell radius of ~ 10 pc. An inspection of the CO emission toward CTB 37A detected the MC that were probably accompanied by OH masers in the northern part of the shell (Reynoso & Mangum 2000).

In the X-ray band, CTB 37A was detected by the *ASCA* Galactic plane survey data. However, due to the stray light from a bright southward source and the limited statistics, we could not determine whether the X-ray emission from CTB 37A is thermal or non-thermal. In order to clarify the X-ray emission mechanism and to obtain the X-ray emission map of the inside the SNRs, we observed CT 37A with *Chandra*/ACIS-I and *XMM-Newton*/EPIC. The observed dates and targeted positions are given in table 7.7. Data acquisition from the ACIS was made in the timed-exposure very faint mode in order to significantly reduce the particle background. The data reductions and analyses were made using the CIAO software, version 3.0. For the *XMM-Newton* data, EPIC CCDs were operated in the full-frame mode with the medium filter. We conducted the background flare cut with the same way as section 7.2. Then, we obtain the effective exposure as shown in

table 7.7, while the intrinsic exposure was 20 ksec.

Table 7.7: Observation Log around CTB 37A

Obs.	Satellite	Obs. ID	R.A. (J2000.0)	Decl. (J2000.0)	Date	Exposure (ks)
1...	Chandra	6721	17 14 35.2	-38 31 38.4	2006 Oct 7	20
2...	XMM-Newton	0306510101	17 14 31.2	-38 29 54.2	2006 May 1	13

Note.—Units of right ascension are hours, minutes, and seconds, and units of declination are degrees, arcminutes, and arcseconds.

Figure 7.12 shows the three color X-ray image obtained with *Chandra*. The energy bands are 0.5 - 2.0 keV for red, 2.0 - 7.0 keV for green, and 7.0 - 10.0 keV for blue image, respectively. The new features discovered by our observations are that the northeast part of the G348.5–0.0 show the strong soft X-ray emission while G348.5+0.1 does not show significant emission and that there is a knot-like structure which emit strong hard X-rays at the wast edge of G348.5–0.0.

We then extracted the X-ray spectra from the primarily X-ray emitting region in G348.5–0.0 except for the knot. Figure 7.13 shows two spectra, one of which is extracted from the northeast part of G348.5–0.0 except for knot region, and the other is from knot region. While the former shows some emission lines from He-like Si and S, the latter shows the smooth continuum emission. Hence the X-rays from G348.5–0.0 can be fitted with the thin-thermal plasma model and those from the knot can be reproduced by power-law emission. The best fit parameters are shown in table 7.8. Because the absorption of the latter is about three times stronger than the former, the origin of the emission from the knot structure, which we expected to be the non-thermal X-rays from this SNR in the *ASCA* spectrum, is possibly an object which locates on the line of sight along G348.5–0.0 accidentally.

Table 7.8: Best-Fit Parameters of G348.5–0.0 and knot

Parameters	G348.5–0.0	knot
kT_1/Γ (keV/M)...	0.38 (0.32 - 0.51)	1.8 (1.3 - 2.3)
$kT_2(keV)$...	1.55 (1.41 - 1.95)	...
[Mg/H]^c...	1.2 (0.86 - 1.7)	...
[Si/H]^c...	1.3 (1.0 - 1.6)	...
[S/H]^c...	1.6 (1.2 - 2.0)	...
Flux^d (ergs cm^{-2} s^{-1})...	5.6×10^{-12}	3.7×10^{-12}
$N_{\rm H}^{{\rm LMC}e}$ ($\times 10^{22}$ cm^{-2})...	3.7 (3.3 - 4.0)	10 (7.9 - 12)

Notes.—Parentheses indicate single-parameter 90% confidence regions.
a: Ionization timescale, where ne and tp are the electron density and age of the plasma.
b: Emission measure EM = $\int n_e n_p dV \simeq n_e^2 V$ where n_p and V are the proton density and the plasma volume, respectively. The distance to LMC is assumed to be 50 kpc.
c: Abundance ratio relative to the solar value (Anders & Grevesse 1989).
d: Absorbed flux in the 0.5 - 9.0 keV band.
e: Absorption column in the LMC. The abundances are assumed to be the average LMC values (Russel & Dopita 1992; Hughes et al. 1998).
f: Fixed to the same value as that for the NEI component.

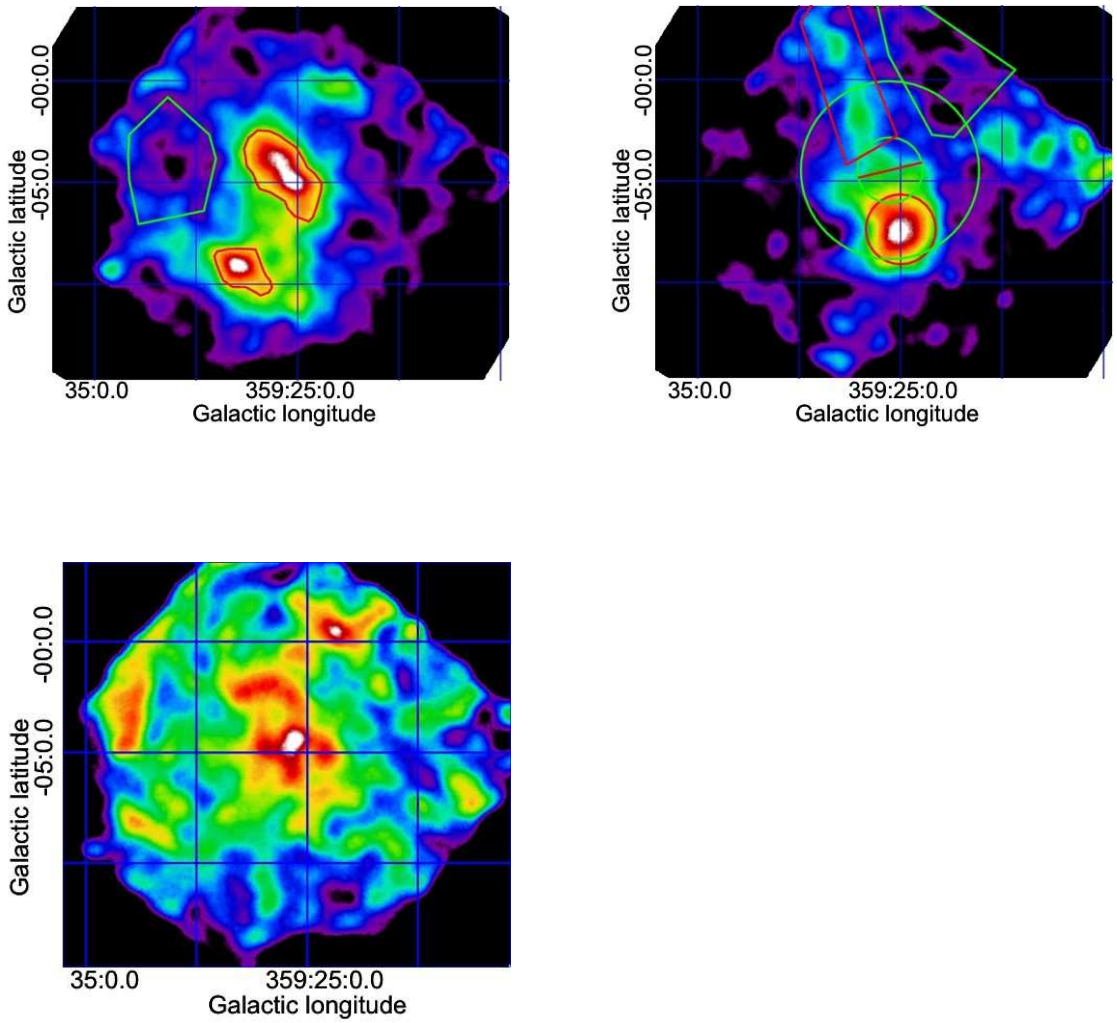

Figure 7.9: X-ray images of Sgr C region. The energy bands are 6.4 keV, 2.45 keV (He-like S Kα line), 6.7 keV (He-like Fe $K\alpha$) for upperleft, upperright, bottomleft panel, respectively. Particle background component is subtracted and the effective exposure is corrected. Red and green polygonal regions indicate the source and background regions adopted in the following spectral analysis, respectively.

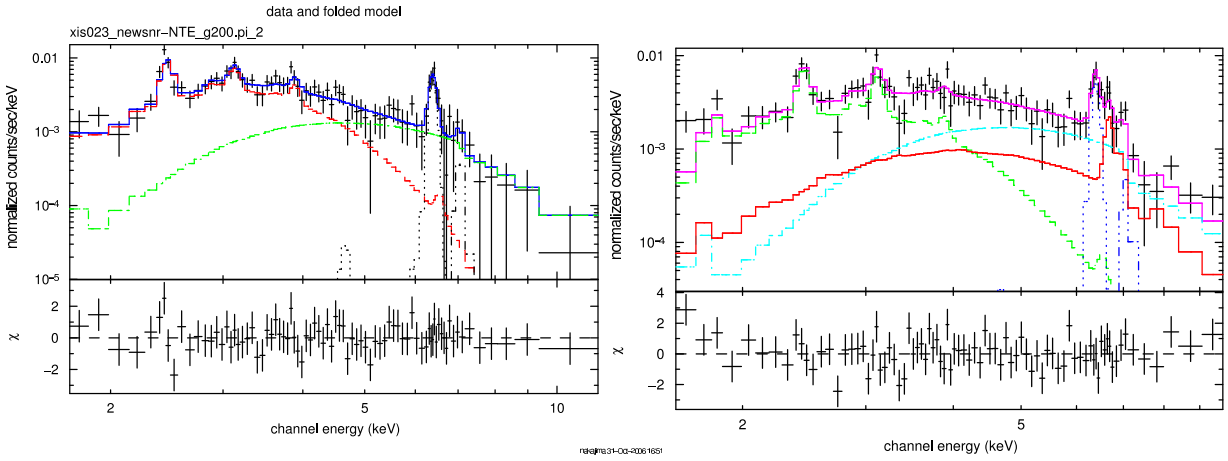

Figure 7.10: (Left panel:)Background-subtracted spectrum extracted from G359.4–0.1 region. The power-law (green) component and 6.4 keV line emission in the fitted model function are the contaminants by the emission distributed over the FOV. (Right panel:) Background-subtracted spectrum extracted from "blowout" region. The hot plasma component of GC (red), power-law component (sky blue), and 6.4 keV line emission (blue) are also in the fitted model function as the contaminants.

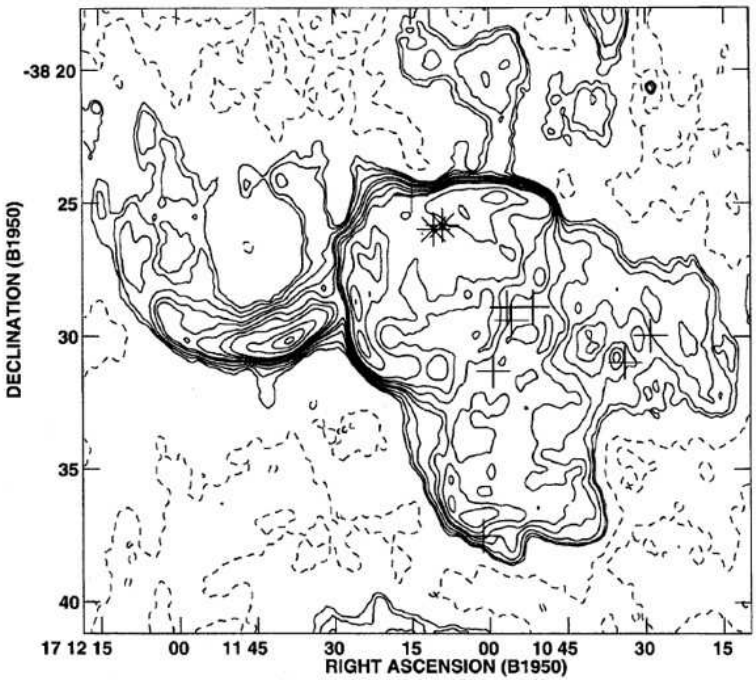

Figure 7.11: A radio continuum image of CTB 37A region at 1.4 GHz from Kassim et al. (1991). The positions of OH (1720 MHz) masers are superimposed as crosses on the image. The beam size is 32″ by 18″ ($\alpha \times \delta$).

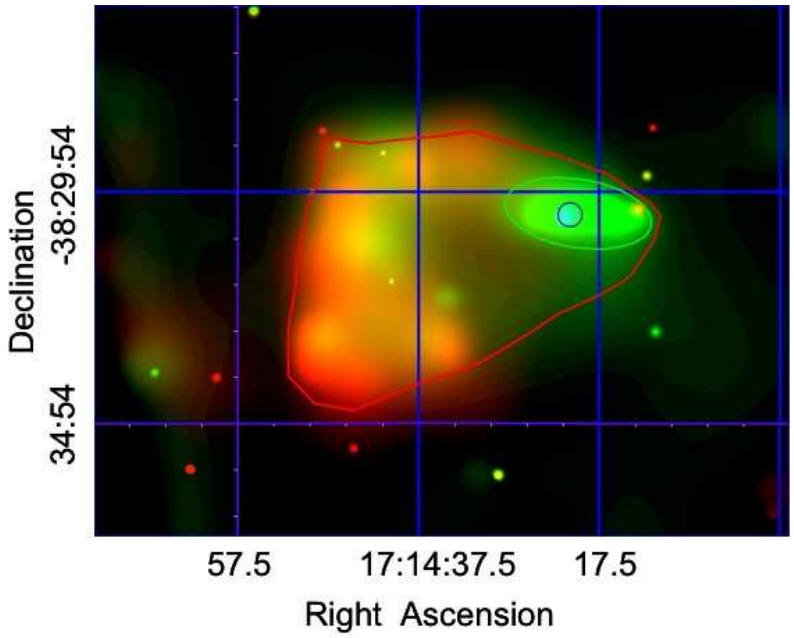

Figure 7.12: The *Chandra* three-color image of CTB 37A region (red = 0.5 - 2.0 keV, green = 2.0 - 7.0 keV, blue = 7.0 - 10.0 keV). Red, green, and blue regions indicate the source regions adopted in the following spectral analysis.

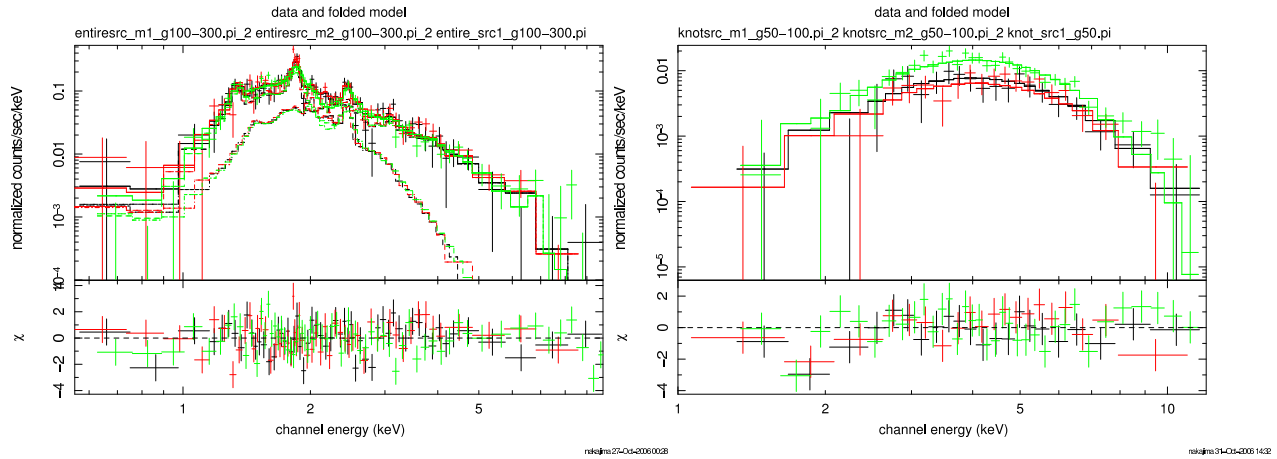

Figure 7.13: (Left panel:)Background-subtracted spectra of ACIS-I and EPIC extracted from the northeast part of G348.5–0.0 although the "knot" region is eliminated. (Right panel:) The same as left panel but for knot region.

Chapter 8

Discussion

8.1 Cosmic Ray Acceleration in SB

30 Dor C is an SB made by a strong stellar wind and/or successive SN explosions of massive stars located in the OB star association LH 90. The age of this star association, or that of 30 Dor C, is on the order of a few to 10 Myr (Lucke & Hodge 1970). The thermal emissions are enhanced in the southeastern side of 30 Dor C (around shell A). The position of this component coincides with that of the Hα emission (Dunne et al. 2001). The plasma temperature of 30 Dor C is rather high compared to those of other LMC SBs (Dunne et al. 2001), although it becomes significantly lower than previous results. Perhaps because of the poor spectral resolution of *ROSAT*, previous observations could not resolve the power-law component (hard spectrum) from the thermal emission.

The X-ray luminosity of 30 Dor C is significantly lower than that of the other SBs (Dunne et al. 2001). With the assumption that the plasma in shell A distributes uniformly in the ellipsoid with radii of $58'' \times 34'' \times 34''$ (total volume $V = 1.2 \times 10^{59}$ cm^3), the mean density (n_e), thermal energy (E), and the age of the plasma (t_p) were calculated as follows using the emission measure EM $= n_e^2 V$ and ionization timescale (see table 7.3)

$$n_e = 4.7(4.2 - 4.8) \times 10^{-1} \text{ cm}^{-3}, \tag{8.1}$$

$$E \simeq 3 n_e kTV = 5.7(4.6 - 6.4) \times 10^{49} \text{ ergs}, \tag{8.2}$$

$$t_p = 6.7(> 0.5) \times 10^5 \text{ yr}. \tag{8.3}$$

Together with the Hα emission around shell A (Dunne et al. 2001), we infer that the shell of 30 Dor C collides with dense matter and temporally emits thermal X-rays with a relatively high temperature. The overabundance of a light element (Mg) relative to a heavier element (Fe) may indicate that a Type II SN occurred (Tsujimoto et al. 1995). Thus, the progenitor is a massive star that is a member of cluster LH 90 (Lucke & Hodge 1970) near the center of 30 Dor C (see § 4.4).

In the 843 MHz band, Mills et al. (1984) found a clear radio shell that is brightest on the southwestern side (around shells C and D) and dim on the eastern side. The nonthermal X-ray emissions are enhanced at the radio bright shell. This fact implies that the nonthermal X-rays are emitted by the same mechanism as the radio band. Therefore, the nonthermal X-rays are likely to be synchrotron radiation from the accelerated electrons, like SN 1006 (Koyama et al. 1995) and other SNRs, which accelerate particles up to TeV. The X-ray photon index of 2.1 - 2.9 (see table 7.4) is, in fact, typical to synchrotron emissions.

To verify the synchrotron origin, we fitted the X-ray spectra with an SRCUT model, which represents the synchrotron emission from electrons with an energy distribution of a power law plus exponential cutoff (Reynolds 1998, 1999). Since the radio index data are not accurate as a result of the large background and contamination of thermal emission (Mathewson et al. 1985), we fixed the spectral index (α) at 1 GHz to be 0.5, which is expected from the first-order Fermi acceleration and similar to that of SN 1006 ($\alpha = 0.57$; Allen et al. 2001).

The fittings were statistically acceptable; the best-fit parameters are listed in table 7.4. The best-fit cutoff frequency is also similar to that of SN 1006, although the age of 30 Dor C may be on the same order as that of LH 90 (10 Myr; Lucke & Hodge 1970), which is far larger than SN 1006. This implies that, depending on the environment, the acceleration of high-energy electrons up to the knee energy can continue for a far longer time than the previous consensus for the SNR case ($\sim 10^3$ yr; Reynolds 1999). The electron acceleration time may have been extended, because successive SN explosions in 30 Dor C, possibly over the course of a few Myr, may more-or-less continuously produce high-energy electrons. The total luminosity of the nonthermal component ($\sim 5.3 \times 10^{35}$ ergs s^{-1}) is about 10 times larger than that of SN 1006 (Koyama et al. 1995). This large nonthermal flux in 30 Dor C would be due to the large energy supply from multiple successive SN explosions.

The expected flux density at 1 GHz is 3.0 (2.4 - 4.6) $\times 10^{-2}$ Jy with $\alpha = 0.5$, which is significantly smaller than the observed value (1.0 Jy; Mills et al. 1984). This "inconsistency" is not relaxed, even if we assume a larger radio index of $\alpha = 0.6$ [1.8 (1.4 - 2.5) $\times 10^{-1}$ Jy, as shown in table 7.4]. We infer that the larger observed radio flux than that expected from X-rays would be due to either the contamination of thermal radio flux or a large uncertainty of the background level (see Mills et al. 1984).

The Hα emission (Dunne et al. 2001) is anticorrelated with the nonthermal components. Similar features have been observed in some of other SNRs with synchrotron X-rays: SN 1006 (Winkler et al. 1997) and RCW 86 (Smith 1997). Because the Hα region has higher density, it may have a higher magnetic field. Therefore, the maximum electron energy is limited by the quick synchrotron energy loss, leading to reduced nonthermal X-rays.

We have identified three pointlike X-ray sources (sources 1, 3, and 4) to the tight clusters of massive stars α, β, and γ, respectively. The spectrum of source 1 (α) is fitted with a thin-thermal plasma model of $\sim$2.1 keV, which is consistent with stellar X-rays from massive stars. The cluster α is the brightest of the three, with X-ray luminosity of $\sim 10^{34}$ ergs s^{-1}. Optical spectroscopy of this cluster revealed that it

includes one red giant and one Wolf-Rayet (W-R) star (MG 41 and Brey 58; Lortet & Testor 1984). Hence, the latter is a possible counterpart of the 2 keV source. The X-ray luminosity is near to the upper end of a massive star, or its binary (Maeda et al. 1999). Although the X-ray luminosity of source 3, a counterpart of the star cluster β, is also consistent with a massive young star, the best-fit photon index, $\sim$2 (see table 7.2), is rather typical of a rotation-powered neutron star, probably a stellar remnant of an SN explosion in the active star cluster. The spectrum of source 3 (γ) is soft and well fitted, with a kT = 1.0 keV thermal plasma model, similar to a cluster α. The star cluster γ also includes one OB star (Sk -69°.212; Sanduleak 1970), and the X-ray luminosity is consistent with that of a young massive star.

The other three sources (2, 5, and 6) have no counterpart in optical, in the infrared band (Breysacher et al. 1981; Lortet & Testor 1984), nor in the SIMBAD database. Their spectra are relatively hard and are consistent with being background active galactic nuclei (AGNs) or stellar remnants (black hole or neutron star) by successive SN explosions.

In order to constrain the nature of the pointlike X-ray sources with a power-law spectrum, we further examined the time variability with the Kolmogorov-Smirnov test (Press et al. 1992). However, no significant time variability was found even between the two observations. For high-resolution timing, we examined the *Chandra* HRC data (ObsID = 738), but no pulsation was found from any of these point sources.

As shown in chapter 7, significant non-thermal X-rays were not detected from other SBs or SB formation sites. This may have relation to the breakout, which is obviously seen in N44. As described in section 6.2.3, hot and tenuous environment inside SBs are essential condition for the effective particle acceleration. If the gas inside the SB leak into the outer ISM, the strength and turbulance of the magnetic field become weak and hence results as the less-effective acceleration.

8.2 Energetics of Superbubble

Utilizing the thermal energy derived in section 7.2, we investigate the energy balance in the case of N44.

For the amount of energy injection to SB, the combined action from SN and stellar winds from OB-type stars must be considered. Oey & Massey (1995) derived the approximate age of LH 47 from the initial mass function of members to be $\sim$10 Myr, then the integral of mechanical luminosity of stellar wind from OB-type stars and SN explosion are $\sim 3\times10^{51}$ ergs and ~ 1–4×10^{51} ergs respectively.

On the other hand, the amount of energy ejection can be estimated by measuring the thermal energy of hot gas in the SB and kinetic energy of H I and H II shell. Kim et al. (1998) estimated the latters to be $\sim 2.4\times10^{50}$ ergs and $\sim 5.0\times10^{49}$ ergs respectively, which is negligible compared with SN explosion energy. Thermal energy inside the main shell, which can be calculated from flux, is $2.62\times10^{51}\ \sqrt{\epsilon}$ ergs (where the ϵ is filling factor). Furthermore we also derived the flux and thermal energy from blowout region and western another shell (Figure 7.4). The sum of the thermal

energy is 2.15×10^{51} $\sqrt{\epsilon}$ ergs. Then the total thermal energy is 4.77×10^{51} $\sqrt{\epsilon}$ ergs, which reaches to the total injected energy.

This feature shows a clear contrast against N51D, another SB in the LMC. In the case of N51D, approximately two third of the injected energy is missing (Cooper et al. 2004) which means a significant fraction of the stellar mechanical energy must have been converted into other forms of energy. The X-ray spectrum of the diffuse emission from N51D requires a power-law component to explain the featureless emission at 1.0 - 3.0 keV. The origin of this power-law component is unclear, but it may be responsible for the discrepancy between the stellar energy input and the observed interstellar energy in N51D. In the case of N44, no significant diffuse non-thermal emission possibly corresponds to the negligible amount of missing energy. The case dependency of the amount of the missing energy have to be investigated more detail comparing our X-ray dataset with data of other bands.

In the typical case of X-ray emission from OB-type stars, the temperature of hot plasma is <1.0 keV and the solar abundance. The hot plasma in the vicinity of OB-type stars shows quite a similar feature; the abundance of Ne and Mg is similar to the solar value, while other region inside the main shell show consistent results with the mean LMC value of 0.3. According to the catalog in the Oey & Massey (1995), there are at least 4 O-type stars and 5 B-type stars in this region. On the other hand the absorption corrected flux in the energy band of 0.2–2.0 keV is 1.49×10^{-13} ergs cm^{-2} s^{-1} which corresponds to the luminosity of 4.50×10^{34} ergs s^{-1}. Considering the luminosity of galactic O-type stars (Babel & Montmerle 1997), this value is not too large because there must be some contamination from diffuse hot gas which fills entire shell. Hence we possibly first detect the contribution from OB-type stars to the hot gas in an SB separately from that of SNRs.

Chapter 9

Conclusion

9.1 Conclusion for XIS calibration

The results of ground and in-orbit experiments of the CI capability of the XIS are as follows:

1. The amount of injected charges (Q) are sufficiently stable (dispersion of 91 eV in FWHM), which should be compared to the X-ray energy resolution (FWHM of 113 eV) with the same amount of charges.

2. The CTI depends on PHA of the charge. The charge loss can be explained as $\delta Q \propto Q^{0.62-1.00}$

3. With the $\mathrm{CTI_{CI}}$ correction , the energy resolution (FWHM) of ^{55}Fe is improved from 193 eV to 173 eV approximately one year after the launch and the residual around the tail component in the line profile is also significantly reduced.

4. The improved charge compensation method is applied to the Tycho's SNR data, which results in the same benefit as the calibration source data.

5. We confirm that the energy resolution can be largely improved by filling the charge trap. Hence, we are currently trying another in-orbit CI capability experiment to actively fill the CTs in the transfer channel by the CI technique.

9.2 Conclusion for SBs study

The results of study of the energetics and particle acceleration in the SBs are as follows:

1. In the shell of the superbubble 30 Dor C, we resolved non-thermal and thermal X-rays using *Chandra* and *XMM-Newton* data. The nonthermal X-rays are located in the northern and western parts of the SB. The power-law model is well fitted to the spectra with $\Gamma = 2.1$ - 2.9, similar to that of the cosmic-ray accelerating SNR, SN 1006. This is the first discovery of nonthermal X-rays

from the shells of SBs. The total luminosity is 10 times larger than that of SN 1006. Only thermal emission could be seen in the case of N44, CTB 37A, and Sgr C.

2. If we consider the breakout region around the main shell of N44, the sum of the thermal energy of hot gas and kinetic energy is consistent with the expected injected energy by the stellar wind and supernovae.

3. The contrast between 30 Dor C and other SBs may have relation to the breakout, which is obviously seen in N44. While, hot and tenuous environment inside SBs are essential condition for the effective particle acceleration, the strength and turbulance of the magnetic field become weak and hence results as the less-effective acceleration due to the inner gas leakage into the outer ISM.

Bibliography

Abbott, D. C., 1982, ApJ, **263**, 723

Åberg, T., 1971, Phys. Rev. A, **4**, 1735

Allen, G. E., Petre, R., & Gotthelf, E. V., 2001, ApJ, **558**, 739

Anders, E., & Grevesse, N., 1989, Geochim. Cosmochim. Acta, **53**, 197

Apanasenko, A. V. et al., 2001, Izv. Akad. Nauk, Ser. Fiz., **65**, 433

Arabadjis, J. S., & Bregman, J. N., 1999, ApJ, **510**, 806

Arnaud, K. A. 1996, in ASP Conf. Ser. 101, Astronomical Data Analysis Software and Systems V, ed. G. H. Jacoby & J. Barnes (San Francisco: ASP), 17

Babel, J., & Montmerle, T., 1997, ApJ, **485**, L29

Bamba, A., Koyama, K., & Tomida, H., 2000, PASJ, **52**, 1157

Bamba, A., Ueno, M., Nakajima, H., & Koyama, K., 2004, ApJ, **602**, 257

Bautz, M. W., Kissel, S. E., Prigozhin, G. Y., Jones, S. E., Isobe, T., Manning, H. L., Pivovaroff, M., Ricker, G. R., & Woo, J., 1996, Proc. SPIE, **2808**, 170

Bautz, M. W., Kissel, S. M., Prigozhin, G., LaMarr, B., Burke, B. E., Gregory, J. A., & The XIS Team, 2004, Proc. SPIE, **5501**, 111

Bearden, J. A., 1967, Rev. Mod. Phys., **39**, 78

Bell, A. R., & Lucek, S. G., 2001, MNRAS, **321**, 433

Berezhko, E. G., & Völk, H. J., 2004, A&A, **427**, 525

Berezhko, E. G., Ksenofontov, L. T., & Völk, H. J., 2003, A&A, **412**, L11

Bird, D. J. et al., 1993, Phys. Rev. Lett., **71**, 3403

Blaauw, A. 1991, in the Physics of Star Formation and Early Stellar Evolution, NATO Advanced Science Institutes (ASI) Ser. C, ed. C. J. Lada & N. D. Kylafis (Kluwer: Dordrecht), 342, 125

Blinnikov, S. I., Imshennik, V. S., & Utrobin, V. P., 1982, SvAL, **8**, 361

Blondin, J. M.. Wright, E. B., Borkowski, K. J., & Reynolds, S. P., 1998, ApJ, **500**, 342

Bomans, D. J., Rossa, J., Weis, K., & Dennerl, K., 2003, in IAU Symposium, No. 212, ed. K. A. van der Hucht, A. Herrero, & C. Esteban (San Francisco: ASP), 637

Borkowski, K. J., Lyerly, W. J., & Reynolds, S. P., 2001, ApJ, **548**, 820

Borkowski, K. J., Rho, J., Reynolds, S. P., & Dyer, K. K., 2001, ApJ, **550**, 334

Born, M., & Wolf, E., 1999, Principles of optics, 7th, ed. (Cambridge: Cambridge University Press), 67

Bresolin, F., Kennicutt, R. C., Jr., & Garnett, D. R., 1999, ApJ, **510**, 104

Breysacher, J., 1981, A&AS, **43**, 203

Burke, B. E., Gregory, J. A., Loomis, A. H., Lesser, M., Bautz, M. W., Kissel, S. E., Rathman, D. D., Osgood, R. M., III, & Cooper, M. J., 2004, IEEE Trans. Nucl. Sci., **51**, 2322

Burrows, D. N. et al., 2000, ApJ, **543**, L149

Butt, Y. M., Torres, D. F., Combi, J. A., Dame, T., & Romero, G. E., 2001, ApJ, **562**, L167

Bykov, A. M., 2001, Space Sci. Rev., **99**, 317

Bykov, A. M., & Fleishman, G. D., 1992, MNRAS, **255**, 269

Bykov, A. M., & Toptygin, I. N., 2001, Ast. L, **27**, 625

Casse, F., Lemoine, M., & Pelletier, G., 2002, Phys. Rev. D, **65**, 3002

Castor, J., McCray, R., & Weaver, R., 1975, ApJ, **200**, L107

Caswell, J. L., Murray, J. D., Roger, R. S., Cole, D. J., & Cooke, D. J., 1975, A&A, **45**, 239

Chevalier, R. A., 1974, ApJ, **188**, 501

Chevalier, R. A., 1976, ApJ, **207**, 872

Chu, Y. -H., & Mac Low, M. -M., 1990, ApJ, **365**, 510

Chu, Y. -H., Mac Low, M. -M., Garcia-Segura, G., Wakker, B., & Kennicutt, R. C., Jr., 1993, ApJ, **414**, 213

Chu, Y. -H., Chang, H. -W., Su, Y. -L., & Mac Low, M. -M., 1995, ApJ, **450**, 157

Clark, D.H., & Caswell, J.L., 1976, MNRAS, **174**, 267

Cooper, R. L., Guerrero, M. A., Chu, Y. -H., Chen, C. -H. R., & Dunne, B. C., 2004, ApJ, **605**, 751

Cox, D. P., 1972, ApJ, **178**, 159

Cox, D. P., & Smith, B. W., 1974, ApJL, **189**, 105

Davies, R. D., Elliott, K. H., &Meaburn, J., 1976, MNRAS, **81**, 89

De Young, D. S. & Gallagher, J. S., III, 1990, ApJL, **356**, 15

Dennerl, K. et al., 2001, A&A, **365**, L202

Dickey, J. M., & Lockman, F. J., 1990, ARAA, **28**, 215

Dunne, B. C., Points, S. D., & Chu, Y. -H., 2001, ApJS, **136**, 119

Enomoto, R. et. al., 2002, Nature, **416**, 823

Falle, S. A. E. G., 1981, MNRAS, **195**, 1011

Falle, S. A. E. G., 1988, Proceedings of IAU Colloq. **101**, 419

Feast, M., 1999, PASP, **111**, 775

Frail, D. A., Goss, W. M., Reynoso, E. M., Giacani, E. B., Green, A. J., & Otrupcek, R., 1996, AJ, **111**, 1651

Fukui, Y. et al., 1999, PASJ, **51**, 745

Garmany, C. D., 1994, PASP, **106**, 25

Gendreau, K. C. 1995, PhD, Massachusetts Institute of Technology

Gendreau, K., Bautz, M. W., & Ricker, G., 1993, Proc. SPIE, **335**, 318

Georgelin, Y. M., Georgelin, Y. P., Laval, A., Monnet, G., & Rosado, M., 1983, A&AS, **54**, 459

Goudis, C., & Meaburn, J., 1984, A&A, **137**, 152

Grant, C.E., Bautz, M.W., Kissel, S.M., & LaMarr, B., 2004, Nucl. Instr. and Meth. A, **5501**, 177

Green, D. A., 2004, BASI, **32**, 335

Gull, S. F., 1973, MNRAS, **161**, 47

Haberl, F., & Pietsch, W., 1999, A&AS, **139**, 277

Hamaguchi, K., Maeda, Y., Matsumoto, H., Nishiuchi, M., Tomida, H., Koyama, K., Awaki, H., & Tsuru, G. T., 2000, Nucl. Instr. and Meth. A, **450**, 360

Hardy, T., Murowinski, R., & Deen, M. J., 1998, IEEE Trans. Nucl. Sci., **45**, 154

Haynes, R. F. et al., 1990, In "Galactic and Intergalactic Magnetic fields" IAU Symp., No.140, 205, eds. Beck, R., Kronberg, P., & Dordrecht, R. W. K.

Henize, K. G., 1956, ApJS, **2**, 315

Hess, V. F., 1912, Phys. Z., **13**, 1084

Higdon, J. C., & Lingenfelter, R. E., 2005, ApJ, **239**, 867

Higdon, J. C., & Lingenfelter, R. E., 2005, ApJ, **628**, 738

Higdon, J. C., Lingenfelter, R. E., & Ramaty, R., 1998, ApJL, **509**, 33

Holland, A., Abbey, A., Lumb, D., & McCarthy, K., 1990, Proc. SPIE, **1344**, 378

Holland, A. D., Turner, M. J., Abbey, A. F., & Pool, P. J., 1996, Proc. SPIE, **2808**, 414

Hughes, J. P., Hayashi, I., & Koyama, K., 1998, ApJ, **505**, 732

Itoh, M., Tanaka, R., & Komatsu, H. 2001, in ASP Conf. Ser. 251, New Century of X-Ray Astronomy, ed. H. Inoue & H. Kuneida (San Francisco: ASP), 250

Jamison, K. A., Hall, J. M., Oltjen, J., Woods, C. W., Kauffman, R. L., Gray, T. J., & Richard, P., 1976, Phys. Rev. A, **14**, 937

Janesick, J. R., Soli, G., Elliott, T. S., & Collins, S. A., 1991, Proc. SPIE, **1447**, 87

Jansen, F. et al., 2001, A&A, **365**, L1

Kaastra, J. S. 1992, An X-Ray Spectral Code for Optically Thin Plasmas (Internal SRON-Leiden Rep., updated ver. 2.0; Leiden: SRON)

Kampert, K. -H. et al., 2001, in 27th International Cosmic Ray Conference, ed. R. Schlickeiser (Copernicus Gesellschaft), 240

Kassim, N. E.. Weiler, K. W., & Baum, S. A., 1991, ApJ, **374**, 212

Kim, S., Chu, Y. -H., Staveley-Smith, L., & Smith, R. C., 1998, ApJ, **503**, 729

Kitamoto, S. et al., 2004, Proc. SPIE, **5168**, 376

Knoll, G. F., 1989, Radiation Detection and Measurement, John Wiley & Sons, New York, pp.405

Kokubun, M. et al., 2006, PASJ, accepted (astro-ph 0611233)

Koo, B. -C., & Kang, J., 2001, MNRAS, **349**, 983

Koyama, K., Petre, R., Gotthelf, E. V., Hwang, U., Matsura, M., Ozaki, M., & Holt, S. S., 1995, Nature, **378**, 255

Koyama, K., Maeda, Y., Sonobe, T., Takeshima, T., Tanaka, Y., & Yamauchi, S., 1996, PASJ, **48**, 249

Koyama, K. et al., 2006, PASJ, accepted

Koyama, K. et al., 2006, PASJ, accepted (astro-ph 0609215)

Krause, M. O., & Oliver, J. H., 1979, J. Phys. Chem. Ref. Data, **8**, 329

LaMarr, B., Bautz, M. W., Kissel, S. M., Prigozhin, G., Hayashida, K., Tsuru, T., & Matsumoto, H., 2004, Proc. SPIE, **5501**, 385

Le Marne, A. E., 1968, MNRAS, **139**, 461

Lesser, M., & Iyer, V., 1998, Proc. SPIE, **3355**, 446

Liszt, H. S., & Spiker, R. W., 1995, ApJS, **98**, 259

Long, K. S., Helfand, D. J., & Grabelsky, D. A., 1981, ApJ, **248**, 925

Lortet, M. C., & Testor, G. 1984, A&A, **139**, 330

Lucke, P. B., & Hodge, P. W., 1970, AJ, **75**, 171

Lumb, D. H., & Nousek, J. A., 1990, Proc. SPIE, **1736**, 138

Mac Low, M. -M., & McCray, R., 1988, ApJ, **324**, 776

Maeda, Y., Koyama, K., Yokogawa, J., & Skinner, S., 1999, ApJ, **510**, 967

Magnier, E. A., Chu, Y. -H., Points, S. D., Hwang, U., & Smith, R. C., 1996, ApJ, **464**, 829

Mathewson, D. S., & Clarke, J. N., 1973, ApJ, **180**, 725

Mathewson, D. S., Ford, V. L., Tuohy, I. R., Mills, B. Y., Turtle, A. J., & Helfand, D. J., 1985, ApJS, **58**, 197

Mathewson, D. S., Ford, V. L., Tuohy, I. R., Mills, B. Y., Turtle, A. J., & Helfand, D. J., 1985, ApJL, **509**, 33

Matsumoto, H. et. al., 2005, Nucl. Instr. and Meth. A, **541**, 357

Matsumoto, H. et. al., 2006, Proc. SPIE, **6266**, 120

McCray, R., & Snow, T. P. 1979, ARAA, **17**, 213

McGee, R. X., Newton, L. M., & Butler, P. W., 1978, MNRAS, **183**, 799

McKee, C. F., & Ostriker, J. P., 1977, ApJ, **218**, 148

McKee, C. F., & Truelove, J. K., 1995, Phys. Rep., **256**, 157

McNamara, D. H., Madsen, J. B., Barnes, J., & Ericksen, B. F., 2000, PASP, **112**, 202

Meaburn, J., & Laspias, V. N., 1991, A&A, **245**, 635

Meidinger, N., Schmalhofer, B., & Strüder, L., 2000, Nucl. Instr. and Meth. A, **439**, 319

Mel'nik, A. M., & Efremov, Y. N. 1995, Astron. Lett., **21**, 10

Mewe, R., Gronenschild, E. H. B. M., & van den Oord, G. H. J. 1985, A&AS, **62**, 197

Meynet, G., Maeder, A., Schaller, G., Schaerer, D., & Charbonnel, C., 1994, ApJS, **103**, 97

Michael, E. et al., 2002, ApJ, **574**, 166

Mills, B. Y., Turtle, A. J., Little, A. G., & Durdin, J. M., 1984, Australian J. Phys., **37**, 321

Mitsuda, K. et al., 2006, PASJ, accepted

Morrison, R., & McCammon, D., 1983, ApJ, **270**, 119

Murakami, H., Koyama, K., Tsujimoto, M., Maeda, Y., & Sakano, M., 2001, ApJ, **550**, 297

Nakajima, H. et. al., 2005, Nucl. Instr. and Meth. A, **541**, 365

Nazé, Y., Chu, Y. -H., Guerrero, M. A., Oey, M. S., Gruendl, R. A., & Smith, R. C., 2002, ApJ, **124**, 3325

Nazé, Y., Antokhin, I. I., Rauw, G., Chu, Y. -H., Gosset, E., & Vreux, J. -M., 2004, A&A., **418**, 841

Odenwald, S. F., & Fazio, G. G., 1984, ApJ, **283**, 601

Oey, M. S. & Massey, P., 1995, ApJ, **452**, 216

Oka, T., Hasegawa, T., Hayashi, M., Handa, T., & Sakamoto, S., 1998, ApJ, **493**, 730

Oort, J. H., Problems of Cosmic Aerodynamics (Central Air Document Office Dayton, OH)

Ostriker, J. P., & McKee, C. F., 1988, *Reviews of Modern Physics*, **60**, 1

Park, S., Burrows, D. N., Garmire, G. P., Nousek, J. A., McCray, R., Michael, E., & Zhekov, S., 2002, ApJ, **567**, 314

Pietrzyński, G., Gieren, W., Fouqué, P., & Pont, F., 2001, A&A, **371**, 497

Plucinsky, P. P. & Virani, S.N., 2000, Proc. SPIE, **4012**, 681

Press, W. H., Teukolsky, S. A., Vetterling, W. T., & Flannery, B. P., 1992, Numerical Recipes in C (2d ed.; Cambridge: Cambridge Univ. Press)

Prigozhin, G., Burke, B., Bautz, M. W., Kissel, S. M., LaMarr, B., & Freytsis, M., 2004, Proc. SPIE, **5501**, 357

Ptuskin, V. S., & Zirakashvili, V. N., 2003, A&A, **403**, 1

Raymond, J. C., & Smith, B. W., 1977, ApJS, **35**, 419

Read, A. M., & Ponman, T. J., 2003, A&A, **409**, 395

Reynolds, S. P., 1998, ApJ, **493**, 375

Reynolds, S. P., & Keohane, J. W., 1999, ApJ, **525**, 368

Reynoso, E. M., & Mangum, J. G., 2000, ApJ, **545**, 874

Richard, P., Oltjen, J., Jamison, K. A., Kauffman, R. L., Woods, C. W., & Hall, J. M., 1975, Phys. Letters A, **54**, 169

Różyczka, M., & Tenorio-Tagle, G., 1985, A&A, **147**, 202

Russel, S. C., & Dopita, M. A., 1992, ApJ, **384**, 508

Ryter, C. E., 1996, Ap&SS, **236**, 285

Sasaki, M., Haberl, F., & Pietsch, W., 2000, A&AS, **143**, 391

Schaller, G., Schaerer, D., Meynet, G., & Maeder, A., 1992, A&APS, **96**, 269

Sedov, L. I., 1959, Similarity and Dimensional Methods in Mechanics (Academic Press, New York)

Sembay, S., Abbey, A., Altieri, B., Ambrosi, R., Baskill, D, Ferrando, P., Mukerjee, K., Read, A.M., & Turner, M.J.L., 2004. Proc. SPIE, **5488**, 264

Shklovskii, I. S., 1962, SvA, **6**, 162

Shockley, E. G., & Read, J. M., 1952, Phys. Rev., **87**, 835

Slane, P., Hughes, J. P., Edgar, R. J., Plucinsky, P. P., Miyata, E/, Tsunemi, H., & Aschenbach, B., 2001, ApJ, **548**, 814

Smith, R. C., 1997, AJ, **114**, 2664

Smith, D. R., Holland, A. D., Hutchinson, I., Abbey, A. F., Pool, P., Burt, D., & Morris, D., 2004, Proc. SPIE, **5501**, 189

Stassinopoulos, E. G., & Barth, J. M., 1991, "Astro-D Charged Particle Environment Study", NASA report X-900-91-07

Stephan, K., Reppin, C., Hirschinger, M., Maier, H. J., Frischke, D. Fuchs, D., Mueller, P., & Guertler, P., 1996, Proc. SPIE, **2808**, 421

Sunyaev, R., & Churazov, E., 1998, MNRAS, **297**, 1279

Takahashi, T., et al., 2006, PASJ, accepted (astro-ph 0611232)

Tenorio-Tagle, G., 1996, AJ, **111**, 1641

Tenorio-Tagle, G., Bodenheimer, P., & Rozyczka, M., 1987, A&A, **182**, 120

Tokunaga, A. T., 2000, Allen's Astrophysical Quantities, 4th ed., ed. A. N.Cox (New York: Springer)

Tompsett, M. F. et al., 1975, IEEE Trans. ED, **22**, 305

Truelove, J. K., & McKee, C. F., 1999, ApJS, **120**, 299

Tsujimoto, T., Nomoto, K., Yoshii, Y., Hashimoto, M., Yanagida, S., & Thielemann, F. -K., 1995, MNRAS, **277**, 945

Tsuru, T., Nishiuchi, M., Awaki, H., Hamaguchi, K., Koyama, K., Tomida, H., Sakano, M., ASTRO-E XIS Team, 2000, AdSpR, **25**, 885

Uchiyama, Y., Takahashi, T., & Aharonian, F. A., 2002, ApJ, **571**, 866

Ueno, M., Bamba, A., Koyama, K., & Ebisawa, K., 2003, ApJ, **588**, 338

van den Bergh, S., & McClure, R. D., 1994, ApJ, **425**, 205

Villa, G. E., et al., 1998, IEEE Trans. Nucl. Sci., **45**, 921

Völk, H. J., Berezhko, E. G., & Ksenofontov, L. T., 2003, A&A, **409**, 563

Wang, Q., & Helfand, D. J., 1991, ApJ, **373**, 497

Watson, M. G. et al., 2001, A&A, 3**65**, L51

Weaver, G. et al., 1997, ApJ, **218**, 377

Weisskopf, M. C., Brinkman, B., Canizares, C., Garmire, G., Murray, S., & Van Speybroeck, L. P. 2002, PASP, **114**, 1

Will J. -M., Bomans D. J., & Dieball A., 1997, A&AS, **123**, 455

Winkler, P. F., & Long, K. S., 1997, ApJ, **491**, 829

Yamaguchi, R., Mizuno, N., Onishi, T., Mizuno, A., & Fukui, Y., 2001, PASJ, **53**, 959

Yamaguchi, H., Nakajima, H., Koyama, K., Tsuru, T. G., Matsumoto, H., Tsunemi, H., Hayashida, K., Torii, K., Namiki, M., Katsuda, S., Matuura, D., & Miyauchi, T., 2006, Proceedings of the The X-ray Universe 2005 Ed. A. Wilson, pp.949

Yamaguchi, H. et al., 2006, Proc. SPIE, **6266**, 121

Appendix A

Abbreviations

CP Charge Packet

CTI Charge Transfer Ineeficiency

CTI$_{\mathrm{COL}}$ CTI measured for each column

CTI$_{\mathrm{AVE}}$ CTI measured averaged among columns

CT Charge Trap

GC Galactic Center

LMC Large Magellanic Cloud

SB Superbubble

SNR Supernova Remnant

SN Supernova

Acknowledgment

First of all, I am deeply grateful to my supervisor, Prof. K. Koyama, Assoc. Prof. T. Tsuru, and Res. Assoc. H. Matsumoto for their continual guidance, advice and support throughout my graduate career. Their patience and sometimes strict guidance led me to complete this work.

I express my thanks to Dr. A. Bamba and M. Ueno, who carried out part of the study of SB samples, the results of them are so amazing and wonderful. Dr. A. Bamba, especially, kindly gave me advices and suggestions on the LMC SNRs, which were so useful and helpful to me.

I am also grateful to my collaborators, Prof. H. Tsunemi, Assoc. Prof. K. Hayashida, Res. Assoc. K. Torii, Mr. S. Katsuda, M. Shoji, D. Matsuura, and T. Miyauchi for their great helps in conducting the ground experiments at Osaka University.

I also thank all the members of the Cosmic-ray laboratory in Kyoto University for the daily discussion and insightful comments, as well as for the kind and heartful attitude to me.

I express my gratitude to all the members of the *Suzaku* XIS team for their support of this study. All the observational data were obtained by the members of the *Suzaku* team.

I also thank to Dr. M. Bautz, S. Kissel, and B. LaMarr XIS team. for their hospitality during my visit to MIT in U.S.A..

I was financially supported by the Japan Society for the Promotion of Science.

Finally I express supreme thanks to my family, especially for my parents. They have provided me not only financial but also unstinted emotional support.